

2021

Design and Fabrication of Soft 3D Printed Actuators: Expanding Soft Robotics Applications

Ryan G. Drury

Follow this and additional works at: <https://ro.uow.edu.au/theses1>

University of Wollongong

Copyright Warning

You may print or download ONE copy of this document for the purpose of your own research or study. The University does not authorise you to copy, communicate or otherwise make available electronically to any other person any copyright material contained on this site.

You are reminded of the following: This work is copyright. Apart from any use permitted under the Copyright Act 1968, no part of this work may be reproduced by any process, nor may any other exclusive right be exercised, without the permission of the author. Copyright owners are entitled to take legal action against persons who infringe their copyright. A reproduction of material that is protected by copyright may be a copyright infringement. A court may impose penalties and award damages in relation to offences and infringements relating to copyright material.

Higher penalties may apply, and higher damages may be awarded, for offences and infringements involving the conversion of material into digital or electronic form.

Unless otherwise indicated, the views expressed in this thesis are those of the author and do not necessarily represent the views of the University of Wollongong.

Research Online is the open access institutional repository for the University of Wollongong. For further information contact the UOW Library: research-pubs@uow.edu.au



Design and Fabrication of Soft 3D Printed Actuators: Expanding Soft Robotics Applications

Ryan G. Drury

**Supervisors:
Gursel Alici
Vitor Sencadas**

**This thesis is presented as part of the requirements
for the conferral of the degree:**

Doctor of Philosophy

August 2021

University of Wollongong, Australia

Faculty of Engineering and Information Sciences

**School of Materials, Mechanical, Mechatronic,
and Biomedical Engineering**

ABSTRACT

Soft pneumatic actuators are ideal for soft robotic applications due to their innate compliance and high power-weight ratios. Presently, the majority of soft pneumatic actuators are used to create bending motions, with very few able to produce significant linear movements. Fewer can actively produce strains in multiple directions. The further development of these actuators is limited by their fabrication methods, specifically the lack of suitable stretchable materials for 3D printing.

In this thesis, a new highly elastic resin for digital light projection 3D printers, designated ElastAMBER, is developed and evaluated, which shows improvements over previously synthesised elastic resins. It is prepared from a di-functional polyether urethane acrylate oligomer and a blend of two different diluent monomers. ElastAMBER exhibits a viscosity of 1000 mPa.s at 40 °C, allowing easy printing at near room temperatures. The 3D-printed components present an elastomeric behaviour with a maximum extension ratio of 4.02 ± 0.06 , an ultimate tensile strength of (1.23 ± 0.09) MPa, low hysteresis, and negligible viscoelastic relaxation.

Using this elastomeric material, a new 3D printable soft pneumatic actuator is produced and evaluated. The presented pneumatic device, the linear soft multi-mode actuator (LSOMMA), is capable of both extension and contraction under differential pressures. It operates at low pressures, achieving full contraction and expansion at gauge pressures of -25 kPa and 75 kPa, respectively, corresponding to actuator strains of up to -50% and 37%. The LSOMMA is demonstrably scalable, provides a stable response over its lifetime of >10 000 cycles, and has a rise time of less than 250 ms.

ElastAMBER actuators show promise for creating intrinsically capacitive sensing devices, displaying a strong correlation between actuator displacement and capacitance. The developed 3D printable ElastAMBER can find potential functions as dual sensors and actuators for human-machine interface applications. The soft robotic applications of these multi-mode actuators are

demonstrated by developing a pipe-crawling robot capable of traversing horizontal, vertical, and bent sections of a pipe, and a ground locomotion robot capable of moving at 652 mm.min^{-1} and turning at $361^\circ.\text{min}^{-1}$. An untethered locomotion robot that can navigate multiple surface materials is assembled to demonstrate the potential of the developed technologies for lightweight autonomous robotic applications.

ACKNOWLEDGEMENTS

First of all, I'd like to deeply thank my academic supervisors, Senior Professor Gursel Alici and Dr Vitor Sencadas, for their support and direction the past few years. Their wealth of knowledge, experience, and intuition helped me greatly throughout my thesis work. I hope I did your efforts justice.

I'd also like to extend my gratitude to Dr Rahim Mutlu, my former co-supervisor, who unfortunately moved away from academic life at the University of Wollongong in my final year. You provided significant guidance in and out of the lab and were always free to discuss ideas and directions with me. The EIS Workshop staff were also a great help throughout this work. Especially Doug and Brian in the electrical workshop, you were both an immense help and I could not have completed this without your assistance on some projects.

This research has been conducted with the support of the Australian Government Research Training Program Scholarship.

On a more personal note, Alexa and Sina, you were amazing office mates, always happy to chat, get coffee, and communally procrastinate. I hope your theses finish smoother than mine did.

I have been supported immensely by my wonderful group of friends all these years. You all are the kindest, funniest, most supportive people there could ever be. Thanks for all the chats, drinks, hangs, and games. Once this is submitted, there will be time for many more.

I would not be here if not for my parents. Okay but seriously, I wouldn't be, Mum & Dad, thank you for caring for me all my life and helping shape me into the person I am today. I've always joked you're far too nice to me, because you are just lovely people through and through.

Equally lovely people who are far too nice to me are my partner's parents. Just a wealth of caring and knowledge from both of you, thank you for letting me into your lives and sharing it with me.

My dearest Shannon Freya, I appear to have run out of space... Oh well, you already know everything I have to say anyway, a million times over.

CERTIFICATION

I, Ryan Grant Drury, declare that this thesis, submitted in partial fulfillment of the requirements for the award of Doctor of Philosophy at the University of Wollongong, Australia, is wholly my work unless referenced or acknowledged otherwise. This document has not been submitted for qualifications at any other university or academic institution.

Ryan G. Drury

31 August 2021

TABLE OF CONTENTS

Abstract.....	i
Acknowledgements	iii
Certification.....	iv
Table Of Contents.....	v
List of Figures	vii
List of Tables	xi
1 Introduction	1
1.1 Aim & Objectives.....	3
1.2 Contributions	3
1.3 Thesis Outline	4
2 Literature Review.....	6
2.1 Current Actuation Technologies	6
2.1.1 Conventional Fluidic Actuators	10
2.1.2 Shape Memory Alloy Actuators.....	11
2.1.3 Electroactive Polymer Actuators.....	13
2.1.4 Piezoelectric Actuators	15
2.1.5 Biological-Synthetic Actuators	16
2.2 Soft Pneumatic Actuator Technologies	18
2.2.1 Pneumatic Artificial Muscles.....	20
2.2.2 Pneumatic Network Actuators.....	25
2.2.3 Various Novel Pneumatic Actuation Concepts	29
2.3 3D Printing	41
2.3.1 3D Printing Technologies.....	41
2.3.2 Photopolymer Resins.....	45
2.3.3 Base Components of Resins	47
2.3.4 Factors Affecting Curing and Material Properties	56
2.3.5 Recent Improvements in DLP Printable Materials.....	60
2.4 Summary.....	66
3 Materials and Methods	68
3.1 Resin Materials, Synthesis, and Evaluation.....	68
3.2 3D Printing of Resins	70

3.3	Cured Polymer Characterisation.....	73
3.4	Actuator Evaluation	75
4	Development of an Elastomeric Resin for Digital Light Processing Printing 77	
4.1	Introduction.....	77
4.2	Preliminary Resin Formulation Experiments.....	77
4.2.1	Printer Modifications	77
4.2.2	Resin Formulation and Initial Evaluation	78
4.2.3	Initial Mechanical Evaluation.....	83
4.3	Results and Discussion	87
4.3.1	Evaluation of the ElastAMBER Resin.....	87
4.3.2	Physical and Thermal Properties of 3D Printed ElastAMBER	89
4.3.3	Evaluation of the Cross-Linking Density of ElastAMBER.....	94
5	Linear Soft Multi-Modal Actuators	98
5.1	Introduction.....	98
5.2	Actuator Performance.....	99
5.3	Electromechanical Behaviour of ElastAMBER Actuators	109
5.4	Finite Element Analysis	110
5.5	Locomotion Robots.....	113
5.6	Discussion.....	120
6	Conclusions and Recommendations for Future Work.....	126
6.1	Conclusions	126
6.2	Recommendations for Future Research	127
	References.....	130
	Appendix A.....	142

LIST OF FIGURES

Figure 2.1 HyQ-series hydraulically actuated quadruped robots are emblematic the size and bulk of conventional pressure actuated robots (adapted from [35], © 2017 IEEE).....	11
Figure 2.2 Operation of IPMC actuators: (a) a labelled schematic of ion diffusion during actuation (adapted from [44], © 2011 IOP Publishing) and (b) time sequenced photos of an IPMC bending under 3 V (adapted from [2], © 2018 Wiley).....	13
Figure 2.3 Strain profile of an electronic EAP (adapted from [44], © 2011 IOP Publishing).....	14
Figure 2.4 Piezoelectric strain deformations: (a) longitudinal, (b) shear, and (c) bending (adapted from [48], © 2017 PI-Ceramic).	16
Figure 2.5 Size scale of biological soft robot units (adapted from [25], © 2015 Annual Reviews Inc.).	17
Figure 2.6 Pneumatic artificial muscles: (a) common forms (from left to right): McKibben braided, pleated, Paynter hyperboloid, Yarlott netted (adapted from [59, 60], © 2011 IEEE) and (b) the bulging activation of a pleated PAM (adapted from [52], © 2002 EJME).....	21
Figure 2.7 Relationship between force, pressure, and contraction ratio for a Festo DMSP PAM (adapted from [61], © 2016 Festo Corp.).....	22
Figure 2.8 Various biomimetic PAM-based robots, showing the significant amount of supporting structures required for the operation of PAMs (adapted from [59], © 2011 IEEE).	24
Figure 2.9 Various PAM-based orthotic devices (adapted from [59], © 2011 IEEE)	25
Figure 2.10 Structure and actuation of PneuNets, (a) a monolithic PneuNet geometry and (b) a segmented PneuNet geometry (adapted from [68], © 2014 Wiley).....	26
Figure 2.11 Bending actuator concepts: (a) a flexible micro-actuator, (b) a moulded balloon-jointed finger model, and (c) a glued asymmetric balloon actuator (adapted from [11], © 2009 Elsevier).	31
Figure 2.12 Individual Peano element (left) and rotary Peano actuator (right) (adapted from [86], © 2014 ASME).....	32
Figure 2.13 Vacuum-powered soft pneumatic twisting actuator (V-SPTA) (adapted from [90]).....	33
Figure 2.14 Operation of the HCRPAM (adapted from [13], © 2017 Liebert Pub.).....	35
Figure 2.15 Soft linear vacuum actuators: (a) shear-based (adapted from [92], © 2017 Wiley) and (b) buckling-based (adapted from [50], © 2016 Wiley).....	37

Figure 2.16 Extending soft pneumatic actuators: (a) balloon-like soft actuator (adapted from [96], © 2015 IEEE) and (b) inverse-PAM type (adapted from [56], © 2016 IEEE).....	38
Figure 2.17 Linear soft vacuum actuators (LSOVA): (a) cross-section of a one chamber LSOVA, (b) five chamber LSOVA unpressurised, (c) five chamber LSOVA under -96 kPa, (d) soft finger in open position, (e) soft finger in closed position, (f) soft finger grasping a screwdriver, and (g) LSOVA-based elbow joint (adapted from [79], © 2019 IEEE).	40
Figure 2.18 Common ink- and light-based 3D printing methods: (a) fused deposition modelling, (b) material jetting, (c) selective laser sintering, and (d) digital light projection stereolithography (adapted from [99], © 2016 Nature).....	42
Figure 2.19 General chemical structure of common acrylate (red) terminated oligomers.....	48
Figure 2.20 n monomers of a diisocyanate reacting with n monomers of a polyol to create a polyurethane of chain length n . Singular functional groups highlighted in red.	49
Figure 2.21 Generalised influence of monomer functionality on the conversion ratio and cure times of a urethane acrylate resin (adapted from [133], © 2001 Emerald Insight).....	49
Figure 2.22 Chemical structures of common diluent monomers.	50
Figure 2.23 Chemical structures of Type I photoinitiators TPO, BAPO, and CPK, Type II photoinitiator CQ.	52
Figure 2.24 Relative spectral absorbance values for several photoinitiators at a concentration of 0.25 mol% (adapted from [145] , © 2015 Elsevier).....	52
Figure 2.25 Pigment colour transmittance of a spectra of light (adapted from [128], © 2010 CRC Press).....	54
Figure 2.26 The effect of the concentration of the photoinitiator on the cure depth of a resin (adapted from [128], © 2010 CRC Press).....	57
Figure 2.27 Effects of temperature and dilution upon resin viscosity for (a) an aliphatic urethane diacrylate resin (adapted from [118], © 2017 Allnex Group), (b) a dimethacrylate oligomer-based resin with alumina suspensions (adapted from [124], © 1998 Elsevier), and (c) resins with different oligomeric molecular weights (adapted from [116] , © 2011 Wiley).	59
Figure 2.28 Mechanical properties of elastomer mixtures of Ebecryl 113 and Ebecryl 8413: (a) stress-strain curves and (b) mechanical properties box plots (adapted from [82], © 2017 Wiley).....	61

Figure 2.29 Direct ink writing material (a) stretched by hand, (b) mechanical properties at different printing angles, and (c) stress-strain behaviour at different printing angles (adapted from [161], © 2018 ACS).....	63
Figure 2.30 Stress-strain curves of HEA-based photopolymeric resins (adapted from [83], © 2017 ACS).....	65
Figure 3.1 (a) Schematic of the resin synthesis process, (b) schematic of the DLP 3D printing process, and (c) Titan 2 HR DLP printer (adapted from kudo3d.com).....	69
Figure 4.1 Titan printer modifications (a) heating system elements and build platform, and (b) transmission properties of the old and new projector filters.	78
Figure 4.2 Geometric test piece (a) model and (b) printed part at 0.25 wt% carbon black pigment.	83
Figure 4.3 Stress-strain curves for (a) EBECRYL 8411 and IBOA (2.7:1, TPO 4%, CB 1%), (b) BR-345 and IBOA (1:1, TPO 4%, CB 1%), (c) BR-345 and IBOA (1:1, TPO 1%, CB 0.5%), and (d) BR-345 and IBOA (1:1, TPO 2%, CB 0.5%).	85
Figure 4.4 (a) BR-345 and HEA (1:1, TPO 2%, CB 0.5%) stress-strain curves, (b) BR-345 and HEA (1:1, TPO 2%, CB 0.5%) hysteresis curves, and (c) BR-345 and IBOA (1:1, TPO 2%, CB 0.5%) hysteresis curves.....	86
Figure 4.5 ElastAMBER resin properties: (a) GPC comparison between BR-345 oligomer and ElastAMBER resin, (b) resin viscosity with respect to shear rate, and (c) resin viscosity with respect to temperature.	88
Figure 4.6 Scanning electron microscope images of (a) printed mechanical specimen cross-section and (b) elastomer surface.	90
Figure 4.7 ElastAMBER specimen (a) measurement, (b) stretched 250%, (c) twisted 2.5 times, and (d) bent 180°.	91
Figure 4.8 Mechanical responses (a) stress versus extension ratio, (b) hysteresis cycles, and (c) stress relaxation.	92
Figure 4.9 Thermal properties of ElastAMBER: (a) storage modulus (E') and the loss factor ($\tan\delta$) versus temperature for ElastAMBER and (b) elastomer mass loss versus temperature.	94
Figure 4.10 Swelling experiment: (a) dry polymer sample, (b) polymer sample completely swollen with THF, and (c) polymer swelling ratio with respect to time.	95
Figure 5.1 A one chamber 20 mm face diameter LSOMMA: (a) cross-sectional side view, (b) side view with dimensions labelled, and (c) photo.....	99
Figure 5.2 A 3C 14 mm LSOMMA: (a) unpressurised (b) with 75 kPa applied, and (c) with -25 kPa applied.....	100

Figure 5.3 Displacement responses to step inputs (a) 1C 20 mm step responses, (b) 1C 14 mm step responses, and (c) 3C 14 mm step responses.	102
Figure 5.4 Hysteresis curves of ramped pressure cycles in LSOMMAs (a) 1C 20 mm 75 kPa, (b) 3C 14 mm 75 kPa, (c) 1C 20 mm -25 kPa, and (d) 3C 14 mm -25 kPa.	104
Figure 5.5 Bode plots for a 1C 20 mm LSOMMA (a) at 75 kPa and (b) at -25 kPa.	105
Figure 5.6 Actuator creep and lifetime (a) 1C 20 mm held at 25 kPa showing pressure and displacement creep, (b) 1C 20 mm held at -25 kPa showing creep, (c) 1C 14 mm showing stroke lifetime at cycles of 75 kPa, and (d) 1C 20 mm showing stroke lifetime at cycles of -25 kPa.	106
Figure 5.7 1C 14 mm LSOMMA after failure: (a) imperfection in the wall and (b) failure at imperfection shown by squeezing the actuator.	107
Figure 5.8 Destructive test on a 1C 20 mm LSOMMA (a) pressure-displacement graph, (b) unpressurised LSOMMA, and (c) LSOMMA at 101 kPa.	108
Figure 5.9 Relationship between the change in capacitance and the air gauge pressure. (a) 1C 20 mm LSOMMA with capacitive probes connected, (b) positive pressure step inputs, (c) positive pressure step held for an hour, (d) positive pressure ramp input, and (e) vacuum pressure ramp input.	110
Figure 5.10 Finite element analysis results for a 3C 14 mm LSOMMA: (a) element strain at -25 kPa, (b) elemental stress at -25 kPa, (c) elemental strain at 75 kPa, and (d) elemental stress at 75 kPa.	112
Figure 5.11 Pipe crawling robot with snapshots of individual steps. In the diagrams, aqua blue indicates a negative pressure (-20 kPa) actuated chamber, yellow an unactuated chamber, and red a positive pressure (50 kPa) actuated chamber.	114
Figure 5.12 Pipe crawler moving vertically. Left: negative pressures (-20 kPa) only. Right: positive (50 kPa) and negative pressures. Upper: positions at 0 s. Lower: positions after 30 s.	115
Figure 5.13 Soft pneumatic tethered locomotion robot, alternating between -20 kPa and 50 kPa (a) forward motion steps and (b) turning motion steps.	117
Figure 5.14 Untethered ground locomotion robot electrical and pneumatic schematic.	118
Figure 5.15 Untethered locomotion robot after six crawling cycles (11 seconds) on (a) a rubber mat, (b) wooden desk, and (c) office carpet.	119
Figure A.1 Pipe crawler robot moving through a 90° bent pipe.	142
Figure A.2 Tethered locomotion robot crawling under -20 kPa: (a) forwards motion steps and (b) turning motion steps.	143

LIST OF TABLES

Table 2.1 Quantitative comparison of actuator technology properties (adapted from [2, 7, 32-34]).	9
Table 2.2 Qualitative comparison of actuator technologies advantages and disadvantages.	9
Table 2.3 Material properties of Thrasher <i>et al.</i> photopolymeric resins (adapted from [83], © 2017 ACS).	65
Table 4.1 Sourced chemical types from various manufacturers.	79
Table 4.2 Reported properties of various commercial resin compounds.	80
Table 4.3 Molecular weights of the resin components from GPC.	88
Table 4.4 Comparison between ElastAMBER and other elastomeric materials.	97
Table 5.1 Dimensions and mass of LSOMMA units.	99
Table 5.2 Performance parameters of the LSOMMAs under step inputs.	101
Table 5.3 Elastomer hyperelastic material model constants.	111
Table 5.4 Comparison of LSOMMA performance with FEA predictions.	112
Table 5.5 Comparison between the performance of LSOMMA and LSOVA.	122
Table 5.6 Comparison of untethered soft pneumatic crawling robots.	125

1 INTRODUCTION

Traditional robotic applications have utilised electric motors for decades, employing their high accuracies, speeds, and stiffnesses for repetitive automated processes. However, in the emerging field of human-robot interactions and collaborative work, these traits are detrimental to safe operations and contact with soft, delicate, or inconsistent objects. Similarly, the development of small lightweight robotics has somewhat stagnated due to the limited power-to-weight and power-to-volume ratios of motors. Other established actuation technologies have been examined by this thesis to find the most suitable alternative for furthering the development of soft robotic devices.

The actuators were assessed based on criteria such as mass, speed, force, volume, and intrinsic compliance, and the balance between these. Factors such as the type of motion generated (linear, rotational, etc.), generable strains, energy efficiency, and safety considerations were also taken into consideration. Pneumatic actuators, which have high power-to-weight ratios and intrinsic compliance due to the compressibility of air, were selected for the focus of this thesis.

Soft pneumatic actuators are typically constructed from hollow elastomeric parts, meaning they are lightweight, have excellent power-to-weight ratios, and are versatile in design. Depending on the geometry of the chambers and walls comprising the actuator, it can produce different motions such as elongation, contraction, bending, or twisting. Bending soft pneumatic actuators are the most common, as this type of motion can be produced through simple asymmetric geometries or anisotropic stiffnesses. Rarer are linear-acting soft pneumatic actuators, and actuators that can produce different motions when different modes of air pressure are applied.

Although there have been numerous studies into the development of novel soft pneumatic actuators, there are still many potential designs to investigate that are currently inaccessible due to current fabrication obstacles. Most soft pneumatic actuators are manufactured either by moulding

components separately then gluing them together, or by 3D printing monolithic structures. Moulding methods are limited to simple designs but can select from a broad range of materials. Conversely, 3D printing technologies have the potential to create components with complex geometries but have severely restricted materials options.

For further developments in the field of soft pneumatic actuators to occur, advances must also be made to the fabrication methods. As such, the purpose of this thesis was to synthesise a new elastomeric material 3D printing, then construct a new soft pneumatic actuator. Several material formulations were evaluated for their mechanical properties, such as viscosity, elongation at break, and hysteresis. The best performing elastomeric material was used in the development of new soft pneumatic actuators. This material, named ElastAMBER, was synthesised in the form of a resin capable of curing into complex elastic parts at near-room temperature using an off-the-shelf printer. The cured elastomer showed good elongation, low hysteresis, and a stable stress-relaxation response, equalling or surpassing most other 3D printable elastomeric materials.

Actuators were 3D printed using ElastAMBER which could produce linear motions and are unique in that their motion direction changes depending on the input pressure type, dubbed LSOMMA. Under positive gauge pressures, the actuators expand linearly, whereas negative gauge pressures produce lengthwise contractions, thereby producing bidirectional actuation *in the same design*. The stroke, speed, force, lifetime, stability, and scalability of the new soft pneumatic actuator were evaluated, showing significant improvements in response time, maximum strain, and lifetime in comparison to similar actuators. These actuators were used in robotic applications to assess their broader utility.

A pipe crawling robot was constructed from three independent LSOMMAs, which could crawl horizontally, vertically, and around corners. It outperformed other similar pneumatically operated soft robots in terms of speed compared to body length. Ground-based crawling robots were also assembled to how LSOMMAs can be used for unconstrained locomotion,

including the ability to turn. An untethered version of the ground locomotion robot was able to traverse multiple surface materials, including difficult ones like carpet. Importantly, the low operating pressures of LSOMMAs permit the use of smaller and lighter pumps and other control components, allowing possibilities for the creation of mobile devices. Both the tethered and untethered versions performed significantly better in many categories in comparison to many of the other soft robots of similar natures in the literature.

1.1 Aim & Objectives

Aim –

- To develop a new 3D printable elastomeric material and apply it to a new class of soft pneumatic actuators.

Objectives –

- Formulate, synthesise, and optimise a new highly elastic (strain > 200%, cycles to failure > 1 000) material for 3D printing.
- Characterise and evaluate the 3D printable elastomer.
- Design, manufacture, and evaluate a new type of soft pneumatic actuator capable of sophisticated linear motions.
- Develop robotic devices based on the new actuator concept and assess the performance relative to similar technologies.

1.2 Contributions

Considering the Aims and Objectives, the principal contributions of this thesis are:

- It proposes several modifications to commercial digital light projection 3D printers which improve the printability of resins.
- It summarises the factors which affect the formulation and curing of elastomeric 3D printable resins and outlines the optimal conditions. It evaluates many commercial oligomers and monomers for their effect on material properties.

- It proposes a new 3D printable elastomeric resin which shows a low viscosity at slightly elevated temperatures. The cured resin exhibits a highly elastomeric and responsive nature.
- It presents a new 3D printed linear soft pneumatic actuator that is capable of multi-modal operations, depending on the supplied pressure. This actuator can actively expand under positive gauge pressures and actively contract under negative gauge pressures.
- It presents how the elastomeric material can be used in a dual sensing-actuating device. The motions of the soft pneumatic actuator show a strong relationship between input pressure and capacitive response.
- It demonstrates that finite element analysis of the actuators can accurately predict the performance, and therefore can be used to optimise their performance.
- It presents several applications of the actuators in soft robotic locomotion prototypes. These locomotion robots show improvements over previously published designs of similar natures. One robot is untethered and can travel linearly and turn upon several different surface terrains.
- Paper published in the Journal of Applied Polymer Science: R. Drury, V. Sencadas, and G. Alici, "Development of an elastomeric resin for digital light processing printing," *Journal of Applied Polymer Science*, vol. n/a, p. 52123, 2022/01/10 2022.
- Paper published in Soft Matter: R. Drury, V. Sencadas, and G. Alici, "3D printed linear soft multi-mode actuators expanding robotic applications," *Soft Matter*, vol. 18, pp. 1911-1919, 2022.

1.3 Thesis Outline

The rest of this thesis is outlined as follows. Chapter 2 reviews the current literature and data related to the rationale, aims, and objectives of this thesis. It outlines the contemporary state of actuators and actuation technologies, with a focus on pneumatic technologies. It also investigates 3D

printing technologies, 3D printable material compositions, and resin synthesis. Chapter 3 presents the materials obtained and used throughout this thesis, the equipment used for development and measurement, and the data collection and analysis methodologies. Chapter 4 reports on the development of a novel elastomeric material for 3D printing. It initially outlines the iterative steps taken to produce the desired material, then evaluates many of its properties in depth. Chapter 5 presents the performance of a new soft linear pneumatic actuator. It evaluates the actuators' dynamic characteristics, verifies the results through simulations, demonstrates the significance of the actuator in robotic applications, and compares it to other similar technologies. Chapter 6 summarises the work undertaken in this thesis and proposes further applications and research questions.

2 LITERATURE REVIEW

2.1 Current Actuation Technologies

Actuators are devices which convert an energy input into a mechanical energy output in a predictable, repeatable, and reversible fashion [1]. The input energy is usually in the form of electrical, chemical, or pressure, while the mechanical energy output can be applied as forces affecting kinetic or potential changes. This mechanical transformation or deformation of the device can occur in one or more forms of motion such as linear, rotational (torsional), bending, or shear [2]. Actuators are usually composed of multiple parts, with relative motion created through the translation or rotation of one part relative to another fixed part. Some actuators, however, may comprise of a single monolithic component, which flexibly deforms when the external stimulus is applied.

In the past, the development of robotic actuator designs focused on the optimisation of simple and repetitive tasks to maximise work efficiency, most commonly for the automation of production lines. These machines are unsuitable for human interaction, as they typically lack sensors to detect human proximity, and any collision between the rigid structures of the robot and the soft flesh of a human could cause serious harm [3-7].

The definition of a “soft robot” is somewhat vague and nuanced. As described by Sachyani-Keneth et al. [8], soft robots are (1) made from flexible materials (are not hard-bodied) and (2) have motor-less actuation. They also state the actuation can be executed through pneumatic, electrostatic, thermal, and magnetic mechanisms. The scope of these parameters, for instance, excludes devices such as flexible hydraulic actuators and other niche devices from being classed as soft robotics. Another definition by Alici [7] makes the distinction between soft and hard robotics based on the rigidity or elasticity of the joints, links, and actuators, defined by a threshold of a 1 GPa elastic modulus. As these definitions allow for the possibility of soft actuators to be

produced from a broad range of actuator technologies, this thesis briefly investigates the potential of a number of actuation.

With the increased demand for human-robot interaction processes and the continued evolution of small-scale robotics, research has shifted to smaller and lighter devices which are safer to be in proximity to people [5, 9]. A requirement of this new wave of 'soft robotics' is intrinsic compliance, the ability of a device to deform and adapt to disturbances or interference by objects in its path without causing damage [3, 7, 10-13]. Another benefit of soft robotics over their hard counterparts is the reduced number of parts needed to complete a particular task, with a single actuator potentially having many degrees of freedom, being able to achieve a greater range of motion and more flexible trajectory options [7, 14]. However, in exchange for the higher degrees of freedom and compliance of soft actuators, the maximum force output is comparatively lower, due to energy being absorbed through the deformation of the soft parts and the lower material strengths [15, 16]. By being made from lightweight flexible structures, there are broader possibilities for creating small tethered or autonomous robotics [11, 12]. Small untethered robots have the potential for exceptional adaptation to a range of tasks and to be deployable in constrained environments [8, 14].

Many researchers are being inspired by the unique motions of limb systems found in nature and replicating them through robotics, a field of study known as biomimetics [17]. Evolution has culminated in a diverse range of animal life, with many unique and robust biological configurations. The study of animal locomotion is particularly relevant to the ongoing research into soft robotic actuators, as it is inspiring concepts based on joints and motions unavailable to humans [18, 19]. The cyclic movement of snakes and worms [20-23], the gait of caterpillars and inchworms [19, 22-25], the hydraulic-like leg actuation of spiders [26, 27], and the soft fluidic action of octopus tentacles [22, 28, 29] are just some of the many diverse and interesting inspirations for the development of new actuation concepts.

Sensors are required to properly regulate the operation of the actuators, providing data on the real-world position, force, and/or pressure, rather than relying upon ideal or predicted responses. Precise and dynamic control can be achieved through the integration of multiple high quality sensors [30]. Sensors have been created to detect most types of changes in physical and electrical phenomena [9, 30]. For recent developments of soft sensors, the author recommends Hughes *et al.* [9]. Intrinsically sensing soft actuators, devices which act as both a sensor and actuator, have been scarcely addressed in literature, largely due to the viscoelastic nature of soft materials that create modelling challenges, but also the strict requirements [12].

One of the main restrictions on manufacturing small-scale robotics is the lack of efficient actuation technologies with high power densities at small scales [12, 30]. The smallest actuators in the world, biological muscles, are built from repeating units starting from the microscale that work together in both series and parallel to provide bulk actuation [2, 25, 31]. Humanity currently lacks the ability to assemble actuator units as small, detailed, and sensitive as biological muscle. A general comparison of the basic properties of actuator classes is shown in Table 2.1, which has been compiled from several sources of data, while Table 2.2 provides a qualitative comparison of the actuators. By comparing the ranges presented in the older sources, for instance Huber *et al.* from 1997 [32], to the more recent articles, such as Mirvakili and Hunter from 2018 [2], tremendous improvement can be observed for some technologies, while others appear to have stagnated. For instance, the power density of DC motors is largely unchanged, whereas newer pneumatic technologies have seen upwards of a fourfold increase in power density. This may be attributed to the advancements in lighter materials for soft pneumatic robotics, as the soft polymeric walls significantly decrease the per unit mass of pneumatic devices compared to the traditional metallic housings.

Table 2.1 Quantitative comparison of actuator technology properties (adapted from [2, 7, 32-34]).

Actuator Type	σ_{max} (MPa)	ε_{max} (%)	E (MPa)	ρ (W.kg ⁻¹)	Efficiency	f_{max} (Hz)
Pneumatic	0.5 – 3.4	10 – 100	50 – 90	4 000	0.4 – 0.9	50 – 300
Muscle	0.1 – 0.4	30 – 40	5 – 20	50 – 284	0.2 – 0.25	20
DC Motor	0.1	N/A	depends on gearing	100	depends on gearing	N/A
Hydraulic	20 – 70	10 – 100	2 000 – 3 000	1 600 – 2 000	0.9 – 0.98	50 – 300
SMA	100 – 700	10	30 000 – 90 000	6 400 – 6 600	0.01 – 0.02	0.02 – 3
IPMC EAP	4 – 10	2 – 80	200 – 300	244	<0.03	0.1 – 100
DEA EAP	5 – 29	80	-	-	0.6 – 0.9	1 000
Piezoelectric	110	0.2	-	-	0.9	10 × 10 ⁶

σ_{max} : maximum stress, ε_{max} : maximum strain, E : Young's modulus, ρ : specific power, f_{max} : maximum actuation frequency

Table 2.2 Qualitative comparison of actuator technologies advantages and disadvantages

Actuator Type	Advantages	Disadvantages
Pneumatic	High specific power, high strain	Non-linear response, low stiffness
DC Motor	Linear response, simple control scheme, high speed	Low force generation, high stiffness in applications requiring compliance
Hydraulic	Very high stiffness, high work	Heavy system, density of

	density, high efficiency	working fluid
SMA	Very high stiffness, very high work density	Low strain, low speed, very low efficiency
IPMC EAP	Suitable for aqueous environments	Very low efficiency, very low speed
DEA EAP	High efficiency, high speed	High electric fields
Piezoelectric	Very high efficiency, very high speed	Very low strain

The selection of an actuator for a task involves the consideration of the most desired performance characteristics and weighing these against the inherent constraints of that technology. Every existing type of actuator technology involves a compromise between the varying performance properties, where an actuator may exhibit good performance in some areas but is found lacking in others [34].

2.1.1 Conventional Fluidic Actuators

Motion has been produced through the application of pressurised fluids for centuries, appearing first as steam-powered pistons and engines. The piston, a technology still in common use today, is a cylindrical vessel bisected by a sliding plate and rod, which are moved by the differential pressure on either side of the plate. The working fluid can be either a liquid or a gas, referred to as hydraulic and pneumatic systems respectively. Hydraulic and pneumatic systems utilise pumps and compressors, respectively, to pressurise and drive the working fluids around networks of reservoirs, pipes, tubes, valves, sensors, and/or actuators [9]. Although many principles are shared, there is a significant difference in performance, advantages, and drawbacks between pneumatics and hydraulics [9]. This subsection will focus mostly on hydraulic technologies, with pneumatic technologies analysed in greater depth in Section 2.2.

Robotics based on conventional hydraulic pistons require appropriately strong supporting structures, resulting in extremely heavy autonomous

locomotion robots which may weigh between 24 kg and 160 kg (Figure 2.1) [35]. Careful design can minimise these drawbacks, providing small scale fluidic actuators an excellent potential to deliver a combination of high actuation force and elongation [36]. However, by using incompressible liquids over compressible gases, conventional hydraulic technologies are not intrinsically compliant and therefore are not classed as soft actuators [14, 37]. If constructed using flexible walls and chambers, they can be grouped with other soft fluidic actuators [11, 37], which are reviewed in Section 2.2.

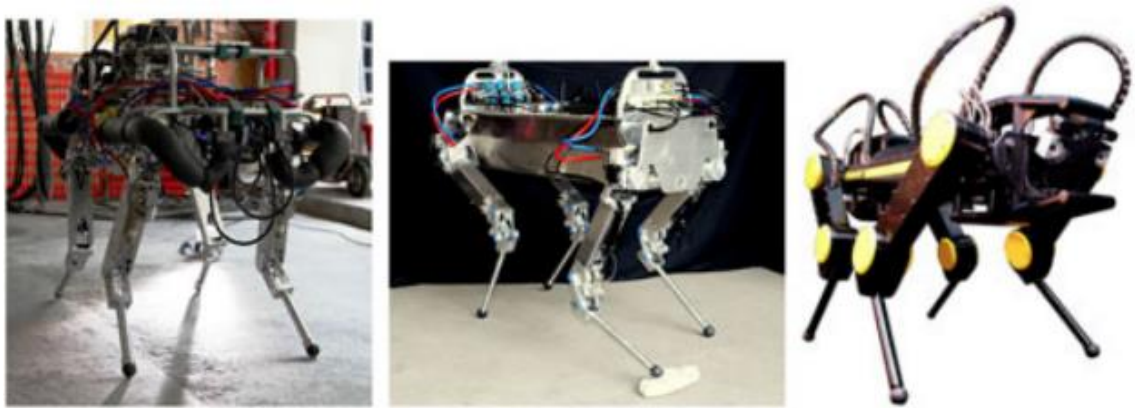


Figure 2.1 HyQ-series hydraulically actuated quadruped robots are emblematic the size and bulk of conventional pressure actuated robots (adapted from [35], © 2017 IEEE).

2.1.2 Shape Memory Alloy Actuators

Shape memory alloys (SMAs) are a class of metallic alloys which reform to their undeformed shape and size when heated. Cooling the alloys results in them returning to their original deformed shape [2]. This cyclic phenomenon is a material phase transformation process known as the shape memory effect [33]. SMAs are most commonly a nickel-titanium (NiTi) alloy due to its good overall performance, but other material combinations have been developed for specific requirements or applications [38]. SMAs operate in two different material phases corresponding to different temperature ranges: a martensite structure at low temperatures, and an austenite structure at higher

temperatures. For a more comprehensive description of how the shape memory effect works, the author recommends reading Mohd-Jani *et al.* [33].

Actuators capitalising on the shape memory effect show excellent promise in many areas due to their unique activation and performance characteristics. In general, NiTi SMA actuators exhibit very high work densities up to 25 times greater than that of electric motors, and high force-mass ratios [5, 24, 33, 38, 39]. These alloy actuators can operate under loads 100 times greater than their own body weight in some configurations, and display high wear resistance [33].

SMA actuators face unique challenges with their design, requiring large electrical currents to achieve rapid heating rates and significant operational temperatures [2, 39, 40]. SMA actuators can only achieve a very low operational efficiency due to waste heat and frequent heating/cooling cycles [2, 30]. The maximum theoretical energy efficiency of SMAs when analysed as a Carnot cycle heat machine is 10%, but in practice the efficiency is found to be near 1% for tensile configurations and much lower for bending and torsional actuators [22, 33, 41]. These actuators are typically limited to elastic strains of 10%, but owing to safety factors and the prevention of permanent plastic deformation, most applications are designed to operate at lower strain magnitudes, typically near 4% for NiTi alloys [2, 6, 33, 40-43].

The high force-to-mass and force-to-volume ratios of shape memory alloy actuators technologies shows there is considerable potential for the construction of lightweight and powerful devices. However, these actuators face significant challenges to their integration into further robotic applications, most notably the slow activation times, tiny strain outputs, and low thermodynamic efficiencies [33]. Additionally, shape memory alloy actuators are not intrinsically compliant, requiring the specific inclusion of springs or soft materials [40]. Furthermore, their electrical and thermal nature limits their safe use in biomedical applications, especially near electromagnetic sensitive equipment, or inside a patient where a fault could cause serious tissue damage [11].

2.1.3 Electroactive Polymer Actuators

Electroactive polymer (EAP) actuators share some functions to those of biological muscle, particularly compliance and reversibility [9, 44]. As a result of these properties, EAP actuators have attracted considerable attention in the hopes of the successful biomimetic emulation of natural movements and animal locomotion [9, 14, 45]. These particular types of polymers exhibit shape strains in response to the application of electric fields. There are two general categories of EAP actuators: ionic and electronic [19].

Of the ionic EAP actuators, the most common type is that of the ionic polymer-metal composite (IPMC), which is a conductive membrane filled with an electrolytic fluid [2]. When subjected to an electrostatic force, the mobile ions and/or charged molecules migrate within the membrane. The concentration of these charge-bearing particles along one side of the long slender actuators produces a bending motion, as can be seen in Figure 2.2 [44]. However, this process is extremely slow and can take minutes to complete in one direction [2].

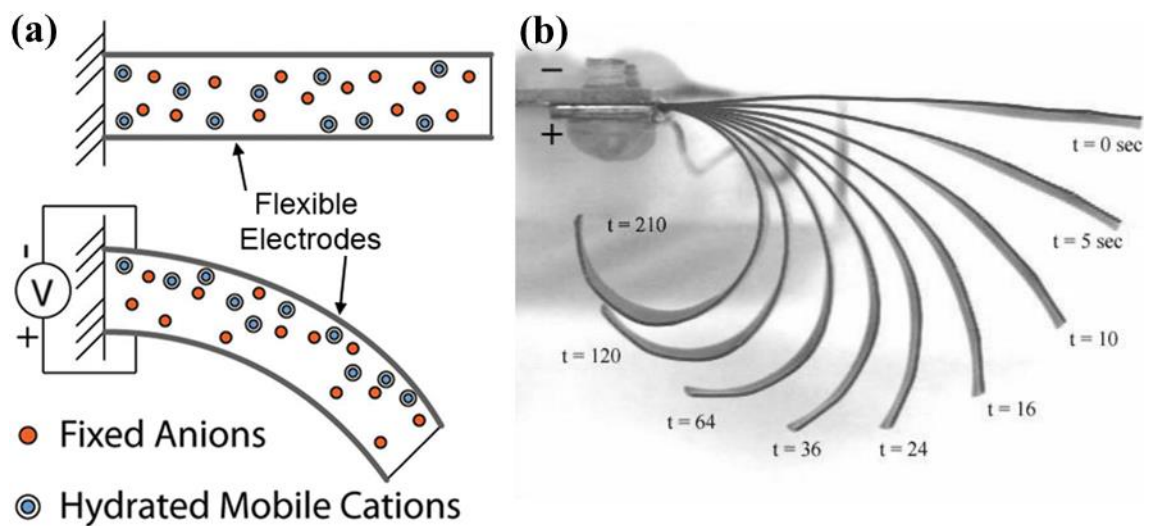


Figure 2.2 Operation of IPMC actuators: (a) a labelled schematic of ion diffusion during actuation (adapted from [44], © 2011 IOP Publishing) and (b) time sequenced photos of an IPMC bending under 3 V (adapted from [2], © 2018 Wiley).

Of the electronically activated electroactive polymers, the dielectric elastomer actuator (DEA) is regarded as the most promising, owing to its simplicity and well-rounded performance characteristics [44, 45]. Similar to the IMPC, the DEA is constructed by sandwiching a medium between two flexible electrodes, but the medium in this case is a film of low stiffness and high strain elastomer (Figure 2.3) [5, 45]. Upon the application of an electrostatic force, the electrodes attract towards each other, compressing the elastomer and resulting in an expansion in the lateral directions, as per the Poisson effect [2]. The magnitude of the applied voltage is dependent on the choice of polymeric material selected, but it generally exceeds $100 \text{ V} \cdot \mu\text{m}^{-1}$, close to the breakdown level of many conductive materials and even the dielectric layers [2, 44, 45].

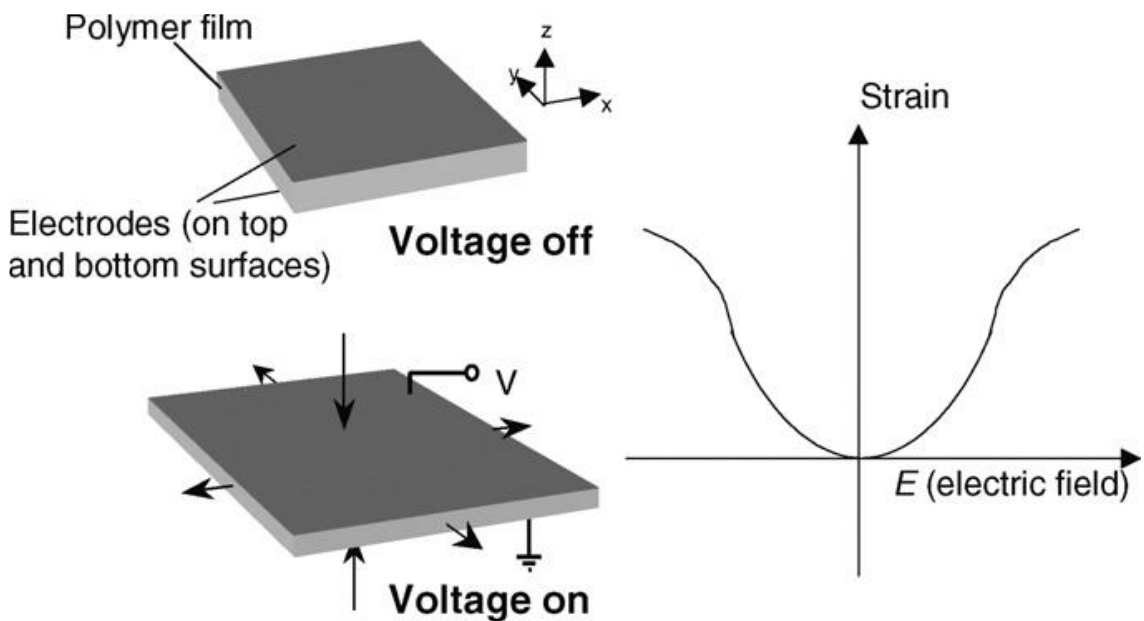


Figure 2.3 Strain profile of an electronic EAP (adapted from [44], © 2011 IOP Publishing).

There are two major advantages of electronic EAPs over ionic EAPs, firstly since the actuation of EAPs do not require the migration of ions, the response times are significantly faster, in the order of milliseconds, and secondly that these actuators may be used in air without serious constraints [39, 45]. The inclusion of elastic elements and compliant electrodes allow for DEAs

to produce strains up to 200% and the potential for high mechanical energy densities [5, 44, 45]. Their high bandwidth, up to 1 000 cycles per second, makes DEAs well suitable for use in devices such as switches, flapping robots, and loudspeakers [2]. Being constructed from elastomers and flexible films, DEAs exhibit excellent power densities and high efficiencies [2, 46]. However dielectric elastomer actuators require significant electrical field strengths to operate, requiring hundreds or thousands of Volts for actuation [2]. Heavy high voltage transformer units and rectifier circuits are often needed to power these DEAs, and there are serious health and safety issues regarding insulation, component breakdown, and electric shock [2, 38, 46, 47].

2.1.4 Piezoelectric Actuators

Piezoelectric actuators are like electroactive polymer actuators in that they directly convert electrical energy to mechanical energy and vice versa but are formed from stiff crystalline or ceramic materials instead. Piezoelectric actuators are able to create or detect highly accurate microscale strains, making them suitable for applications such as operating valves, creating fine motion in scanning microscopes, and extremely precise sensors [48, 49]. They can produce or detect many types of deformation, such as elongation, contraction, shear, and bending (see Figure 2.4). Piezoelectric operation is considered frictionless and subsequently allows for extremely high bandwidths, up to 10 MHz, making them ideal for ultrasound transducers and MEMS switches [2]. However, they can only produce tiny strains ($\sim 0.2\%$) and require a significant voltage (up to 1 kV) to do so, making them ultimately unsuitable for use in soft robotic locomotion devices [2, 34, 39].

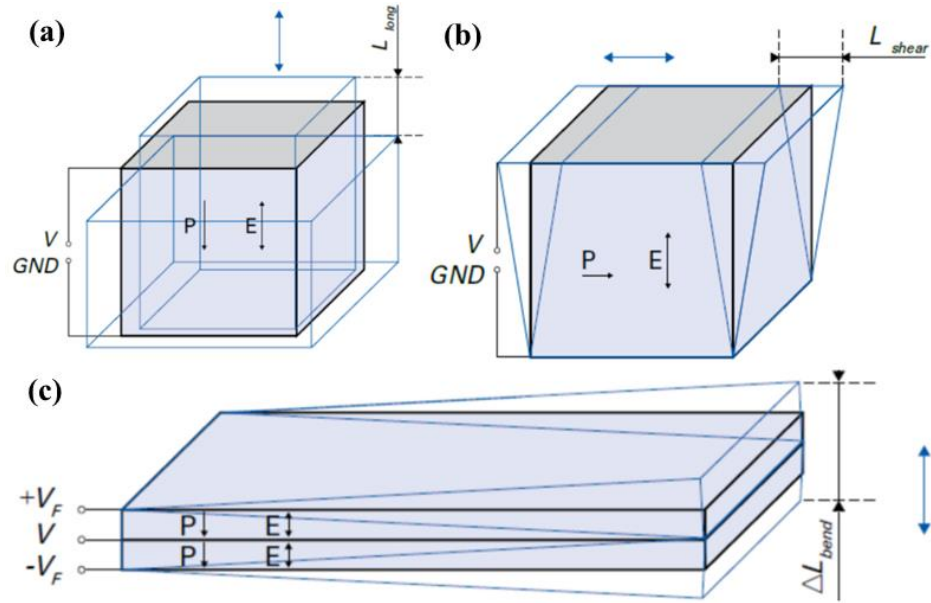


Figure 2.4 Piezoelectric strain deformations: (a) longitudinal, (b) shear, and (c) bending (adapted from [48], © 2017 PI-Ceramic).

Similar to piezoelectric actuators are electrostrictive actuators, which differ by the relationship between strain and electric field and by the materials used. In piezoelectric materials the relationship between applied electric field and contraction strain is linear, whereas electrostrictive materials show a parabolic relationship [2]. Poly(vinylidene fluoride-co-trifluoroethylene) (P(VDF-TrFE)) copolymer-based electrostrictive actuators can produce high thickness strains, up to 10%, when excited under extreme electric field strengths of 9 MV.m^{-1} [2].

2.1.5 Biological-Synthetic Actuators

Considering there is a large research focus on biomimetics and the imitation of natural movements in soft robots, one would surely enquire about the possibility of adapting biological muscle into soft robots as actuators. Biological muscle has numerous advantages, such as high force-weight ratio and incredible scalability, and some attempts have been made to develop hybrid systems incorporating both biological and synthetic components (see Figure 2.5) [2, 25, 31]. The integration of nanoscale and microscale biological systems with mechanical components could allow for the synthesis of high

strength and low elastic moduli living tissues with the backing of stiffer and reliable metals or polymers, resulting in a combination unobtainable from synthetic actuators alone [25]. Unfortunately, the synthesis of artificial biological muscle as usable actuators has yet to be achieved under current engineering techniques. In a recent review paper, eighteen biological-synthetic soft robots had their components and performance analysed (see [25] for full details).

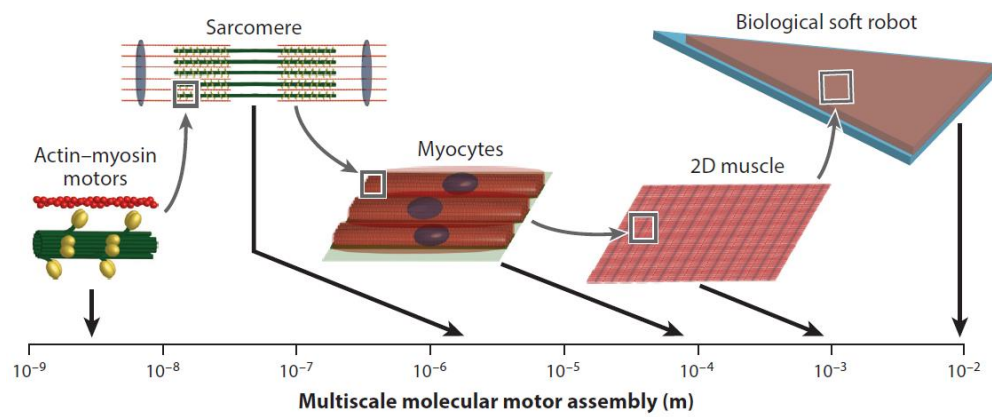


Figure 2.5 Size scale of biological soft robot units (adapted from [25], © 2015 Annual Reviews Inc.).

Unfortunately, there are serious challenges facing the further development of these hybrid biological-synthetic actuators. Firstly, these muscle tissues are harvested and removed from the rest of the body's systems, meaning there is no ongoing replacement or rebuilding of tissues by the body through cellular homeostasis [25]. Due to the lack of artificial growing methods, the primary source of the biological materials is the harvesting of tissue from small unborn animals, thus the actuators are heavily restricted in size. Additionally, all the grippers reported by [25] suffered from poor actuation performances relative to their size when compared to other technologies. To improve the actuation technology, biological-synthetic soft robots will need to produce larger displacements and forces.

2.2 Soft Pneumatic Actuator Technologies

Pneumatic actuators are devices that utilise differential air pressures to produce motion. The pressure driven nature of pneumatics provides a wide range of possible categories and mechanisms, as relative pressure differences can be achieved in two ways. Positive differential pressures, or positive gauge pressures, are the most used, as gas is easily compressible and high pressures can be created. When a positive gauge pressure is applied to an internal chamber, outwards pushing forces and/or expansions are applied to the surfaces. The use of negative gauge pressure, known as vacuum pressure, by contrast, stimulates the walls of an actuator to pull and/or contract inwards. Vacuum pressures are more limited in use, due to having a maximum differential of only 100 kPa in standard atmospheric conditions, and require a hyperbaric environment if this constraint is to be overcome [50, 51].

In correspondence with the ideal gas law, the compressibility of air gives pneumatic devices a level of intrinsic compliance. Any impulse or shock to a pneumatic system is partially absorbed by a change in either the internal pressure or volume. This means that upon any interaction or collision between the pneumatic actuator and any object, human, or environment, the actuator absorbs some of the energy, giving a softer and safer contact [8, 14, 30, 52, 53]. Vacuum pressure operations have an additional level of safety in that they cannot be catastrophically over-pressurised by accident, preventing the risk of explosions [51].

With the rise of new manufacturing methods for flexible and elastomeric materials, pneumatic actuators have begun taking the form of soft inflatable structures as the predominant form of research and development. Soft pneumatic actuators produce motion through structural material deformations. These actuators are extremely lightweight and versatile, with the flexible polymeric structures able to be constructed in a spectrum of unique geometries to generate complex motions such as bending, twisting, expanding, and/or contracting [10, 54]. The elastomeric materials store energy as they undergo deformation, which is used to passively reverse the applied strain when the

pressure is removed [12]. Most novel soft pneumatic actuators do not produce relative sliding motions between parts, thus there is little need for lubricants, no wear or loose particles created, and less chance of leakages [11].

Pneumatic actuators show similar performance characteristics to those of biological muscle, making them an excellent candidate for use as artificial muscles or in similar applications [32, 39, 50, 55]. Soft pneumatic actuators, when compared to human muscle, are capable of generating ten times the power per volume, fourteen times the power per mass, exhibit similar ranges of stress and bandwidth, and produce significantly higher strains [7, 33]. These properties represent a broad range of soft pneumatic technologies and varies depending on the individual actuator type and configuration. Pneumatic actuators have distinct benefits over hydraulic actuators of similar design due to differences in the physical properties of their working fluids. Atmospheric air, the prevailing gas used in pneumatics, is freely available and can be drawn from and released back into the environment without harm. This eliminates the need for the fluid reservoir required for hydraulic technologies [12, 37]. The density and viscosity of air are both negligible in comparison to all liquids, allowing lighter systems overall and less energy spent for operation [37].

There are a number of drawbacks to pneumatic systems to go along with the many advantages. Firstly, the compressibility of gas which provides the intrinsic compliance also creates hysteresis within the system, adding a level of difficulty to the control methods [11, 30]. The nonlinear relationships between pressure, elongation, and force may require the inclusion of additional sensors and a more sophisticated control routine where high precision is required [8]. In order to direct and regulate the flow of air through the system, a number of tubes and valves need to be present, adding slightly to the overall mass [6, 11, 16]. Pneumatic systems must be provided with a high pressure gas from either an electric motor-compressor or a pressurised canister [56]. The electric compressor component requires additional power to operate, is noisy, and actuator response times may be considerably slower if it needs to build up a head of pressure, but pressure can be reliably generated for as long as the

power supply lasts [38]. By comparison, a pressurised canister requires no power source, is noiseless, and its high pressure is available instantaneously via a regulator, but the volume and maximum pressure of air available are both finite and diminish with usage [5]. The last consideration is that pneumatic components must be sufficiently airtight, which can be a complex problem to address when designing devices with moving parts. A comprehensive review of pneumatic pressure generation for mobile devices and comparison of key characteristics has been conducted by Wehner *et al.* [57] and is recommended further reading on this subject.

The following subsections will discuss and comment upon the variety of soft pneumatic actuator designs in modern literature. The first is that of the pneumatic artificial muscle, a contractile rubber bladder which has seen many developments over several decades but is still frequently having advancements published. The second is a more modern pneumatic actuator, the pneumatic network actuator, which can be fabricated by moulding or 3D printing. There have been dozens of papers published regarding this type of actuator in recent years. The final section provides insight into the many varieties of unique soft pneumatic actuators in modern literature. These have been grouped by the primary type of motion generated by the actuators to allow some direct comparisons to be drawn.

2.2.1 Pneumatic Artificial Muscles

Conceptualised in the 1950s by an inventor called McKibben for use in orthotic rehabilitation devices, these actuators have frequently been implemented in robotic devices since the 2000s [52, 58, 59]. Though initially called McKibben actuators, these devices are known by various names such as pneumatic artificial muscles (PAMs), fluidic actuators, and pneumatic muscles actuators. They were the first type of soft pneumatic actuators to be widely implemented industrially, being applied to many prototypes and robotic devices. Although PAMs are more suitable for stationary machines performing general robotic applications, some headway has been made in adapting these

artificial muscles for autonomous robotics and human-machine interfaces [24, 38, 59]. There numerous ways the PAM can be constructed (see Figure 2.6).

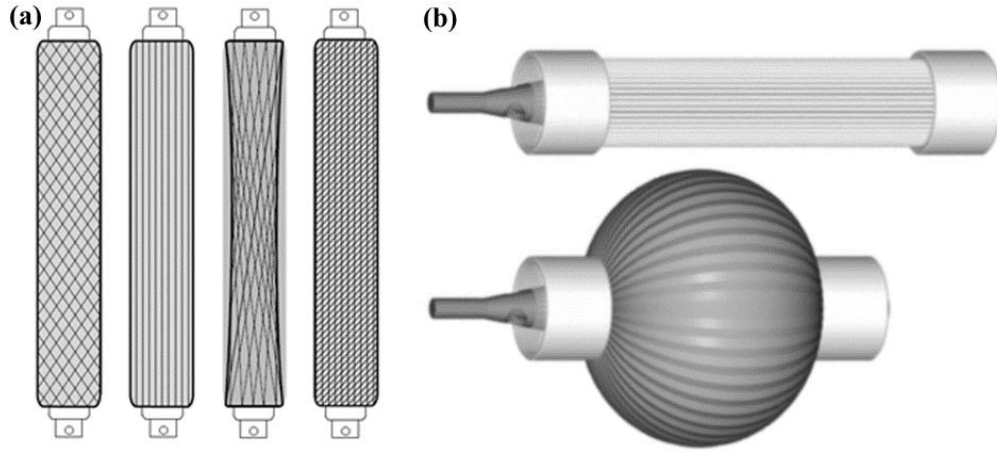


Figure 2.6 Pneumatic artificial muscles: (a) common forms (from left to right): McKibben braided, pleated, Paynter hyperboloid, Yarlott netted (adapted from [59, 60], © 2011 IEEE) and (b) the bulging activation of a pleated PAM (adapted from [52], © 2002 EJME).

Pneumatic artificial muscles show a number of advantages over traditional electric drives and other non-pneumatic soft actuators. They are able to transfer about the same amount of energy as pneumatic cylinders, due to similar operating pressures and volumes [52]. PAMs have a contraction ratio comparable to human muscles and can have power-to-weight ratios up to ten times more powerful than electric motors [24, 52, 60]. However, these higher ratios occur when maximum pressure is applied, typically between 500 kPa to 800 kPa [52, 61]. Pneumatic artificial muscles are easy and cheap to maintain, are relatively cheap to produce, and have a long service life up to one million cycles [4, 61].

PAMs can achieve contraction ratios similar to those of biological muscle, typically up to 25%, but this is small compared to that achievable by many other pneumatic technologies [61]. Some researchers have achieved up to 35% contraction, but those actuators were metres in length [60, 62]. PAMs do not scale well, with power-to-weight ratios and maximum operating pressures

both decreasing with smaller unit sizes [52, 61]. While the power-to-weight ratios of pneumatic actuator muscles may be reasonably high, their power-to-volume ratios are considerably lower due to their large dimensions and bulging during actuation [59]. A consequence of this bulging is the inability to closely group multiple PAM units in parallel, as two activated PAMs in contact would cause interference. Furthermore, this contact creates additional friction between the rubber and mesh surfaces, increasing losses and reducing the actuator lifetime [62].

The relationships between pressure, stroke, force, and velocity are highly nonlinear in pneumatic artificial muscles (Figure 2.7). This has resulted in difficulties in achieving accurate modelling and control of PAM-based systems [4, 52, 58, 61, 62]. This is due to a number of interconnecting factors, such as the compressibility of the gas, hysteresis effects of both the rubber sleeve and the mesh, and temperature influences [3, 58, 62]. For a full representation of the dynamics of the artificial muscle, the systems need to be modelled phenomenologically to obtain nonlinear differential equations, suitable for both conventional dynamic analysis and computer simulations, although this approach is computationally complex and time consuming [3, 58].

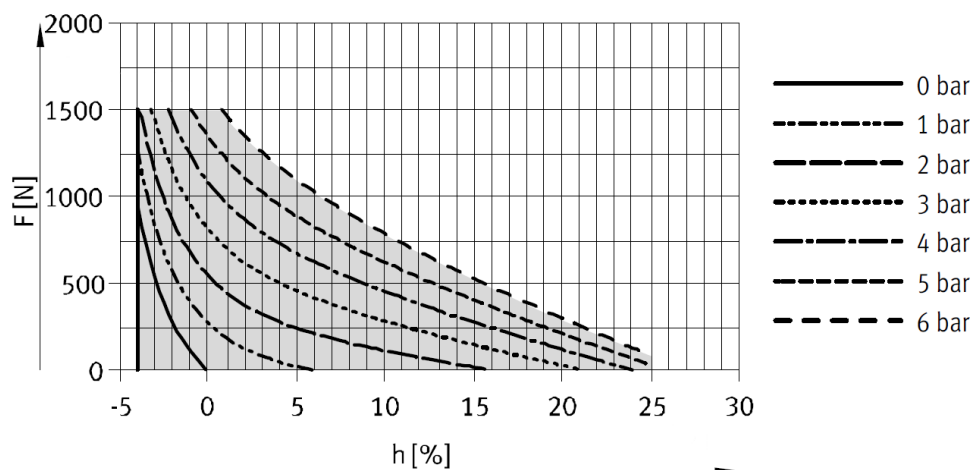


Figure 2.7 Relationship between force, pressure, and contraction ratio for a Festo DMSP PAM (adapted from [61], © 2016 Festo Corp.).

It is possible to modify McKibben muscles to produce bending, extending, or twisting movements, but performance is diminished severely [52, 56, 63, 64]. Pneumatic artificial muscles can only provide force in one direction, thus many applications require antagonistic pairs to effectively provide linear or rotational motion [4, 52]. Further issues with PAM application is that they cannot be directly attached to joints without a heavy, rigid support structure, and have a short life due to constant frictional wear from mesh sliding and fatigue from repeated expansion and contraction of the rubber tube [46, 52, 62, 65].

Pneumatic artificial muscle actuators have been introduced in many areas such as industrial robots, biomimetic robots, and medical and orthotic devices. Pneumatic actuator muscles have been used to replace pneumatic cylinders in automated gripper tools, robot arms, and in pick and place operations [3, 46, 59, 61]. PAM driven robotic designs have recreated many bodily operations; legs which can walk or leap, arms capable of waving and grasping, and one which could replicate the motion of the eye. Many bio-inspired robots have been created such as quadrupeds, arthropods, and manta rays [59]. Despite using soft actuators for motion, these robots are all rather heavy and feature many metallic structures (see Figure 2.8).

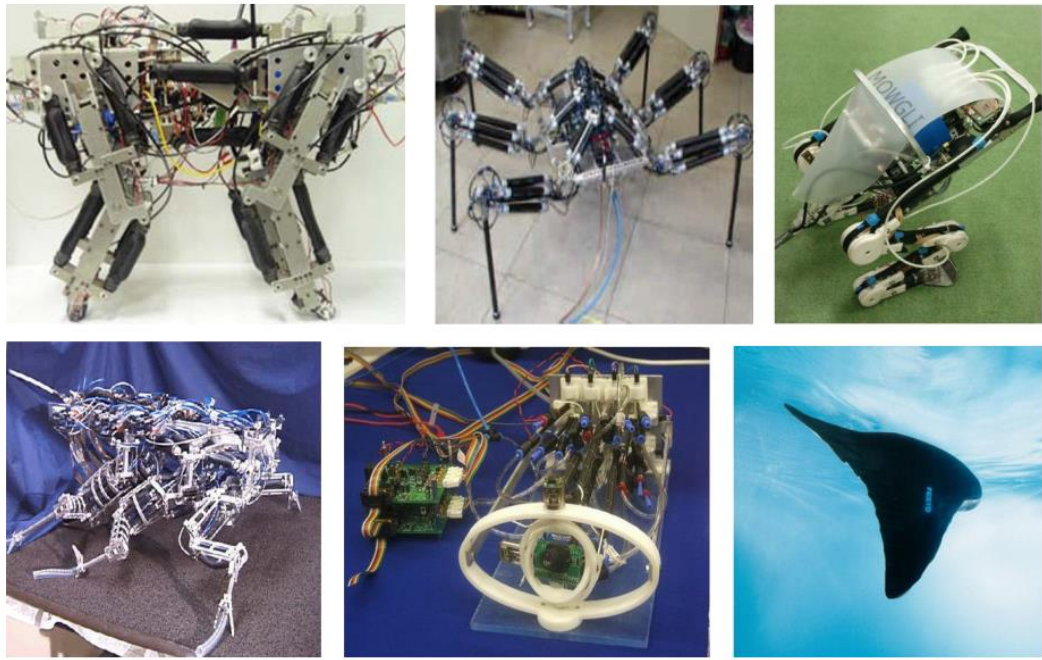


Figure 2.8 Various biomimetic PAM-based robots, showing the significant amount of supporting structures required for the operation of PAMs (adapted from [59], © 2011 IEEE).

In terms of human-machine interfacing robots, pneumatic artificial muscle actuators have proven useful in orthotic devices for limbs and larger joints (see Figure 2.9). As these rehabilitation devices need not be lightweight and mobile, they can afford to be constructed using large exoskeletons and supporting structures necessary for the operation of PAMs. These are not intended to be worn constantly or used mobile, but rather used as an exercise tool to assist and strengthen the body's muscles. These devices can be worn as elbow, shoulder, hand, knee, or hip exoskeletons for gait training and muscle rebuilding in people suffering from debilitating conditions [52, 59].

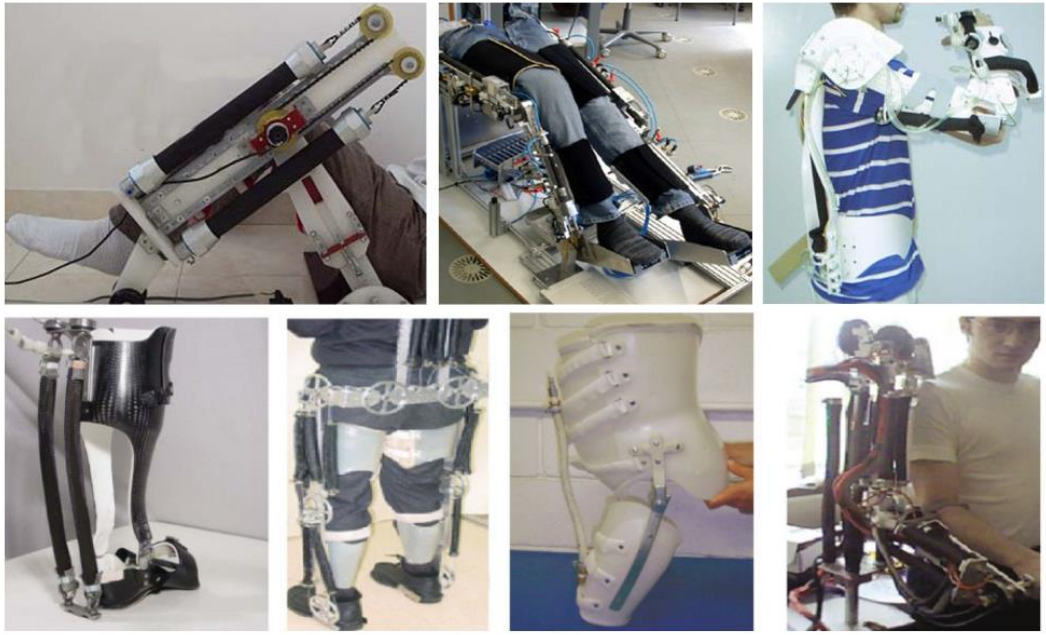


Figure 2.9 Various PAM-based orthotic devices (adapted from [59], © 2011 IEEE)

This technology, though popular for decades, has begun to reach the end of its usefulness and is not viable for future technologies requiring more sophisticated and advantageous geometries [12].

2.2.2 Pneumatic Network Actuators

Accounting for the shortcomings of pneumatic artificial muscles and to take further advantage of the unique features of flexible pneumatics, research goals began to shift towards smaller and softer actuator concepts [54]. With intrinsic compliance remaining a priority, all manners of flexible pneumatic chamber designs have been investigated. Bending actuators have been comprehensively studied due to the appeal of biomimicry, with inspiration for actuators drawn from the locomotion of snakes, worms, and octopuses, and the prehensile movements elephant trunks, animal tails, and more [14, 66]. Arguably, the concept which has received the most research attention has been the elastomeric multi-chambered pneumatic network actuators, which will be referred to as PneuNets henceforth. There are many variations of the PneuNet concept, and these may be called different names by different groups, such as

PneuFlex actuators or fluid elastomeric actuators (FEAs), but they have the same working principle and will be examined together in this section [9, 54, 67, 68].

The basic structure of a pneumatic network actuator is rather simple: a linear array of flexible chambers are connected by a strip along one edge, and can be fabricated by either multiple part-moulding or 3D printing technologies (see Figure 2.10) [54, 63, 69]. Moulded PneuNets are assembled from two layers of material, the lower layer being a strip made using a flexible but inextensible material [70]. The upper layer is comprised of multiple elastic chambers connected in series which share a pneumatic channel and is grafted to the lower layer using an airtight adhesive. These thin chambers expand outwards in a balloon-like fashion when pressurised, creating a net bending effect across the length of the actuator [71]. The PneuNet upper layer can be monolithic, where the top and sides of the upper layer are made from singular faces (Figure 2.10 (a)), or segmented, with each chamber showing its own discrete faces (Figure 2.10 (b)).

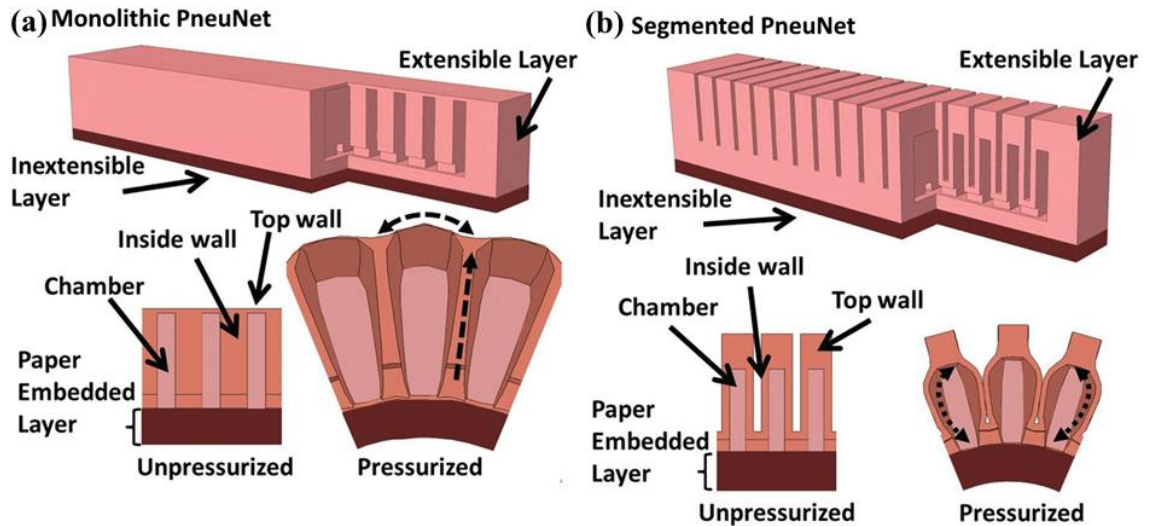


Figure 2.10 Structure and actuation of PneuNets, (a) a monolithic PneuNet geometry and (b) a segmented PneuNet geometry (adapted from [68], © 2014 Wiley).

Much research has been done on characterising the effects of geometric and material variations on the performance of PneuNets [54, 67-70, 72]. The sizes and thicknesses of the various walls, the gaps between the chambers, the shapes of the chambers, the materials used, and the applied pressures all have a significant impact on the dynamic performance of these actuators [68, 70]. Two units of PneuNets may be attached back-to-back along the inextensible layer to allow active bending in both directions, although this decreases the achievable total bending angle [69]. One research group forwent individual chambers altogether, instead using a single chamber which spanned the length of the device and a helically wound thread to mimic the effects of multiple chambers [67, 72]. Most pneumatic network actuators are designed to operate only under positive pressure, but some have been modified to create curling under vacuum pressure [51]. This requires changing the chamber geometry from numerous narrow chambers to fewer wider chambers. When a negative pressure is applied, these wide chambers buckle along the top and side walls, pulling inwards.

The biggest advantage of pneumatic network actuators is their ability to achieve a wide range of bending, curling, and twisting motions [54, 68, 73]. Their multi-chambered design provides many degrees of freedom, allowing PneuNet actuators to easily conform to non-uniform and arbitrary geometric surfaces. PneuNets capitalise on this phenomenon for applications such as grasping or pick-and-place tasks, which may be achieved using one or more actuator units in parallel [67, 69, 70, 74]. Journal articles commonly feature images of PneuNet grippers holding various items such as soft fruit, plastic cups, or irregularly shaped household objects. The total curling of the actuator tip relative to the restrained end is dependent upon the number of chambers and thus the length of the device. PneuNets are often manufactured at a length which allows for full curling at the maximum operating pressure, where the tip has bent far back enough to nearly touch the body [54, 67, 75]. One significant advantage of pneumatic network actuators is the potential for rapid actuation speeds [68, 71]. As the internal air chambers are very small in volume and do

not expand much when pressurised, only a small volume of air needs to be pumped in to produce movement [68]. Similarly, these actuators can operate under low applied pressures, typically between 5 kPa and 50 kPa, depending on the application and geometry [68, 70, 71, 73]. PneuNets can be manufactured to produce higher forces by increasing the wall thickness or material strength, allowing higher pressures to be applied, though this restricts the achievable device strain [68, 69, 71].

Some practical limitations exist for pneumatic network actuators which prevent their widespread use. Primarily, the combination of low actuation pressures, long slender geometries, and soft materials limits the production of force [10, 71]. When the blocking forces of PneuNet actuators were evaluated the maximum applied forces at the tips were reported to be 1.2 N at 45 kPa for a 136 mm length actuator in one study [70] and 1.4 N at 72 kPa in another [68]. When a stiffer thermoplastic elastomer was used, the 150 mm long PneuNet generated blocked forces of 70 N under an applied pressure of 300 kPa [69]. PneuNets, despite being manufactured as finger-like in size and movement, are not perfect analogues for fingers in robotic devices. As overall bending motion is a summation of all the small bending strains along the length of the device, PneuNet fingers are far better suited for wrapping and enveloping large objects than grasping small objects securely or in pinch or tip grips [10, 72].

A major application of pneumatic network actuators is orthotics and rehabilitation devices [10, 54, 69, 70]. The soft compliant nature of these rubber actuators and their ability to conform to arbitrary shapes works well for devices which augment the motions and forces of people with weakened grips. Some particularly novel demonstrations have been performed using pneumatic network actuators, such as the song “Mary Had A Little Lamb” being played on an electronic keyboard by four finger imitating PneuNet actuators [68]. The authors stated they would need to significantly modify the setup in order to play a song with a faster tempo. Similarly, a tethered crawling quadruped prototype whose body is comprised of several PneuNets was also developed [76]. The soft robot’s four legs and spine were formed from separate pneumatic

network actuators and could operate independently of each other, allowing it to crawl under gaps 20 mm tall. This soft robot operated at 70 kPa and could crawl at speeds up to 400 mm.min⁻¹, or 3.2 body lengths per minute [76].

While it is clear that there are numerous advantages to using pneumatic network actuators for certain tasks, they have distinct limitations preventing their wider usage. The small force output relative to volume restricts both the amount of work they can perform and the weight of the payload they can interact with. The other major constraint is only being able to produce bending motions, making them unsuitable for tasks requiring linear or rotational outputs. Fortunately, many niche soft pneumatic actuators have been developed to help fill in areas where pneumatic network actuators are unsuitable.

2.2.3 Various Novel Pneumatic Actuation Concepts

Recent advances in 3D printing and moulding manufacturing practices have expanded the potential for investigating of all manner of hollow elastomeric designs as the basis of soft pneumatic actuators. Flexible rubbers and silicones for moulding such as EcoFlex [5, 12, 21, 54, 67, 71, 76-78], thermoplastic polyurethanes for fused deposition modelling printing such as NinjaFlex and Filaflex [47, 69, 79, 80], and novel resin formulations for digital light projection stereolithography printing [81-84] have been used to fabricate many new soft pneumatic devices. This section will briefly review some of the many recent flexible pneumatic actuators found within literature, arranged by their generated motion type.

Bending

Bending motions are often created across a pneumatic device through anisotropic geometries or stiffness, or through asymmetric loading [11]. This is done by constructing the actuator out of multiple materials of differing stiffnesses, by varying the wall thickness of the pneumatic chambers, or by offsetting the chambers from a central axis. Among the earliest designs was the

flexible micro-actuator (FMA), a silicone cylinder comprised of three internal chambers, split from the centre axis in a Y-shape (Figure 2.11 (a)) [11, 14, 85]. The cylinder was reinforced with nylon fibres to make it flexible but inextensible. Applying pressure in one or more chambers caused a bending deflection towards the opposite side. FMAs could be moulded or printed, and could utilise different numbers of chambers or lengths to vary the bending properties, but were severely limited in terms of the achievable bending angle [11].

Bending motions can also be produced by placing chambers on one side of a pin joint. Depending on the geometry of the actuator, the inflation would either pull the linkages in, decreasing the joint angle, or push the linkages outwards, increasing the joint angle (Figure 2.11 (b)). Soft actuators based off anisotropic stiffnesses can produce a degree of bending deformation by causing one wall to inflate more than another. The non-uniform bulging of the flexible but inextensible walls causes one side to become shorter than the other, pulling the end of the actuator inwards and upwards (Figure 2.11 (c)). De Greef *et al.* [11] provides a comprehensive list of numerous bending actuator concepts.

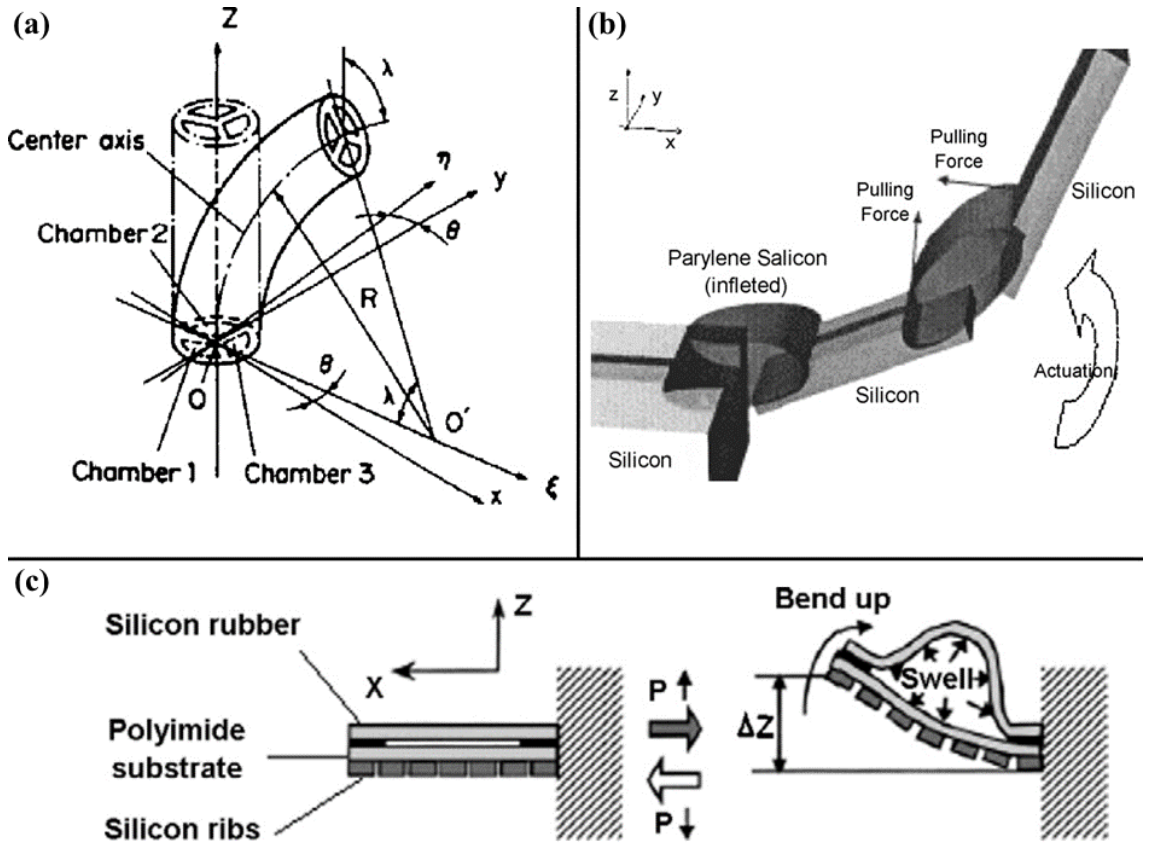


Figure 2.11 Bending actuator concepts: (a) a flexible micro-actuator, (b) a moulded balloon-jointed finger model, and (c) a glued asymmetric balloon actuator (adapted from [11], © 2009 Elsevier).

Torsional

While bending actuators create an angular deflection at the free end relative to an axis placed at the fixed end, torsional actuators generate a rotational motion through the central axis of the device. Torsional actuators typically have a smaller working envelope than bending actuators, thereby requiring less space to perform similar tasks [37, 66]. However, generating pure torsional motion is difficult to achieve, thus rotating devices are often created by utilising other types of actuator motions and redirecting the relative displacements to create a rotation around an axis [66].

One particular example are rotary Peano actuators, which use a network of contractile elements spaced radially around a fulcrum to effect a net rotation [86]. This network is made up of elliptical tubes, joined in series along the edges

of their major axes. Individually, these tubes contract a small amount when inflated, but when arranged helically as a cylinder, the free end twists relative to the fixed end (Figure 2.12) [66, 86]. The rotary prototype presented by Sanan *et al.* [86], measuring 50 mm in diameter and 100 mm in height, was capable of twisting 40° in a single direction under 70 kPa. It could theoretically provide a blocked torque of almost 40 N.m, but the torque decayed rapidly with rotational displacement, dropping below 10 N.m by 10° . These Peano actuators were assembled from multiple inelastic strips using adhesive. As a side effect of the structure, the rotary Peano actuators also generated linear strain in the axial direction, in addition to the desired rotation. This could be mitigated by increasing the stiffness of the device, but the authors added this would negatively affect the range of motion and torque [86]. A similar actuation concept was examined, comprising of two spiral chambers, helically wound with thread, embedded in a silicone cylinder. This torsional actuator, diameter 18 mm height 50 mm, under a 100 kPa input was able to freely deflect 120° , and produce a blocking torque of 0.026 N.m [66].

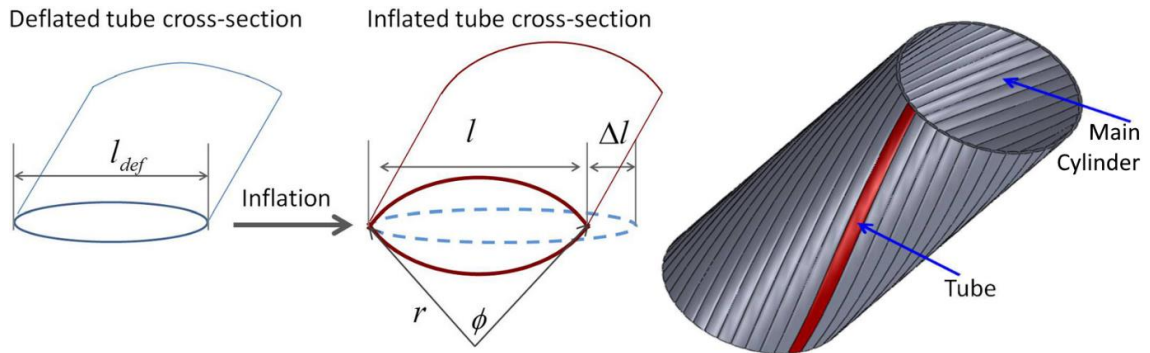


Figure 2.12 Individual Peano element (left) and rotary Peano actuator (right) (adapted from [86], © 2014 ASME).

Rotary soft actuators can be created by constraining a bellows between two pin jointed plates to produce motion [11]. As the pleated bellows expands, it pushes the plates outwards circumferentially, increasing the angle between the plates. Devices based on this technology have primarily been used as rehabilitative motion devices on the larger joints of the shoulders, hips, and legs

[66, 87]. The pleating of materials has also been used to construct extremely lightweight bending actuators. By pleating thin plastic films, 3D trajectories can be reliably created upon pressurisation, from which tentacle-like inflatable helical grippers have been manufactured [88, 89]. These helical grippers operate at pressures up to 10 kPa and can generate substantial forces due to their large contact area. They have demonstrated the ability to lift water bottles of up to 1 kg in the air [88].

A recent innovation in soft torsional actuators involves the buckling of a skewed pyramid under vacuum pressure. Vacuum-powered soft pneumatic twisting actuator (V-SPTA) units use the buckling of an asymmetric thin-walled chamber to produce a relative rotation and contraction across its moulded bulk [90]. A single chamber with an active height of 40 mm when placed under a 70 kPa vacuum can produce 80° of twisting and a contraction of 17.5 mm, with a rise time of 0.47 s (Figure 2.13). It is possible to generate a range of motion types by connecting two differently oriented units in series. Depending on the assembled orientation and geometry of the units, the V-SPTAs can create one of: linear contraction, torsion, or a combination. A highlighted issue was the unidirectional nature of the V-SPTA. The direction of twisting needs to be known before the actuator is fabricated and attempts to move in the opposite direction are limited. Several novel applications were proposed: a flexible wrist, a crawling robot which can turn, a pipe climbing robot, and a propulsion system for a “car” utilising one-way bearings.

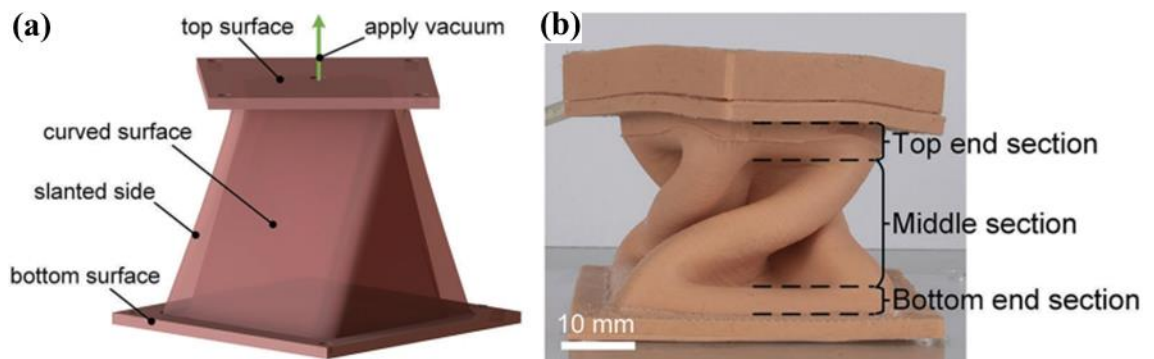


Figure 2.13 Vacuum-powered soft pneumatic twisting actuator (V-SPTA)
(adapted from [90]).

The buckling of moulded elastomeric beams has been found useful in producing a rotation along a soft pneumatic actuator [37]. By placing four elliptic cylindrical chambers in a two-by-two grid, the actuator's core can rotate up to 30° in a single direction under vacuum pressure. Some soft robotic applications were demonstrated using batteries of these buckling actuators, such as a gripper, the propulsion device for a swimmer, and a walking cart.

Linear

Despite the benefits and ubiquity of linear motion devices, there have been few successes in creating soft pneumatic actuators which can deliver robust linear motions [50, 79, 91, 92]. Of those which have been developed, most are operable only in one direction under one type of differential pressure, and can only actively produce either a pushing or a pulling force [50, 79, 90, 92, 93]. These devices rely on passive elasticity and stored energy to return to their initial positions and would require multiple actuators to produce robust antagonistic movement across a joint.

The classic design of the expansive bellows was adapted and transformed into a contractile device capable of applying significant forces, called a HCRPAM [13]. This was done by adding a diamond-shaped band across the ends of the 3D printed bellows, using the other two corners as the unit's attachment points (see Figure 2.14). Additionally, a telescopic rod was embedded in the core to prevent it from bending and the whole unit was coated in a rubber spray to minimise air leakage. When operated under pressures of 300 kPa, a unit of 170 mm \times 53 mm was able to deliver a blocked force of 295 N or a maximum contraction ratio of 65%. It should be observed that the addition of the diamond-shaped framework greatly increased the work envelope required by the actuator. It also has a reduced strain magnitude when compared to the original bellows.

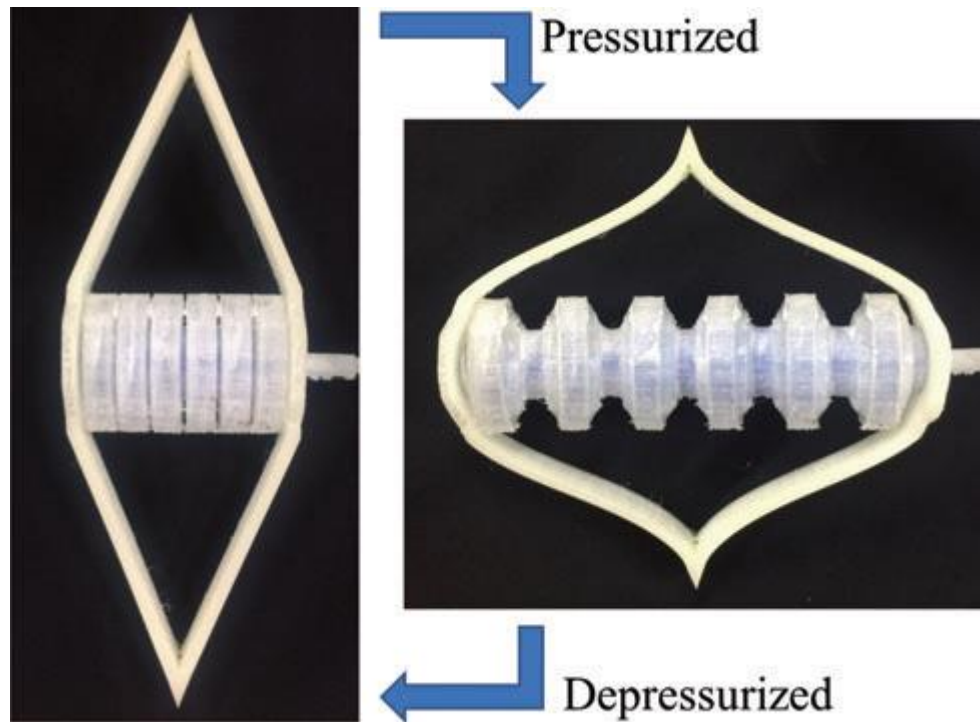


Figure 2.14 Operation of the HCRPAM (adapted from [13], © 2017 Liebert Pub.).

As mentioned previously, Peano actuators are essentially elliptical cylindrical tubes of polymer which contract along their major axis under an applied gauge pressure (Figure 2.12) [86]. This contraction has a maximum theoretical value of 64%, due to the cross-sectional shape transitioning from elliptical towards circular, as the internal pressure seeks to minimise itself by deforming the flexible walls. In practice the contractile strains achievable are far lower, below 20% even at pressures up to 500 kPa, as the applied load tends to deform the thin walled tubes in the opposite direction [93, 94]. Hydraulically activated Peano actuators have shown poor scalability, with a 50 mm long hydraulic Peano actuator shown to have a contractile strain of 12% and a maximum efficiency of 40%, while a 10 mm device could only contract 0.2% with a 2% efficiency [93]. Similarly, a textile-based pneumatic Peano actuator of 200 mm × 200 mm was able to generate blocked forces up to 3.5 kN under 700 kPa of gauge pressure [95].

Other deformation methods for creating contractions in soft pneumatic devices have made use of localised shearing and buckling under vacuum pressures. A moulded silicone trapezoidal soft actuator with multiple trapezoidal chambers was manufactured to cause a pulling force under a gauge pressure of -90 kPa (Figure 2.15 (a)) [92]. By using the obtusely angled corners of the trapezoid as attachment points, the elastomeric walls deform inwards, flattening the actuator and creating a small relative motion at the free end. Similarly, buckling linear vacuum actuators have been created by moulding silicone into a shape which resembles a brick-and-mortar wall. The silicone takes the form of the “mortar”, whereas the “bricks” are voids within the actuator walls. Under vacuum pressure, these voids collapse and get pulled inwards and upwards (Figure 2.15 (b)) [50]. Under a 90 kPa vacuum pressure, the horizontal silicone beams buckle inwards and a net linear contraction of ~40% can be achieved when unloaded.

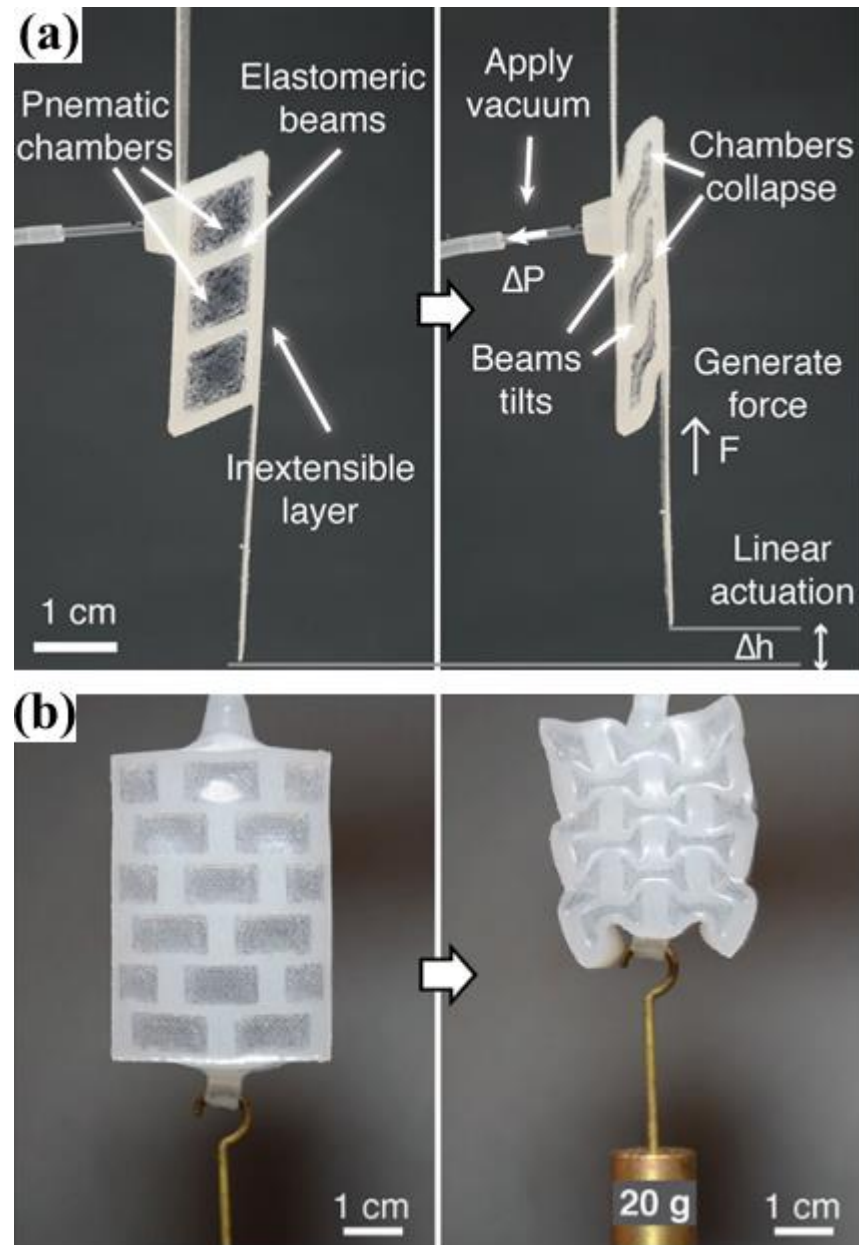


Figure 2.15 Soft linear vacuum actuators: (a) shear-based (adapted from [92], © 2017 Wiley) and (b) buckling-based (adapted from [50], © 2016 Wiley).

There has been good success in the creation of soft pneumatic actuators capable of large elongation strains, owing to the use of high strain silicones in their construction. A low-profile soft actuator manufactured by selectively adhering layers of silicone together (Figure 2.16 (a)) has achieved elongation strains of over 800% and forces up to 20 N at pressures of 20 kPa [96]. The combination of multiple thin layers, wide area, and soft elastomeric material provide these actuators excellent performance characteristics. However, this

structural assembly also results in a significant instability in the balloon-like actuator. Only a small lateral force will cause the free end to tilt away from the central axis, and the output force has a tendency to rebound depending on the applied pressures and testing speeds [96].

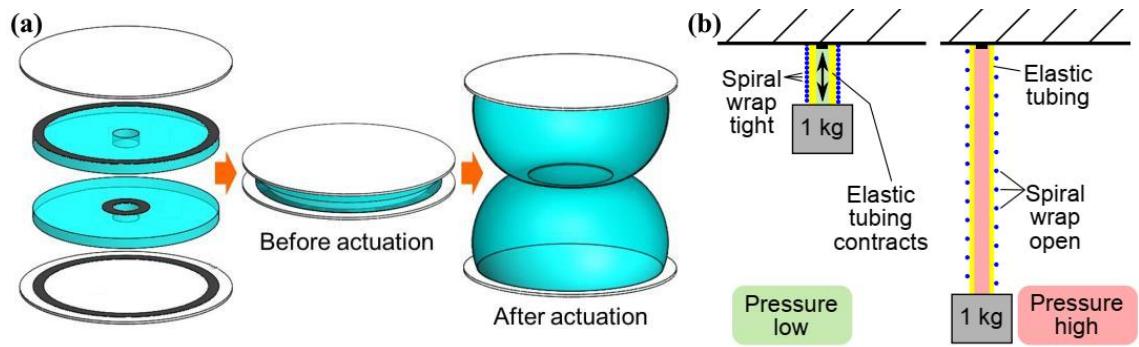


Figure 2.16 Extending soft pneumatic actuators: (a) balloon-like soft actuator (adapted from [96], © 2015 IEEE) and (b) inverse-PAM type (adapted from [56], © 2016 IEEE).

A reconceptualisation of pneumatic artificial muscles has produced an actuator called the inverse pneumatic artificial muscle (IPAM), which can produce linear strains up to 300% (Figure 2.16 (b)) [56]. A thin stretchable latex tube was wrapped in a spiral wound inextensible fibre and absorbs energy as pressures up to 600 kPa were applied and the tubing elongated. The stored energy was used to contract the device and payload upon the release of the pressure. This method of actuation is different from most other actuators, as this actuator's intended work output comes from not the application of energy in the form of pressure, but from the removal of the pressure resulting in the elastic return to the initial state.

Some novel linear pneumatic actuators have been proposed featuring geometries of various folds, ripples, and bellows-like chambers [97]. These actuators were FDM printed using a polyamide material, the stiffness of which limited the maximum obtainable strains to below 20%, despite applied pressures of up to 300 kPa. The authors highlighted the lack of material deformability limiting the achievable displacements.

The linear soft vacuum actuator (LSOVA) produces linear contractions under applied vacuum pressures of -96 kPa (Figure 2.17) [79]. These actuators are 3D printed using fused deposition modelling (FDM) from the commercially available thermoplastic NinjaFlex, an off-the-shelf thermoplastic polyurethane filament with an elongation at yield of 65% and a tensile modulus of 12 MPa [98]. The LSOVA design has excellent potential for scaling both stroke and force by altering the number of chambers and diameter of the chambers, respectively. A one chamber LSOVA of 20 mm face diameter had a maximum contraction strain of 38%. Regardless of the number of chambers, all reported actuators with 20 mm face diameters reported similar blocked forces of approximately 27 N at 96% vacuum.

The LSOVA design reports to be an improvement over several other vacuum actuators in terms of blocked force, rise time, actuation bandwidth, and lifetime. As these actuators are scalable and have a reliable linear relationship between applied pressure and blocked force, they are tailorable for numerous proposed human-machine interfaces and soft robotic applications. Robotic devices utilising LSOVAs have been demonstrated, including pipe crawling robots, parallel manipulators, and artificial muscles for elbow joints and underactuated fingers.

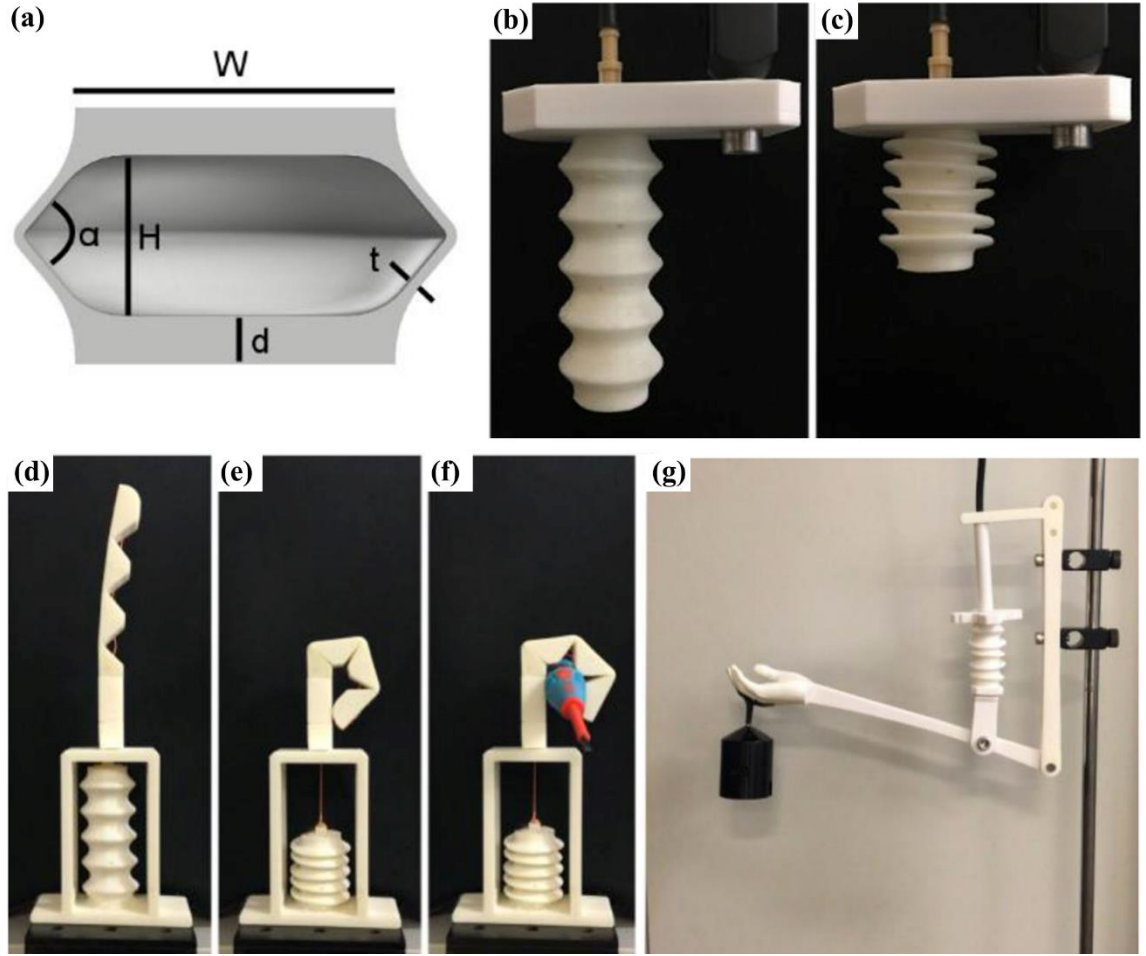


Figure 2.17 Linear soft vacuum actuators (LSOVA): (a) cross-section of a one chamber LSOVA, (b) five chamber LSOVA unpressurised, (c) five chamber LSOVA under -96 kPa, (d) soft finger in open position, (e) soft finger in closed position, (f) soft finger grasping a screwdriver, and (g) LSOVA-based elbow joint (adapted from [79], © 2019 IEEE).

A theme consistent throughout these published works is the lack of suitably soft materials for developing new soft pneumatic actuators. Researchers have so far been forced to choose between two approaches, either using soft elastomeric materials in moulding techniques and be limited to simple geometries, or create detailed parts and geometries using 3D printing methods, but be restricted to the available stiffer thermoplastic materials. It has also been highlighted that the material stiffness limits the achievable strains of soft pneumatic actuators while also requiring higher pressures to operate.

Additionally, most soft pneumatic actuators are operable by only one type of differential pressure and in one direction, relying on passive material restoration to reverse the applied strains. An objective of this thesis is to provide a way to combine the benefits of both approaches by developing a new 3D printable material which can be used to form soft elastomeric parts of intricate designs. In order to do so, 3D printing methods and material science must first be understood.

2.3 3D Printing

Additive manufacturing, more commonly known as 3D printing or rapid prototyping, has seen a surge of interest in both commercial productions and novel research applications in recent years. When compared to traditional manufacturing processes, such as machining, moulding, and joining, 3D printing has some very desirable advantages. Additive manufacturing allows for a rapid development of low cost parts, which can contain highly complex geometries and internal hollows which are difficult or impossible to achieve through traditional methods [8, 16, 40]. These parts can be created as a single monolithic piece, removing the need for assembling multiple pieces using external fasteners or adhesives. Computer-aided design (CAD) programs allow for early prototypes to be constructed and visualised, fast-tracking the optimisation and manufacture of products [39]. Aside from the removal of support structures and unused material, there is typically little post-processing required. The development of new materials and printing methods is expanding the potential of this field for the production of new and unique designs and device applications [99].

2.3.1 3D Printing Technologies

The following are the most common and commercialised forms of 3D printing technologies, although there are more niche methods in the early stages of development. These technologies are fused deposition modelling (FDM), material jetting (MJ), selective laser sintering (SLS), and

stereolithography (SLA). The first two technologies are material deposition based, while the other two use selective light projection methods to cure or sinter parts (Figure 2.18) [99, 100]. Interestingly, only FDM directly uses thermal energy sources in its formation of polymeric parts, the others all use radiation-based energy as the primary energy source.

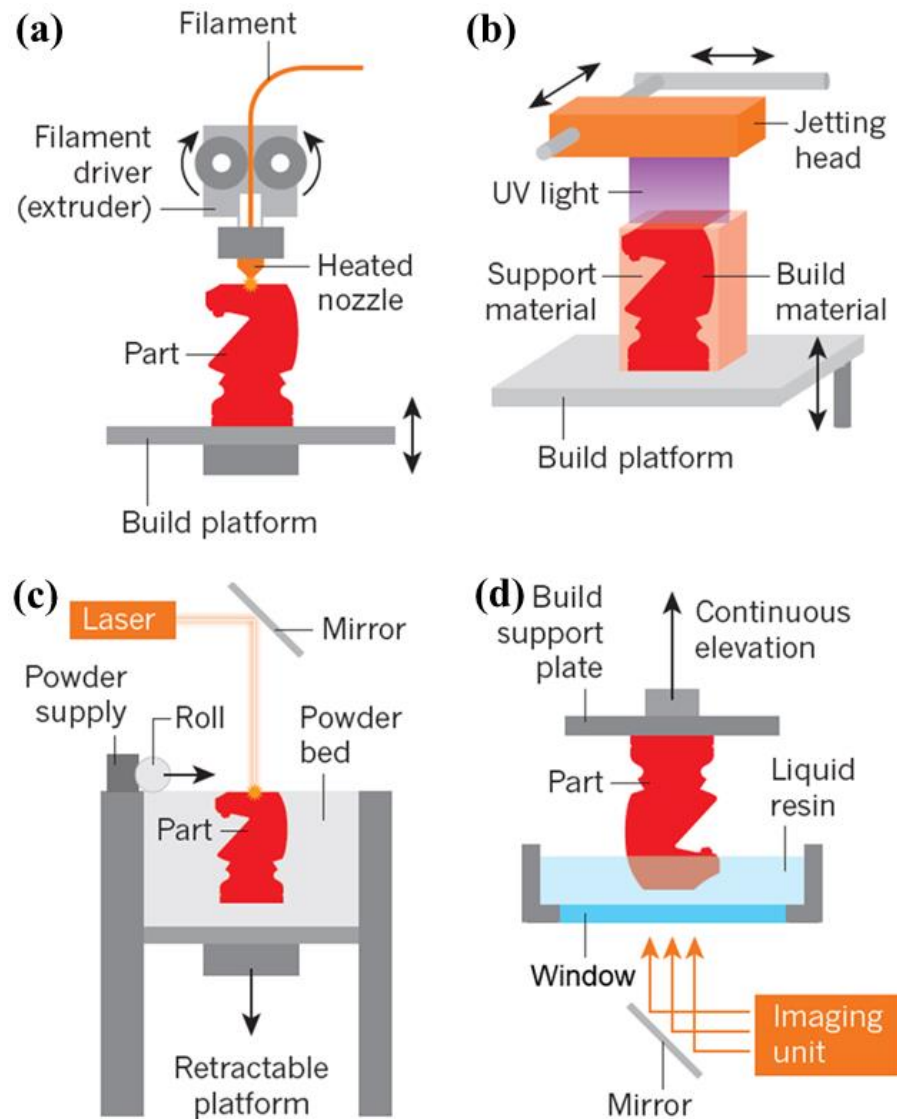


Figure 2.18 Common ink- and light-based 3D printing methods: (a) fused deposition modelling, (b) material jetting, (c) selective laser sintering, and (d) digital light projection stereolithography (adapted from [99], © 2016 Nature).

Fused Deposition Modelling

Fused deposition modelling was the first widely successful additive manufacturing technology, boasting a low machine cost, cheap materials, and easy operation (Figure 2.18 (a)). FDM can print several polymeric materials, such as acrylonitrile butadiene styrene (ABS), polylactic acid (PLA), and polycarbonate (PC), but is limited to thermoplastics [8, 99]. The filament is fed through a heated nozzle, which melts the polymer material and is extruded onto a build plate in the desired pattern [99]. The printer moves the nozzle and plate in three dimensions, effectively drawing the part in lines, layer by layer. This deposition-based method can print multiple materials at once by using multiple nozzles, whereas the vat-based and light-based technologies are restricted to using one medium at a time.

Due to the parts being built one line at a time, often the layers do not completely solidify into an impermeable wall, making the creation of airtight parts difficult [69, 101]. The nozzle diameters are most commonly 0.4 mm, greatly limiting the resolution of FDM printers [8, 80, 98]. Additionally, it is common for undesired trails of material to be created when the nozzle travels between locations, known as “dropped threads” due to the thread-like appearance.

Material Jetting

Material jet printers build parts through the spraying of two UV curable inks from separate jet heads, one a functional material ink and the other a support material ink (Figure 2.18 (b)). The printing process alternates between spraying these inks onto the previously cured material and curing the layers using UV light source [99, 102]. The post-processing removal of the support material involves the spraying of high-pressure water or the use of a harsh solvent. Neither of these methods are particularly effective at cleaning small internal voids or channels [103]. Material jet printers usually have feature resolutions between those of fused deposition modelling and stereolithography, and have much fewer commercially available material options [101]. The most

flexible commercial material is TangoPlus by Stratasys, which has an elongation at break of 170% and an ultimate tensile strength of 0.8 MPa [104].

Selective Laser Sintering

Selective laser sintering (SLS) utilises a high-powered laser point and a series of mirrors to fuse fine powders together (Figure 2.18 (c)). These powders, which can be metallic or polymeric, absorb the laser energy as heat, causing the grain boundaries to grow and merge into a larger continuous product in a process known as sintering [99, 101]. This occurs at a temperature below that of the material's melting point and is different to melting and resolidifying the powders. The unfused material acts as a support network during printing, eliminating the need for the construction of supports. After each layer is fused, the platform is lowered and a new layer of powder is dispersed over the top. SLS printing has the coarsest obtainable resolution of these four reported printing technologies, exceeding 100 μm [99]. Additionally, sintering results in an intrinsically porous network of material which has weaker mechanical properties than the continuous networks created by other processes.

Stereolithography

Stereolithography (SLA) involves the projection of patterned light onto a liquid photocurable resin. Originally, the technology used a single discrete point of light or a laser to raster the image, similar to SLS [100]. A newer method has evolved from this, known as digital light projection (DLP) lithography, which projects 2D images to cure the resin into polymer, one layer at a time, to progressively fabricate the 3D component (Figure 2.18 (d)) [82, 99]. The projected light, often at or near the UV spectrum, initiates the curing process. Once a layer is solidified, the printer moves the part so that more liquid resin fills the space for the next layer. As DLP bonds an entire layer at once to the preceding under-cured layer, the result is a continuous network of polymer chains, a major advantage over FDM [99, 101]. The build area and resolution of the part depend upon the light source of the printer, with scalable XY

resolutions of 14 μm to 100 μm being readily achievable with currently available commercial DLP printers, outperforming all other 3D printing methods [8, 99, 105]. Surface quality is affected by the layer step size, where larger layer heights result in a more visible stair-stepping phenomenon [106]. Unlike FDM printing, the orientation of the printed part and hence the print direction does not significantly affect the stress-strain properties of DLP printed parts [83, 100].

The SLA resins commercially available are mostly acrylics and epoxies, hard or tough plastics intended for structural purposes, with only a few providing adequate flexural abilities. Two of the most flexible commercial DLP resins fail at strains well below 200% and behave more like a polyamide material rather than an elastomer [82, 107, 108]. The biggest limitation to the creation of soft actuators using DLP is the lack of suitable materials currently on the market. Despite researchers long being aware of this distinct lack of suitable materials, there has been limited progress to address this need, thus novel materials are often synthesised by researchers in order to explore the vast potential [8, 55, 81, 82, 85, 99]. A DLP SLA printer was acquired for use in this thesis to create new resins and actuators due to its extremely high resolution and potential for good resin properties.

2.3.2 Photopolymer Resins

The creation of complex elastomeric parts using traditional forming methods is often problematic at best, with SLA printing promising an alternative for the production of complex elastomeric components, opening up many areas of research for enhancement [8, 16, 40, 83]. While there are numerous stiff and strong resins designed specifically for SLA printing available commercially, there are remarkably few resins capable of exhibiting an appreciable degree of elasticity and flexibility, with many authors remarking about this limitation [55, 82, 85, 105, 109-111].

One of the few resins marketed as flexible, is known as Spot-E (Spot-A Materials). It claimed to provide up to 65% elongation at break, with an elastic modulus of 12 MPa, and a viscosity of approximately 100 mPa.s at 25 °C [82,

108, 112]. Despite this resin having a reasonably low viscosity for easy printing, its useful strain is far below those of conventional elastomers, which exhibit reversible strains between 100% and 1 000% [83, 113]. Similarly, the most stretchable resin available from another large manufacturer (Elastic 50A by Formlabs Inc.), has a maximum elongation at failure of 160%, a modulus of 1.59 MPa, and a viscosity of 2 950 mPa.s at 35 °C [114]. The other soft resin produced by Formlabs, called Flexible, fails at 80% elongation, exhibiting a viscosity of 4 500 mPa.s at 25 °C and a cured tensile strength of 8 MPa [107, 115]. Thus, as the focus of this thesis is the creation of highly elastomeric pneumatic actuators, the current commercially available resins were deemed unsuitable, and it was imperative to formulate a new resin [55, 82, 83, 85, 110, 116].

This posed a significant challenge, as most manufacturers refrain from publishing the compositions or synthesis methods to protect their proprietary 3D printable resin formulations [83, 108, 110, 117]. Furthering this was the fact that most base resins on the market are intended for solid protective coatings and applied to surfaces by rolling, die press, or immersion [118]. These products hence lack adequate strains, have viscosities far too high to be 3D printable, or are premixed with high frequency photoinitiators [82, 119, 120]. As remarked in a study published more than two decades ago, a key technical issue with the advancement of SLA printed flexible pneumatic devices is the development of an adequately strong and flexible resin of low viscosity [85]. Indeed, as Skov and Yu [121] stated “one can claim that processing issues can always be overcome, but working with high-viscosity polymers is simply not easy”.

The reduction of resin viscosity for micro-fabrications is key to achieving precise geometries and to allow proper rinsing of the uncured resin from the solidified component [85]. Lower viscosities also better facilitate the recoating of the printer vat between printing each layer, reduce the separation forces during the peeling stage, and decrease the likelihood of damage to the part and the vat [122]. Though there has been some success with custom resin formulations with

viscosities up to 5 000 mPa.s, most commercial resins for DLP printing have viscosities below 1 000 mPa.s, with literature often citing this as a threshold for good printability [112, 115, 116, 122-125]. The viscosity of a fluid is a complicated function of molecular weights, chain entanglement, intermolecular forces, and temperature, therefore it is not possible to accurately estimate a resin's viscosity using the known viscosities and ratios of the individual starting materials [106, 126]. Despite the potential for the stereolithographic fabrication of elastic parts, there have been minimal improvements in commercial SLA resins to provide high elastic strains at low viscosities.

2.3.3 Base Components of Resins

Light-curable resins are comprised of one or more oligomers or monomers in addition to a catalysing agent called the photoinitiator [127]. The large molecular weight of an oligomer tends to form the majority of the cross-linked polymer and thus has the greatest effect on the material properties. The monomers are much smaller in size, tending to have a smaller influence on the cured polymer's mechanical properties than an included oligomer. Monomers may be added to an oligomeric mixture to reduce the resin viscosity in addition to altering the properties. As monomers and oligomers cannot produce sufficient reactive species under normal exposure conditions, a light sensitive photoinitiator is added to catalyse the polymerisation process [128]. Sometimes a photosensitiser or a co-initiator is included with the photoinitiator to assist the curing of some monomers [104, 128]. Further additives such as dyes, pigments, or fillers may be optionally added to adjust various properties of the resin or the cured polymer [119, 127-130].

Oligomers generally comprise the largest proportion of a photolithographic resin by weight, therefore having the largest influence on the material's mechanical properties [127]. Oligomers are differentiated from monomers on a basis of being comprised of many repeating units and having a significantly larger molecular weight [119, 131]. These long molecules have a much higher viscosity than the other components of a resin, often in the orders

of thousands to hundreds-of-thousands of millipascal-seconds at room temperature. The core of these photopolymer building blocks may be comprised of urethane, epoxy, polyether, or polyester chemical units (see Figure 2.19). One of the most commonly used types are the urethane acrylates, which have a vast number of possible structures and formulas, allowing for tailorable combinations of high strength, modulus, and strain at break [119, 129, 132-135].

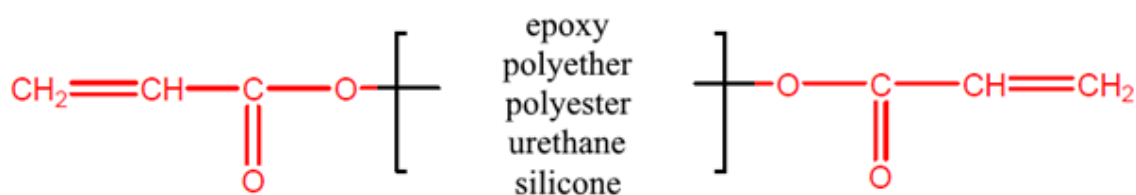


Figure 2.19 General chemical structure of common acrylate (red) terminated oligomers.

A particular class of these urethane acrylates, known as aliphatic urethane diacrylates, is capable of producing elastomeric materials with a high degree of conversion [129]. The urethane chemical group is special in that the smallest urethane unit is formed from the synthesis of a multifunctional isocyanate with a multifunctional alcohol (polyol), often occurring in longer oligomer chains as polyurethane (see Figure 2.20). The physical and chemical properties of the polyurethane highly depend on the size, composition, and reactivity of the functional groups used in the original isocyanates and polyols [136, 137]. The isocyanate compound forms the hard strong segments in the polyurethane, whereas the polyol contributes to the soft, flexible segments [134-138]. Therefore, without explicitly knowing the molecular weights and structures of the constituent compounds of a polyurethane oligomer, it is impossible to predict the nature of the cured material. For further reading on elastomeric polyurethane classification, formulation, and analysis, this author recommends *Polyurethane Elastomers* by C. Hepburn [135].

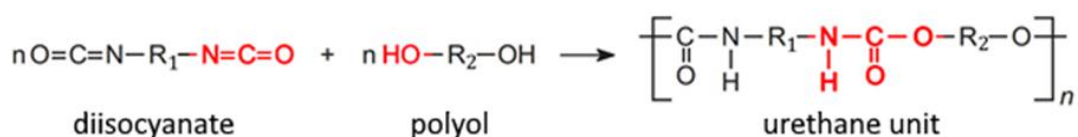


Figure 2.20 n monomers of a diisocyanate reacting with n monomers of a polyol to create a polyurethane of chain length n . Singular functional groups highlighted in red.

Monomers are classed as a separate type of compound to oligomers and typically have a lesser influence on the mechanical properties of the cured material and on the fluid properties of the uncured resin [133]. The monomers most commonly selected for use in photopolymer resins are unsaturated, containing at least one carbon-carbon double bond, and may be acrylate, methacrylate, unsaturated polyester, or thiol-ene based [127]. Monomers with a single carbon-carbon double bond, called mono-functional monomers, can provide a greater reduction in resin viscosity, cure as a more flexible polymer, and have a higher degree of conversion, in comparison to di- and tri-functional monomers (Figure 2.21). However, mono-functional monomer polymerisation requires more time to cure, can have greater adhesion to the substrate, and can be more susceptible to certain solvents [119, 123, 127, 132, 139].

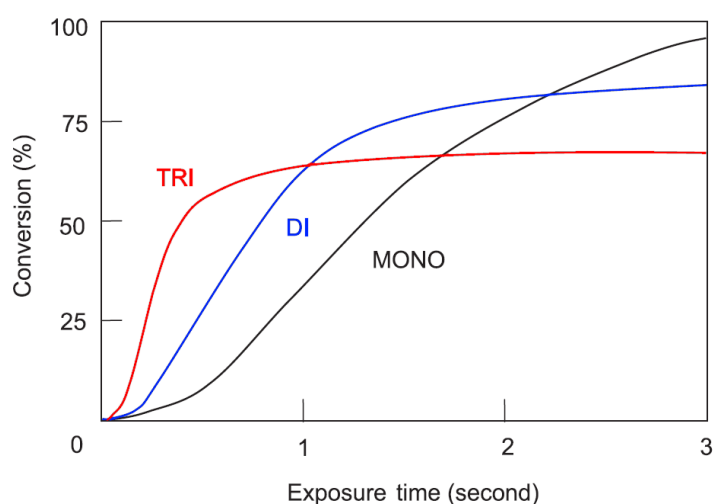


Figure 2.21 Generalised influence of monomer functionality on the conversion ratio and cure times of a urethane acrylate resin (adapted from [133], © 2001 Emerald Insight).

Acrylate-based monomers are frequently used in photocurable resins due to the high reactivity of the double bond, low viscosity, low volatility, and being widely available in many forms at moderate costs (Figure 2.22). Isobornyl acrylate (IBOA) is a mono-functional aliphatic monomer which exhibits a high degree of conversion and excellent flexibility in the cured material [82, 118, 122, 126, 127, 129, 140]. The mono-functional 2-hydroxyethyl acrylate (HEA) has also seen some use in photocuring resins, displaying good effects on elasticity and can reduce oxygen inhibition effects [83, 109, 140]. Another common reactive diluent is that of 1,6-hexanediol diacrylate (HDDA), a di-functional monomer that exhibits high diluent potential, good flexibility, and a high degree of conversion (up to 100%) [118, 126, 127, 129].

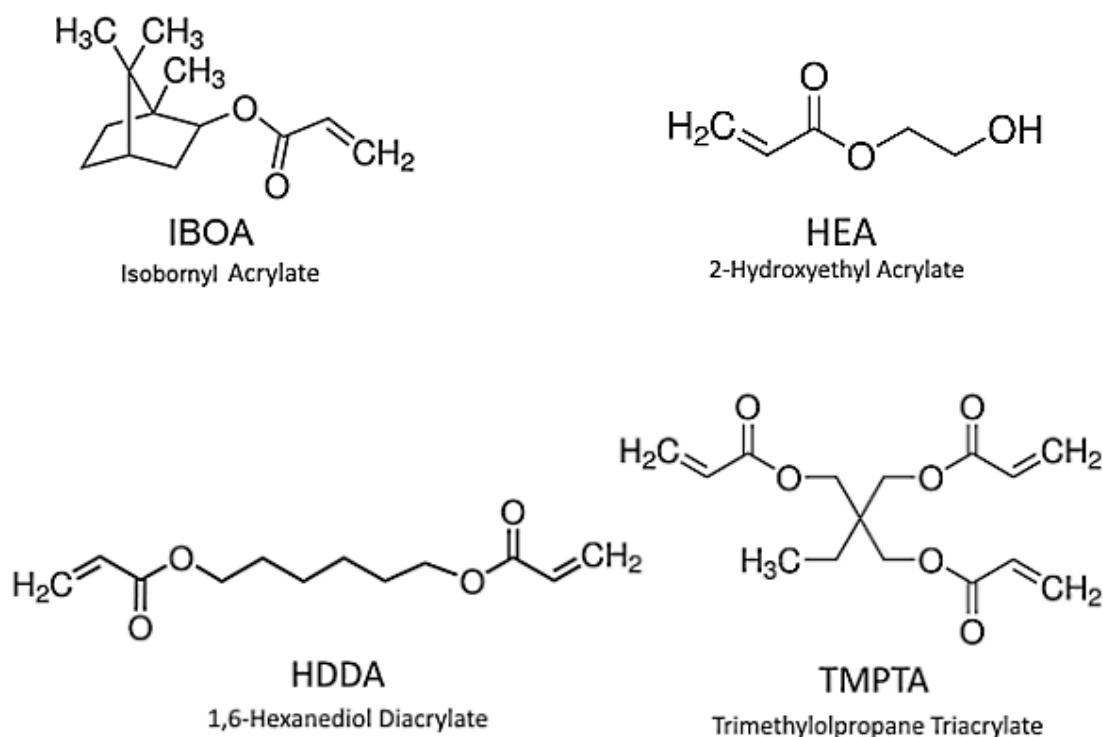


Figure 2.22 Chemical structures of common diluent monomers.

Material hardness and ultimate tensile strength increases in materials depending on the monomer functionality, with the greater increases at higher functional levels, due to multifunctional monomers producing higher cross-

linking densities [122, 139]. Methacrylate-based monomers have a bulky pendant group which limits polymer chain mobility, resulting in a higher modulus and lower potential elongation whilst also requiring a longer exposure time to cure compared to acrylates [111, 127]. The drawback to using acrylic monomers is that they have a relatively large shrinkage during polymerisation and post-curing, potentially resulting in internal material stresses, warping, or fracture [122, 127, 141]. Reactive diluents are preferred over non-reactive solvents as they are converted during curing and therefore do not become emissions [118, 123].

Photoinitiators are used as a reactive catalyst in the photocuring process. They absorb radiant energy from a light source to form the free radicals used in the polymerisation of the monomers [128]. These free radicals react with the double bonds of the monomer acrylate groups, opening them up to begin the chain propagation of the polymer [129]. Some of the most common photoinitiators used in industry are diphenyl(2,4,6-trimethylbenzoyl)phosphine oxide (TPO), phenylbis(2,4,6-trimethylbenzoyl)phosphine oxide (BAPO), and camphorquinone (CQ) (chemical structures shown in Figure 2.23) [110, 128]. The absorbance of incident light by a photoinitiator in a solution can be expressed using the Beer-Lambert law:

$$A = \varepsilon b c \quad (2.1)$$

where A is the absorbance (unitless), ε is the wavelength-dependent molar absorptivity coefficient for the photoinitiator ($\text{L.mol}^{-1}.\text{cm}^{-1}$), b is the path length (cm), and c is the concentration of the photoinitiator in the solution (mol.L^{-1}) [127, 128, 142, 143]. This equation can be used to calculate the required concentration of a monomer to achieve a desired absorbance for a known cure depth, or vice versa [143]. The spectral absorption curves for the aforementioned photoinitiators are shown in Figure 2.24. Efficient DLP printing requires a good overlap of the photoinitiator absorption spectrum with that of the light source's emission spectrum [144]. Poor correlation between these spectra requires longer exposure times, otherwise under-curing could occur.

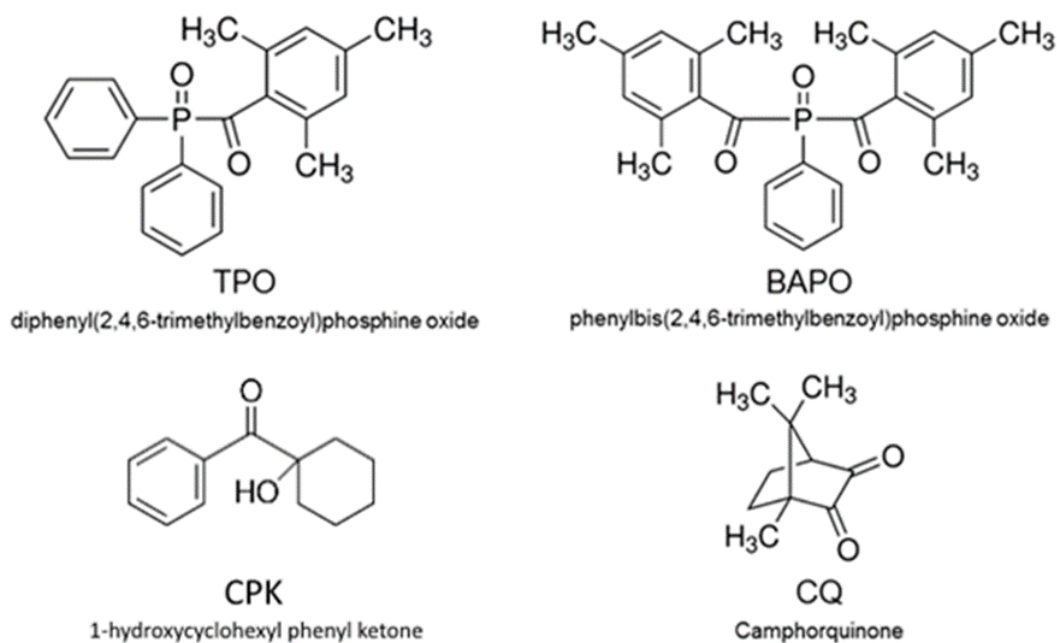


Figure 2.23 Chemical structures of Type I photoinitiators TPO, BAPO, and CPK, Type II photoinitiator CQ.

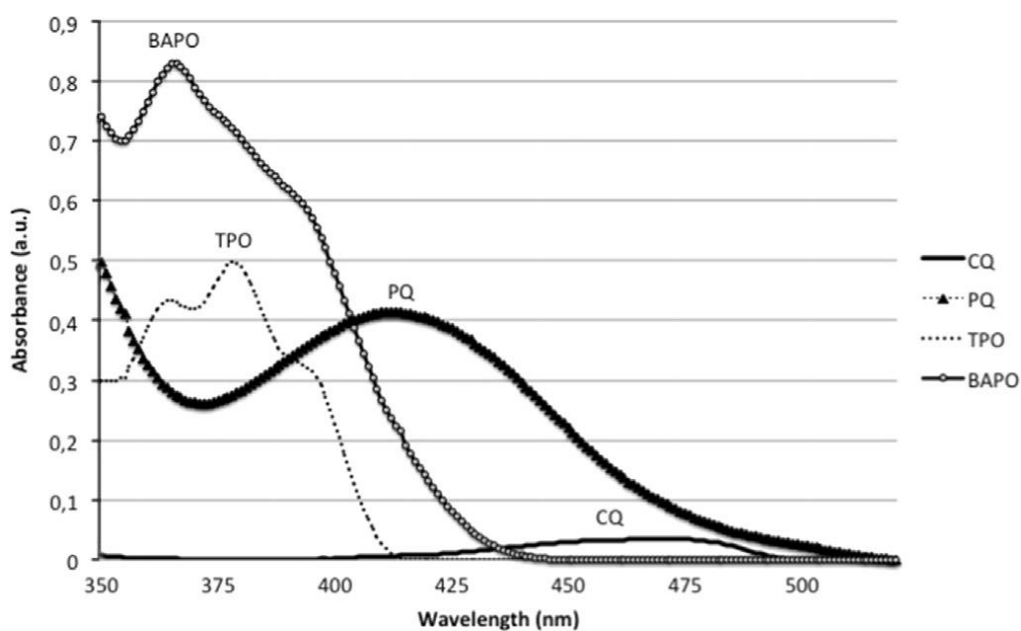


Figure 2.24 Relative spectral absorbance values for several photoinitiators at a concentration of 0.25 mol% (adapted from [145] , © 2015 Elsevier).

The photoinitiator TPO has a high absorbance at wavelengths below 400 nm, with a local maximum near 380 nm, and slight absorbance in the 400 nm to 420 nm range (Figure 2.24) [146]. It can produce a high degree of

conversion in many resin compositions, small depth of cure at moderate concentrations, good solubility in a number of diluents, and low yellowing in comparison to BAPO and CQ [16, 142, 147, 148]. However, TPO is highly susceptible to oxygen inhibition, which can result in the surface being under-cured and becoming tacky during the photocuring process if cured in air or there is a high concentration of dissolved oxygen in the resin [105, 128].

Another commonly used photoinitiator is BAPO owing to its wider absorption characteristics. It has a spectral absorbance range up to 450 nm, allowing it to cure using visible light emissions [149]. In addition, it has a higher extinction coefficient than TPO, providing more activation sites to create free radicals and allowing for a faster curing speed if used in equal concentrations [149]. Unfortunately, the chemical BAPO exhibits poor solubility in diluents due to its symmetric structure, has a lower degree of conversion when compared to TPO, and causes significant yellowing in polymers [147, 149].

A photoinitiator which has found frequent use in the dental materials industry is camphorquinone, which, due to its absorption spectrum extending through blue light, is compatible with non-UV-emitting blue light sources [130, 145]. Its absorption spectrum is effective in the range of 420 nm to 495 nm with a local maximum near 470 nm, but has a significantly lower absorption magnitude throughout [130]. Additionally, CQ requires the inclusion of a co-initiator for photoinitiation to occur, whereas TPO and BAPO do not. The inclusion of co-initiators can act as retardants in some mixtures, decreasing the degree of conversion and generating by-products during photoreaction [130, 145, 147].

The inclusion of pigments or dyes to a resin affects the transmission of light through the liquid in addition to colouring the product. The distinction between pigments and dyes is that pigmentation adds tiny insoluble suspended particles to the resin, whereas dyes dissolve entirely within the resin and are somewhat translucent [150, 151]. These additives are used to reduce the transmission of light energy which would otherwise pass through the material. This prevents curing in undesired locations, effectively throttling the depth of

cure and improving fine detail accuracy without needing higher photoinitiator concentrations [125, 128, 143, 152].

Pigments reduce the transmission of light by absorbing, reflecting, or scattering the photons, whereas dyes can only absorb [150]. Pigments partially absorb light depending on their colour, with discrete “windows” occurring where the light transmission is significantly higher and more light is available for the photoinitiator [128]. The transmission spectra of certain pigment colours are shown in Figure 2.25. It can be seen that white pigments offer excellent transmittance above 390 nm, and therefore provide a very efficient cure when combined with a phosphine oxide such as TPO [128, 150]. On the other hand, carbon black pigments may be chosen due to the small transmittance across the spectrum, minimising the light penetration. It is recommended to use the minimum amount of pigment necessary to achieve the desired colour or the reduction in light penetration to ensure effective curing [128]. Thus, the degree of cure and the depth of cure are both dependent on the Z-resolution, light exposure, and concentration of absorbent compounds (photoinitiator and pigment) [129, 147]. These three factors must be optimised in conjunction with one another to achieve the desired curing profile [143].

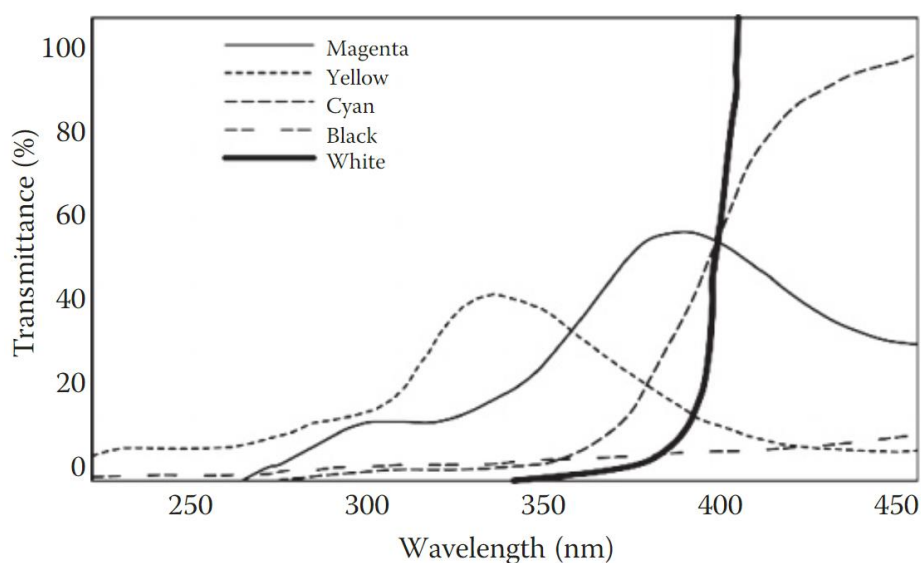


Figure 2.25 Pigment colour transmittance of a spectra of light (adapted from [128], © 2010 CRC Press).

In a study into the inclusion of unnamed colour additives into an unnamed elastic adhesive resin by Suzimori *et al.* [85], it was found that side-curing width and solidification depth both decrease with an increasing of colour density. Upon the tensile testing of these materials, it was observed that the compounds with higher pigment concentrations were stiffer and exhibited lower elongations before breaking [85]. This weakening of the polymer occurs because the pigment molecules are separate from and interspersed between the polymer chains. Clear materials can be produced if a fluorescing optical brightener or photoabsorber chemical is used in place of a pigment [84, 100, 101, 106, 128]. Photoabsorber inclusion has been shown to negatively affect a material's mechanical properties, most significantly the stretchability of the elastomer, making them unwise for use in soft pneumatic actuators [84].

Other resin additives may include: fillers of silica particles to give mass or increase the tensile strength of the cured resin [105, 148]; crosslinking agents to increase polymer chain crosslinking and increase material strength and elastic modulus [109, 113, 123]; and co-initiators to be used in conjunction with certain types of photoinitiators [145, 147]. The addition of oil has been suggested to reduce the viscosity of a mixture by softening the interactions between particles, though these non-reactive and non-volatile compounds decrease the degree of conversion of the resin and result in a more porous part [121].

The general method for the preparation and synthesis of resin formulations for DLP UV printing is essentially a batch process of combining the photoinitiator, monomers, and oligomer together in a vessel and mixing. The apparatus commonly used in the synthesis process are a round-bottomed flask, a temperature-controlled water bath, a mechanical stirrer, and an atmospheric regulating device, sometimes with a device to add the monomer dropwise. The oligomer is often preheated to reduce its viscosity and flow easier. Mixtures are typically held at temperatures between 50 °C and 90 °C throughout the mixing, lasting several hours to ensure a homogenisation depending on the type and amount of chemical compounds [82, 117, 139, 153-155].

155]. The photoinitiator can be added in a ratio of 0.25% to 5% (wt/wt) versus the combined monomers and oligomers [83, 100, 116, 123, 129, 142, 146, 154]. If bubbles form within the viscous resin during mixing, they can be removed using a vacuum chamber [123].

The general process of curing photosensitive resins through UV radical polymerisation involves three stages: initiation, propagation, and termination [128, 132]. During the initiation stage the resin is irradiated by a light or UV source and the photoinitiator absorbs energy from specific wavelengths of the incoming light. Depending on the functionality of the photoinitiator, one or more free radicals are formed per photoinitiator molecule. These radicals then interact with the double bond of an oligomer or monomer, forming a new radical species and the basis of the growing polymer chain. The propagation stage, like the creation of most polymers, is a chain reaction occurring cyclically as the polymer chain grows. Radicals located on the edge of the polymer chain react and join with other oligomer or monomer molecules, extending the chain and generating a new free radical location. Termination occurs when two separate radicals combine, being either two growing chains meeting, or the end of one chain combining with another photoinitiator radical. If the concentration of photoinitiators is too high in the resin, it may lead to a high termination rate of polymer chains. This can result in a smaller chain lengths and low molecular weights, or a large amount of unreacted material, thereby the polymer will exhibit poor physical properties [119, 127, 128, 132].

2.3.4 Factors Affecting Curing and Material Properties

The concentration of the photoinitiator within the resin also affects both the cure depth and the cure speed [133]. If the concentration is high enough, the majority of the incident energy will be absorbed near the surface, rapidly curing a shallow layer (Figure 2.26) [128, 129, 142]. This extreme curing may create surface wrinkling due to differential shrinking through the material and result in highly variable polymer chain molecular weights [128]. In contrast, a lower photoinitiator concentration produces fewer radicals, resulting in fewer

polymer chains, higher molecular weights, and smaller weight deviations [128]. Considering this information in the scope of SLA printing, the amount of photoinitiator used in the resin formulation should be carefully considered, as it is desirable to obtain long and elastic polymer chains but also to minimise unwanted light penetration between layers.

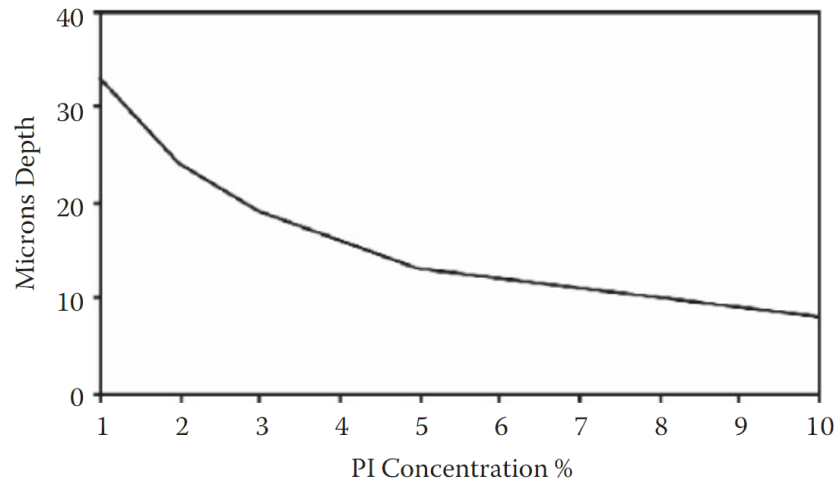


Figure 2.26 The effect of the concentration of the photoinitiator on the cure depth of a resin (adapted from [128], © 2010 CRC Press).

One of the main factors affecting the degree of conversion of a resin is the radiant exposure ($\text{J} \cdot \text{cm}^{-2}$); the amount of energy transmitted in the projected light across a certain area [100, 119, 130, 148]. Radiant exposure is a function of irradiance ($\text{W} \cdot \text{cm}^{-2}$) and irradiation time (s). The width and depth of a cure through a resin are directly affected by the exposure characteristics [84, 156]. That is not to say that, assuming an equal magnitude of radiant exposure, a low irradiance over a long period of time would create the same cure pattern as a high irradiance in a short burst [106, 148, 156]. Similarly, doubling the exposure time would not double the cure depth through a resin. Furthermore, it has been shown that higher intensity irradiations for shorter periods produces a higher degree of conversion in TPO resins for the same radiant exposure, but the opposite was shown for CQ [148, 156]. The importance of matching the light

source characteristics to the type and absorption profile of the photoinitiator has been highlighted by several studies [84, 119, 142, 145].

The physical geometry of the light source and various optical transmission components further complicates the achievement of a uniform cure. These components typically produce slight non-uniform distributions in the intensity of the projected light [106, 130]. This non-uniformity creates small spatial variances in curing rates, depth of cure, degree of conversion, and mechanical properties [106, 130]. Some printers have the option to apply a “mask” to the projected image pattern: dimming specific pixels in accordance with their normalised brightness to account for the non-uniformity of the projected light. This provides a more uniform projection but lowers the irradiance. It is important to note that a complete degree of conversion is difficult to obtain through primary irradiation alone, but can be improved through post-printing processes [148]. Post-curing in direct sunlight or under a constant source of UV light for up to an hour is often performed to cure the residual resin [82, 100, 116, 148].

A resin’s viscosity directly affects its printability and the mechanical properties of the cured polymer. A lower viscosity improves the surface quality, reduces the print time, and makes post-cure cleaning easier [85, 124, 157]. Viscosity reduction can be achieved in two ways: diluting the resin and heating the resin throughout the printing process [82, 85, 116, 118, 124, 157]. As highlighted previously, the use of diluent monomers also influences the chemical structure and mechanical properties of the final product, and too extreme diluent concentrations can weaken the polymer [116, 118]. Most liquids, resins included, tend to have negative exponential-like viscosity responses to increasing temperatures as well as diluents (Figure 2.27). Furthermore, it has been proven that higher curing temperatures result in an increased rate of polymerisation and a higher degree of cure, as lower viscosities allow for greater polymer chain mobility and thus more interaction with unconverted material [100, 129, 140, 157, 158].

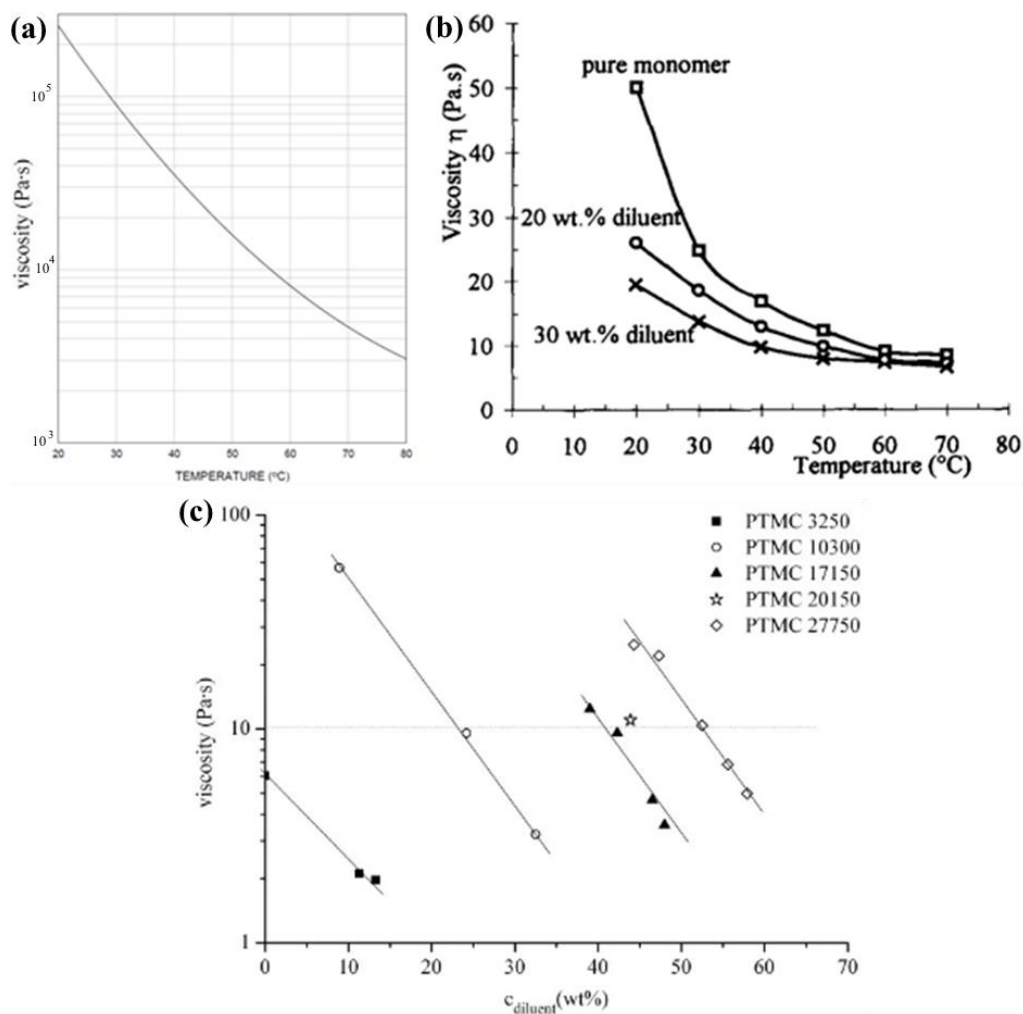


Figure 2.27 Effects of temperature and dilution upon resin viscosity for (a) an aliphatic urethane diacrylate resin (adapted from [118], © 2017 Allnex Group), (b) a dimethacrylate oligomer-based resin with alumina suspensions (adapted from [124], © 1998 Elsevier), and (c) resins with different oligomeric molecular weights (adapted from [116], © 2011 Wiley).

Curing temperature also affects material shrinkage, occurring as the phase changes from liquid to solid. Due to the molecular bonds altering and the units chaining together, the volume of the cured polymer is less than the volume of the constituent resin [127, 159]. Shrinkage is related to the number of reactive groups on the monomer, with tetra- and tri-acrylate monomers producing greater material shrinkage compared to di- or mono-unsaturated-acrylates [128]. Material shrinkage induces internal stresses, which can lead to warping or curling occurring, especially within flexible materials [119, 127, 128,

141, 159]. High shrinkage can reduce the dimensional accuracy during printing which is detrimental to parts requiring precise features such as gears or small internal voids [101, 127]. Annealing the printed part in an oven allows the polymer chains to relax and rearrange, reducing the internal stresses and improving the mechanical performance.

Glass transition temperature (T_g) is an important indicator of a polymer's performance at a given temperature. If the polymer is being used below its T_g there will be insufficient thermal energy to allow for polymer chain motions, and the polymer will be hard and glassy [113, 126, 134, 153]. On the other hand, when a polymer's temperature is above T_g , it displays an elastic behaviour. Elastomers that perform well at room temperature, exhibiting fast reversible behaviour and low hysteresis, normally have T_g in the range of (-70 to -20) °C [113]. The inclusion of compounds with hard chain segments, such as aromatic groups, can raise the transition temperature by several decades of magnitude [153, 160]. The glass transition temperature is strongly related to the final conversion percentage of the polymer undergoing UV curing, as the polymerisation may be inhibited by vitrification, where the mobility of the molecules is reduced as conversion increases [129, 156, 158].

2.3.5 Recent Improvements in DLP Printable Materials

An article by Patel *et al.* [82] began with the statement that commercially available elastomeric resins are still not sufficient for many applications, with the elongation at break of many SLA resins falling below 100%. They acquired commercial non-SLA resins of an epoxy aliphatic acrylate monomer (Ebecryl 113, Allnex) and an aliphatic urethane diacrylate oligomer (Ebecryl 8413, Allnex), which were mixed in ratios from 5:5 to 0:10, with 2 wt% TPO photoinitiator added. Samples were printed using a Free Form Plus 39 by Asiga, a DLP system which uses a 385 nm UV light source. Layers of 100 µm thickness were irradiated for 10 seconds each. As the Ebecryl 8413 resin has an extremely high viscosity (21 000 mPa.s to 44 000 mPa.s at 60 °C) [120], a custom heat bath was created, maintaining the resin at 70 °C during printing. The

printed structures were sonicated in isopropyl alcohol (IPA) for three minutes before being post-cured in a UV oven for three minutes. The results of their stress-strain and material properties tests are shown in Figure 2.28.

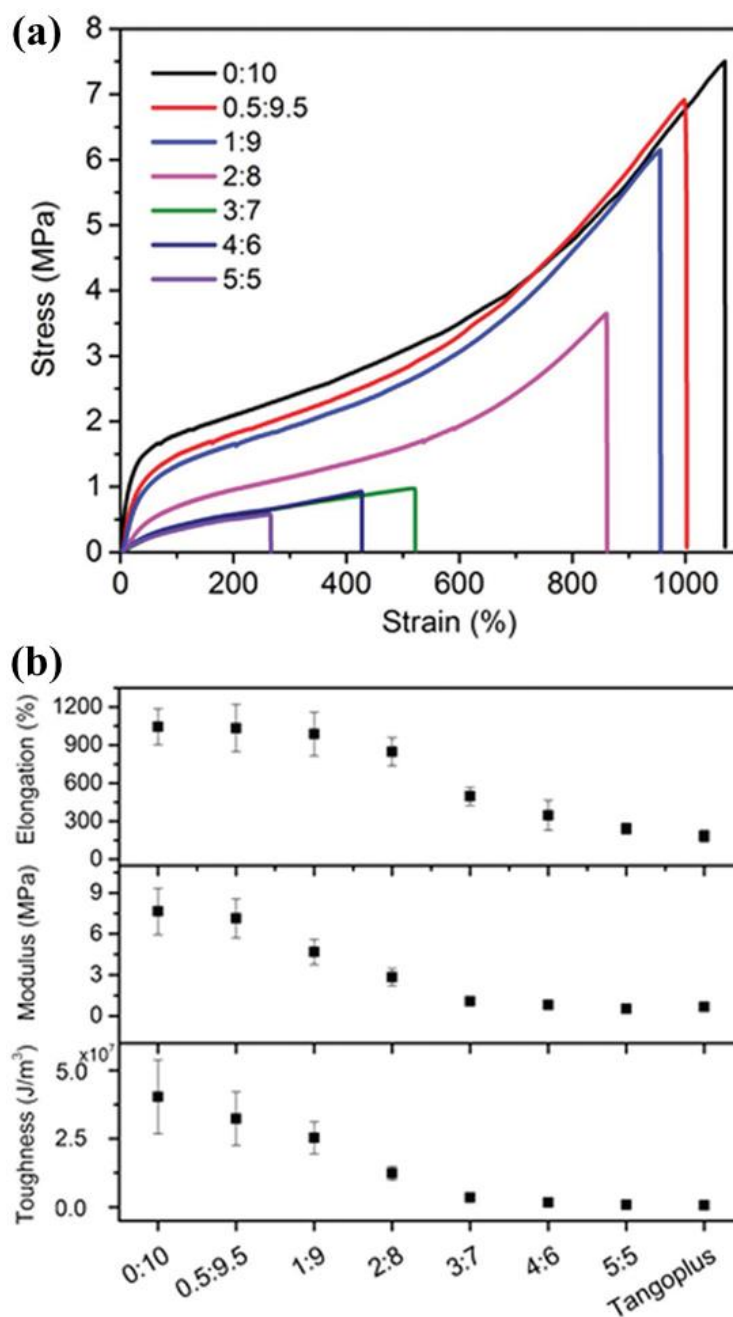


Figure 2.28 Mechanical properties of elastomer mixtures of Ebecryl 113 and Ebecryl 8413: (a) stress-strain curves and (b) mechanical properties box plots (adapted from [82], © 2017 Wiley).

Despite the online datasheet for Ebecryl 8413 [120] stating its elongation at break is 550%, Patel *et al.* claim their 0:10 mixture (pure Ebecryl 8413) produced elongations of over 1100% with no additives aside from the photoinitiator. Furthermore, none of the parts evaluated in their paper were created using their 0:10 mix. Rather, it was the least viscous 5:5 elastomer mixture ($\epsilon_{max} \approx 250\%$, $\sigma_{max} \approx 0.6$ MPa) which was used to create their displayed structures and actuators. The pure Ebecryl 8413 resin has an incredibly high viscosity, far exceeding the recommended threshold for printability even when taking into account a print temperature of 70 °C [82, 120]. The ability to realistically 3D print “highly stretchable” elastomeric parts using this resin is disputed, as although Patel *et al.* could synthesise this resin for “DLP printable elastomers that can be stretched by up to 1100%”, they could not, in fact, cure anything more complex than films with it.

The printing of UV curable Ebecryl 8413-based compounds was also explored by Kurang *et al.* [161], using direct ink writing (DIW) to produce elastomers. This type of 3D printer is a cross between FDM and SLA/DLP, in that a liquid material is extruded from a nozzle to draw lines but is cured using UV light rather than cooling and solidifying. This process avoids the difficulties of printing with highly viscous fluids by forcing it through the nozzle but results in a lower print quality [99]. Their resin formulation combined Ebecryl 8413 and the monomer n-butyl acrylate in a ratio of 1:1.5 wt/wt, after which an undisclosed amount of polycaprolactone was dissolved into the acrylates. To this mixture, 4 wt% of fumed silica powder and 1.5 wt% BAPO photoinitiator were added. During printing, the syringe was heated to a temperature of approximately 70 °C to melt the mixture and allow it to flow through a nozzle of 600 µm internal diameter. Printed dog bone tensile samples showed 500% to 600% elongations and tensile strengths between 4.5 MPa and 5.5 MPa, depending on the filament printing angle (see Figure 2.29).

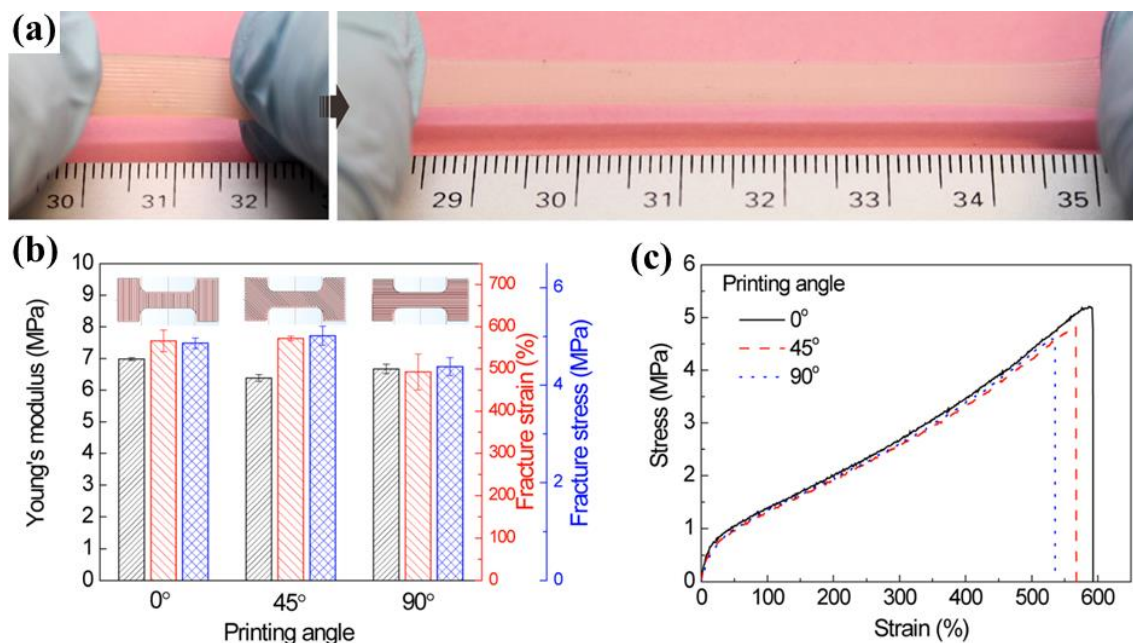


Figure 2.29 Direct ink writing material (a) stretched by hand, (b) mechanical properties at different printing angles, and (c) stress-strain behaviour at different printing angles (adapted from [161], © 2018 ACS).

Another recent success in the formulation of highly elastic SLA suitable resins involved the use of poly(trimethylene carbonate) (PTMC) oligomers [116]. They analysed the effect of PTMC oligomer molecular weight on mechanical properties such as tensile modulus, elongation at yield, and tear resistance. They found that all these properties increased with increasing molecular weights in stereolithographic printed films. However, with the exception of the lowest molecular weight oligomer, the PTMC oligomers occurred in solid states at room temperature. Heavy dilution was required to bring the viscosities down to a suitable level, even at elevated temperatures of 65 °C. These oligomers were mixed with varying amounts of the non-reactant diluent propylene carbonate, 5 wt% of the photoinitiator TPO-L, and an orange dye.

The resin formulation which exhibited the highest elongation at yield as a film, 160%, was unable to be used in the creation of the 3D structures [116]. The heavily diluted resin cured into a swollen polymer during the printing process, and the subsequent drying of the non-reactive diluent left the resultant

structure too brittle and fragile for use. The authors observed that following compression tests of solid cylinders of the other resin formulations, 65% to 75% of the structures returned to their original shapes within 30 minutes. This extreme delay demonstrates that these PTMC elastomers have high viscoelastic and hysteric properties. Therefore, these materials are intended for structural rather than functional applications.

DLP printable elastomeric compounds have been successfully created using only monomers and photoinitiators by Thrasher *et al.* [83]. They modified a DLP printer to improve printability by using a biphasic vat: creating a lower layer of brine and pouring their immiscible resin above. Four resin formulations were evaluated, comprised of various ratios of the monomers 2-hydroxyethyl acrylate, 2-(2-ethoxyethoxy)ethyl acrylate (EEEA), and poly(dimethylsiloxane) bis(propylacrylamide) (PDMSDMAA), along with the photoinitiator BAPO and dyes. The two resin formulations without the PDMSDMAA are of particular interest, the first comprised of the monomer HEA and 1% BAPO (designated as HydrOHflex). The other was a 60:40 ratio of EEEA:HEA, plus 1% BAPO (designated as ThrashOHflex). Dyes were used (up to 0.75%) to improve the printing resolution for the functional parts, however, the mechanical tests were performed on the undyed materials. By avoiding large viscous oligomer molecules, these resins achieved viscosities below 100 mPa.s at room temperature. These materials produced a high elongation with an elastic stress-strain response, with strains between 330% and 472% achieved (see Figure 2.30 and Table 2.3).

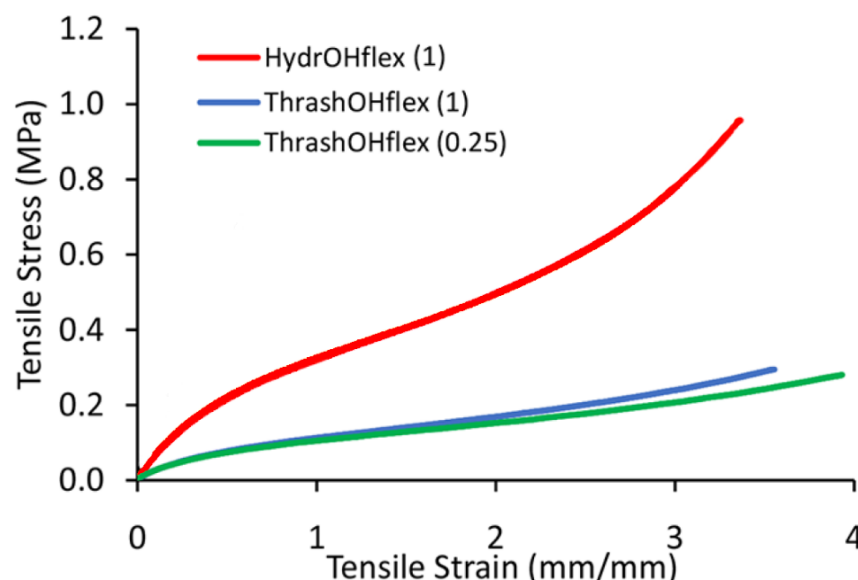


Figure 2.30 Stress-strain curves of HEA-based photopolymeric resins (adapted from [83], © 2017 ACS).

Table 2.3 Material properties of Thrasher *et al.* photopolymeric resins (adapted from [83], © 2017 ACS).

Material ^a	σ_{max} (MPa)	ϵ_{max} (%)	Shore A Hardness	T_g (°C)
ThrashOHflex (0.25)	0.42 ± 0.02	422 ± 22	13.7 ± 0.6	-29
ThrashOHflex (1)	0.24 ± 0.01	329 ± 7	15.0 ± 2.4	-30
HydrOHflex (1)	1.23 ± 0.31	348 ± 26	33.3 ± 0.6	12

^a: number in brackets is photoinitiator concentration (%), σ_{max} : maximum stress, ϵ_{max} : maximum strain, T_g : glass transition temperature

There is some discrepancy between the values reported in the main text of the article [83] and the ones shown in the supporting information. Particularly, the main text reports ThrashOHflex (0.25) to have an elongation at break of $(472 \pm 22)\%$, but the corresponding figure in the supplementary file for this result (Figure S11) shows $(443 \pm 41)\%$ instead. Additionally, the authors state the HydrOHflex material showed little hysteresis and no sign of creep or fatigue, but only tested up to five cycles. Furthermore, the HydrOHflex (1) material showed a high glass transition temperature, only transitioning at 12 °C.

2.4 Summary

Motors have proved effective in robotic applications requiring high speeds, stiffnesses, and accuracies, such as automated assembly lines and in other large machines. However, these same traits make them unsuitable in the developing field of human-robot interactions, where device compliance is necessary for safety and the manipulation of soft objects. Similarly, the low power-to-weight and power-to-volume performance of motors inhibit their application in small lightweight robotics. Other actuation technologies were investigated as potential alternatives which could provide the desired characteristics. Hydraulic actuators have high power-to-weight ratios but require a heavy system due to the fluid reservoir. Shape memory actuators have excellent work densities and are highly configurable but only produce small strains and have long cycle times. Ionic electroactive polymer actuators are lightweight and flexible but require a wet environment and are extremely slow. Dielectric elastomer actuators have extremely fast response times and high strains but require thousands of Volts of electricity to operate. Piezoelectric actuators have exceptionally fast actuation times but produce miniscule strains. Biological-synthetic actuators show good promise for incorporating biological muscle into robotic devices, but the technology presently cannot produce actuators larger than the insects the muscles are harvested from and have a very short lifetime.

Pneumatic technologies show the best potential for lightweight and compliant devices, having good power-to-weight ratios and fast response times. Their main drawback is the difficulty of precise control, which is linked to its innate compliance. The two most common pneumatic actuators – pneumatic cylinders and pneumatic artificial muscles – are both linear-acting and made using metallic components. By utilising soft materials instead, even lighter and more compliant devices can be constructed. The fabrication of soft pneumatic actuators from elastomeric materials allows unique bending, twisting, or linear motions to be produced when pressurised. Bending motions in pneumatic actuators are easily achieved through anisotropic stiffnesses or the asymmetric

arrangement of chambers, but linear-acting soft devices of high fidelity are comparatively rare.

The creation of new soft pneumatic actuators is presently limited by the fabrication methods and materials available. Moulding techniques have a greater range of materials to choose from with better mechanical properties but are limited to simple geometric shapes and multi-part joining. By contrast, 3D printing methods can create complex and detailed components of monolithic structure but have fewer materials available with poorer properties. The digital light projection method of stereolithography can produce intricate components at high resolutions from photopolymeric resins. Importantly, the synthesis of a new resin is a relatively simple process, requiring the mixing of a few chemicals. However, there is an extremely broad variety of base chemicals to choose from, and the formulation of an elastomeric resin which can be 3D printed is convoluted and iterative in nature. There are many factors which interdependently affect both the formulation and the curing processes. While there have been some successes reported in the literature, there is still a need for advancements in DLP 3D printable elastomeric resins for the creation of soft pneumatic actuators, which is one of the aims of this study.

Moreover, it is necessary that this printable material be manufactured as more than just thin films and regular geometric shapes; it must be able to fabricate complex structures with internal voids. The material must be stiff enough for the parts to support their own weight without deformation, yet soft enough to exhibit a significant and usable strain when placed under pressure. Linear acting soft pneumatic devices have been far less studied and developed in comparison to those which generate bending motions, hence this thesis aims to expand this area of literature. To better understand and contrast the linear acting soft actuators, their performance will be comprehensively analysed and small robotic devices are constructed and evaluated against similar soft robotics in literature.

3 MATERIALS AND METHODS

3.1 Resin Materials, Synthesis, and Evaluation

Raw Materials

All reagents, including BR-345 (Dymax), EBECRYL 8411 (Allnex), EBECRYL 8413 (Allnex), Vivid Cure 70201 (Resin Designs), Vivid Cure 70501 (Resin Designs), UV Cure 60-7111 (Epoxies), isobornyl acrylate (IBOA) (technical grade, Sigma-Aldrich), 2-hydroxyethyl acrylate (HEA) (96%, Sigma-Aldrich), diphenyl(2,4,6-trimethylbenzoyl)phosphine oxide (TPO) (97%, Sigma-Aldrich), carbon black pigment (MakerJuice Labs), magenta pigment (Monocure3D), and tetrahydrofuran (THF) (99.9%, Sigma-Aldrich) were used as received. Rationale for the selection of these materials is discussed in section 4.2.2.

Resin Synthesis

The synthesis of resins was carried out in a round-bottomed flask, using a magnetic bar for agitation. This equipment, along with the oligomers, were preheated to 60 °C in an oven to improve the flow before mixing. A temperature-controlled oil bath was also preheated to 60 °C.

All measurements were taken on a HR-200 (A&D) electronic scale (resolution of ± 0.1 mg), zeroed between each step. First, the photoinitiator was weighed and added to the flask, then the monomers were measured and poured in. Next, the preheated oligomers were measured and poured into the flask. To ensure the precise measurement of the liquids, syringes were used to transfer the final few grams dropwise.

A stopper with two gas pipes was inserted into the neck of the flask, through which a constant stream of nitrogen gas flowed for the duration of the experiment (flow rate of 2 L.min⁻¹). The flask was then immersed in the heated oil bath and the magnetic stirrer (MS-H280-Pro, SCILOGEX) was set to a rate of 200 min⁻¹ (Figure 3.1 (a)). The process ran for approximately six hours to ensure homogenisation. Afterwards, the resin was transferred to an opaque container,

and the pigment was added. The resin was re-homogenised by vigorous shaking and then placed in a 60 °C oven for storage.

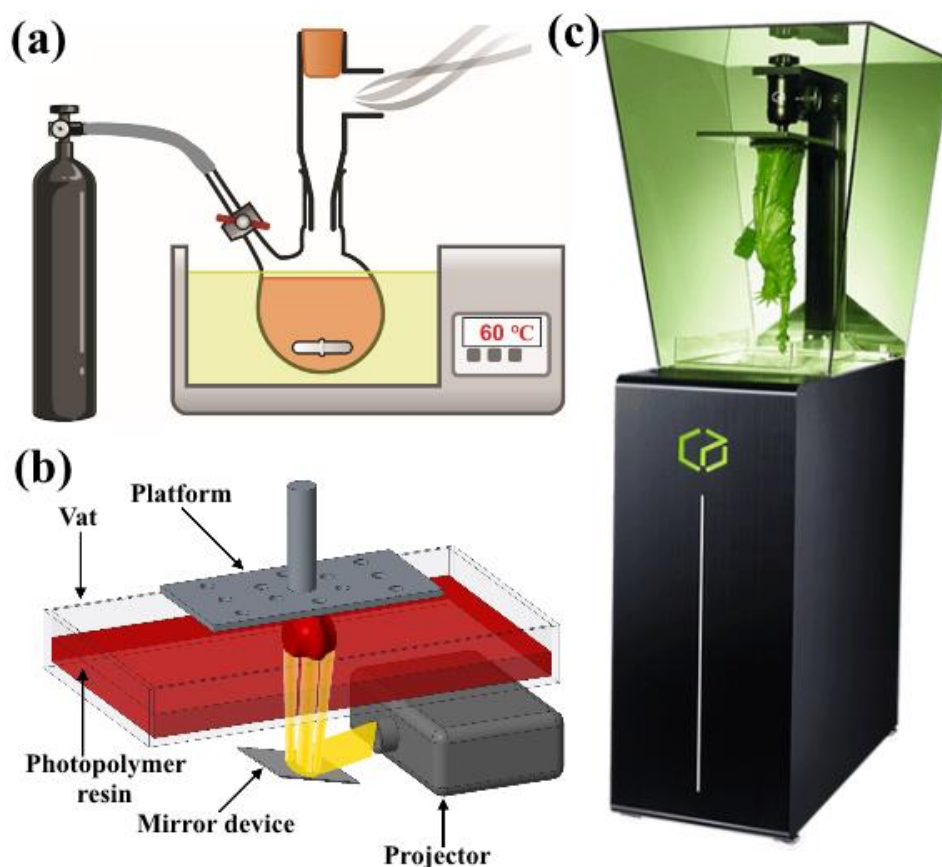


Figure 3.1 (a) Schematic of the resin synthesis process, (b) schematic of the DLP 3D printing process, and (c) Titan 2 HR DLP printer (adapted from kudo3d.com).

Resin Characterisation

A Physica VT 2 MCR 301 (Anton Paar) was used to measure resin viscosity. A PP25/E/TI probe was selected, with 0.6 mm of distance set between the plates. Each test run recorded 100 data points over 200 seconds, with the shear rate starting at 1 s⁻¹ and finishing at 1000 s⁻¹. Measurements were recorded at temperatures of 25, 30, 40, 50, and 60 °C. Recording was started when the temperature stabilised within ± 1 °C of the set point and was repeated three times to ensure reliability. Viscosity data is reported at a shear rate of

100 s⁻¹, as that is the possible highest shear rate experienced during the DLP printing process [122].

The molecular weight of the resin was acquired using a Shimadzu UFLC system equipped with a RID-10A and a Sedere ELSD photodetector. The resin was dissolved in THF (10 mg.mL⁻¹) and injected at a rate of 1 mL.min⁻¹ on a Phenomenex Phenogel column (00k-0644-k0). All experiments were performed at room temperature.

3.2 3D Printing of Resins

3D Printer

The DLP 3D printer used throughout this work was a Titan 2 HR (Kudo3D Inc.) (Figure 3.1 (b) and (c)). It was chosen primarily due to its high spatial accuracies, with its light source capable of producing XY resolutions between 23 μm and 37.5 μm per pixel. The light source projects a grid of lights measuring 1920 pixels by 1080 pixels, equivalent to a build area of 44.16 mm by 24.84 mm at a resolution of 23 μm per pixel, or 72 mm by 40.5 mm at a resolution of 37.5 μm per pixel. The maximum build height, measured as the height the platform can travel up the linear stage, is approximately 250 mm, while the allowable Z resolution can be between 5 μm and 100 μm. The projector was scaled to provide an XY resolution of 37.5 μm and a Z-axis step size of 50 μm as a good compromise between print speed, size, and resolution.

The light projector within this DLP printer is an EH331 (Optoma) that displays Full HD at 1080p. The lamp is rated at 195 W of power and has a projection uniformity of 70%. This provides a power density of approximately 7000 mW.cm⁻² at the XY resolution of 37.5 μm per pixel, without accounting for the optical filter or deterioration over time.

The resin material is held within an open-topped vat throughout the printing process. Along the bottom of the vat is a soft transparent silicone, sandwiched between a transparent acrylic lower layer and a clear polytetrafluoroethylene (PTFE) film on top. The soft silicone and low-stick film help to reduce the separation forces experienced between the freshly cured

layers and the vat, in addition to providing an excellent surface smoothness. Only one edge of the vat body is clamped down, allowing the body to bend upwards during the peeling process, further improving printability. These bottom-up DLP printers have the curing occur beneath the resin surface away from the atmosphere, minimising the occurrence of oxygen inhibition and allowing longer-chain polymers to be produced [128, 157].

Printer Modifications

This DLP printer was modified to improve its performance and printability. Three upgrades to the printer were made: the addition of a vat heating system, the creation of a new build platform, and the replacement of the projector filter. The light transmission measurements of the projector filters were recorded using a Red Tide USB650 (Ocean Optics) spectrometer with an integration time of 3 ms.

Model Creation

The 3D models for printing were created using the computer-aided design program Creo Parametric (version 3.0, PTC). Where necessary, support structures were manually added to the models in this program. These CAD models were imported, oriented, and sliced into layers according to appropriate settings into a 3D printable format using Creation Workshop (version 1.0.0.75, Envision Labs). The output of this process, a collection of black and white image files, were encoded in a .zip file and transferred to the Titan printer.

Printer Settings

The printer software was operated via a webpage after a wireless connection had been established. This webpage provided control over the projector, linear stage, and most importantly, the parameters affecting the printing operations. These parameters include the global layer height, resolution and build size, and shutter toggling. For each individual layer or group of layers, the exposure time in seconds, lift height, lift speed, lower

speed, and delay time between layers was specified. When the printing process was initiated, the layers were projected sequentially, with the platform raising between each layer, until the part had been completely formed.

The adhesive forces between a newly cured material and the vat surface are greater when curing a layer with a large surface area or if using a higher viscosity resin. A slow, gradual peel was used to minimise these forces and reduce the risk of damaging both the print and the vat. The lift speed for each layer was proportional to the area of the cured material for that layer.

The soft elastic nature of the materials being produced requires additional conservative measures compared to stiffer polymers. It should also be noted that as the polymers are flexible, there can be some observable geometric misalignments between layers, especially on tall, thin features such as supports. Thus, to achieve a part with minimal distortions and damage during printing, the platform speeds were lowered significantly, and a delay between layers was implemented to allow time for the displaced structures to return to their desired locations.

Printing the Resins

Due to the tendency of pigments to settle at the bottom of the resin bottle over time, the pigmented resins were vigorously shaken to re-homogenise the pigment prior to use. This would cause small air bubbles to form within the viscous resin, which were removed by placing the open container within a heated vacuum chamber for an hour. The resin was then poured into the vat and the heat bath switched on. Printing began once the temperature had stabilised at 60 °C.

To produce the specimens for mechanical testing, rectangular blanks were printed directly onto the flat surface of the platform with an exposure time of six seconds for the first layer and four seconds for every subsequent layer. Prints requiring more complex geometries were produced using support structures and higher initial exposure times to ensure adequate cohesion. Immediately after printing, the build platform and attached polymeric

structures were placed within a 60 °C oven overnight, which light annealed the polymer chains and reduced the internal stresses. Afterwards, the parts were detached from the print platform and any support structures were trimmed. The exterior surfaces and any interior chambers were repeatedly flushed with isopropyl alcohol and wiped with a microfiber cloth or cotton swab to clean off remaining residue. Finally, the parts were subjected to post-curing by being placed inside a UV oven (Form Cure, Formlabs) for 30 minutes, while submerged in a water filled beaker to prevent oxygen inhibition, rotated once when halfway through. After being post-processed, the blanks were cut into dog bone shaped specimens using a die press.

3.3 Cured Polymer Characterisation

Scanning Electron Microscopy

Samples were analysed using scanning electron microscope (JSM-6490LV, JEOL) with an accelerating voltage of 15 kV. Imaging was enhanced by coating the surfaces with a thin layer of gold (~20 nm) using a sputter coater (Smart Coater, JEOL). The cross-sectional view of a mechanical testing specimen was taken after the sample had been immersed in liquid nitrogen for 20 minutes and cleanly fractured.

Printed Sample Characterisation

The tensile, hysteresis, and relaxation experiments were performed using an EZ-LX (Shimadzu) universal mechanical tester. The data was recorded using a 500 N load cell connected to Trapezium-X software (Shimadzu). Sample dimensions were measured using a digital calliper (RS Pro) with a resolution of ± 0.01 mm before placing the sample into the clamping mechanisms. For the tensile and the cyclic tests, a strain rate of 2 mm.min⁻¹ was applied and with a sampling period of 200 ms. In theory, stress relaxation experiments are performed with an instantaneous strain application, but as this is not physically possible, the strain was applied in an S-curve shape at the maximum velocity of the EZ-LX, sampled for 300 seconds with a period of 10 ms [162]. As the

materials were elastic and deformable, heavy clamping was required to secure the specimens in place. This compression pre-stressed the system but was adjusted manually prior to recording.

The dynamic mechanical analysis experiments were performed on a DMA 242 (NETZSCH) machine. The material strain was set to 5% at a cycle frequency of 1 Hz, performed across a temperature range of (-130 to 150) °C, and a scan rate of 2 °C.min⁻¹, under a nitrogen atmosphere.

Sample Density and Swelling Characterisation

The mass density of the solid polymer (ρ_s) was determined using a pycnometer and distilled water [127, 163]. The environmental temperature remained 20 °C throughout the experiments. Mass measurements were taken for the following conditions: dry empty pycnometer, pycnometer partially filled with polymer m_s , pycnometer filled with polymer and distilled water $m_s + m_{H2O}$, and pycnometer filled with only distilled water m'_{H2O} . Using the density of water ρ_{H2O} at the environmental temperature (998.2 kg.m⁻³ at 20 °C), the density was calculated by:

$$\rho_s = \frac{m_s \times \rho_{H2O}}{m_{H2O} - m'_{H2O}} \quad (3.1)$$

The chemical method of estimating cross-linking density involves immersing an elastomer in a solvent and observing the swelling behaviour. Prior to the swelling tests, samples were left submerged in the solvent tetrahydrofuran for several days to remove any uncured monomer or loose particles, followed by drying the samples at room temperature. After a suitable drying period, the dry mass of the polymer m_d was recorded. The experiment involved submerging the cleaned elastomeric samples in fresh THF and periodic weighing, which was repeated until no further increase in mass was recorded. To improve the mass measurement accuracy, samples were dabbed with paper towels to remove excess solvent before weighing on scales, performed quickly to minimise the evaporation of solvent from the swollen

polymer. The final mass of the swollen network at equilibrium was recorded as m_{eq} . The swelling degree can be defined as:

$$\text{Swelling degree (\%)} = \frac{m_{eq} - m_d}{m_d} \times 100 \quad (3.2)$$

3.4 Actuator Evaluation

Experimental Design

The testing environment which facilitated the characterisation experiments was MATLAB Simulink (r2018b, MathWorks Inc.) via a PCI-6221 (National Instruments) data acquisition device, through which data was recorded and processed. Two pressure regulator devices were used to control the flow of air through the actuators, one for vacuum pressure (ITV0090-3BL, SMC) and another for positive pressure (VPPM-6L-L-1, Festo). Both regulators provided internal pressure feedback via analogue output voltages. In experiments where both positive and negative pressures were delivered to the actuators, a solenoid valve (VUVS-L20-P53U, Festo) was used to switch the pneumatic connections. Pressure vessels were used for each regulator, providing improved response times and less transient effects when compared to directly connected motor-pumps. The positive pressure regulator was supplied with a constant 3 MPa of air pressure from a wall outlet, while the negative pressure vessel was constantly evacuated by a 1410-304-VD (Gardner Denver) diaphragm motor-pump. Additional loss factors include the lengths of pneumatic tubing, valve losses, and energy absorbed through material deformation.

The laser displacement sensor (optoNCDT 1420, Micro-Epsilon) utilised had an analogue output with a theoretical step size of approximately 0.15 mm per step. This may be observed on the data curves after noise filtering has taken place, however it was considered negligible and acceptable. Pieces of white paper were attached to the free surface of the actuators to improve signal strength.

The force sensors used for the expansion and contraction force measurements were the FX29 (TE Connectivity) and the FG-5005 (Lutron), respectively. The ends of the unpressurised actuators were constrained such that the force was passed through a force gauge at one end while the other was fixed. For the expansive force tests, a conical frustum was placed between the unrestrained surface of the actuator and the restrained load cell. To perform the measurement of contraction forces, a hook was bonded to the free surface of the actuator, which was then linked to a hook on the end of the load cell. A screw lift was used to remove the slack from the system before measuring.

Electromechanical Behaviour

A MFIA device (Zurich Instruments) was used to measure the intrinsic capacitance of the actuators across a range of pressures. A silver mesh with an adhesive backing was attached to either end of the soft actuators, which the capacitance device was then connected to. The oscillation frequency was set to 300 kHz, the sampling rate was 1 000 Hz for the step and ramp experiments and 100 Hz for the stability experiments. The on-board noise filtering used was a maximum bandwidth of 20 Hz and a suppression of 20 dB.

4 DEVELOPMENT OF AN ELASTOMERIC RESIN FOR DIGITAL LIGHT PROCESSING PRINTING

4.1 Introduction

This chapter reports on the steps taken towards the formulation and characterisation of a new DLP printable elastomeric resin. The modifications made to the 3D printer to improve the printability of materials are highlighted. The actions taken to formulate, evaluate, and iterate upon the preliminary design of new resins are examined, with justifications provided for the advancement or removal of various chemicals.

The final formulation selected for full characterisation, designated ElastAMBER, was prepared from a di-functional polyether urethane acrylate oligomer, a blend of two different diluent monomers, a photoinitiator, and a pigment. This elastomeric resin had a low viscosity at moderately raised temperatures, allowing for easy printing at near room temperatures. The cured elastomer exhibited a good elastic response, low hysteresis, and negligible viscoelastic relaxation.

4.2 Preliminary Resin Formulation Experiments

4.2.1 Printer Modifications

A heat bath mechanism was constructed to maintain the resin at an elevated temperature from Peltier elements, a temperature probe, relay switches, and a microcontroller (Figure 4.1 (a)). This system was controlled with a custom feedback loop, which accounted for system lag, warming the resin to the set temperature with minimal temperature overshoot. A smaller perforated build platform was manufactured to match the size of the printable area, reducing the area of displaced resin, thus lowering the forces during printing (Figure 4.1 (a)). The original optical filter in the projector was removed and replaced by a Newport 20CGA-360. This filter had a cut-on frequency of (360 ± 5) nm, lower than that of the original (~ 400 nm, Figure 4.1 (b)) allowing the

transmission of some UV-A light, which the TPO photoinitiator is the most reactive to.

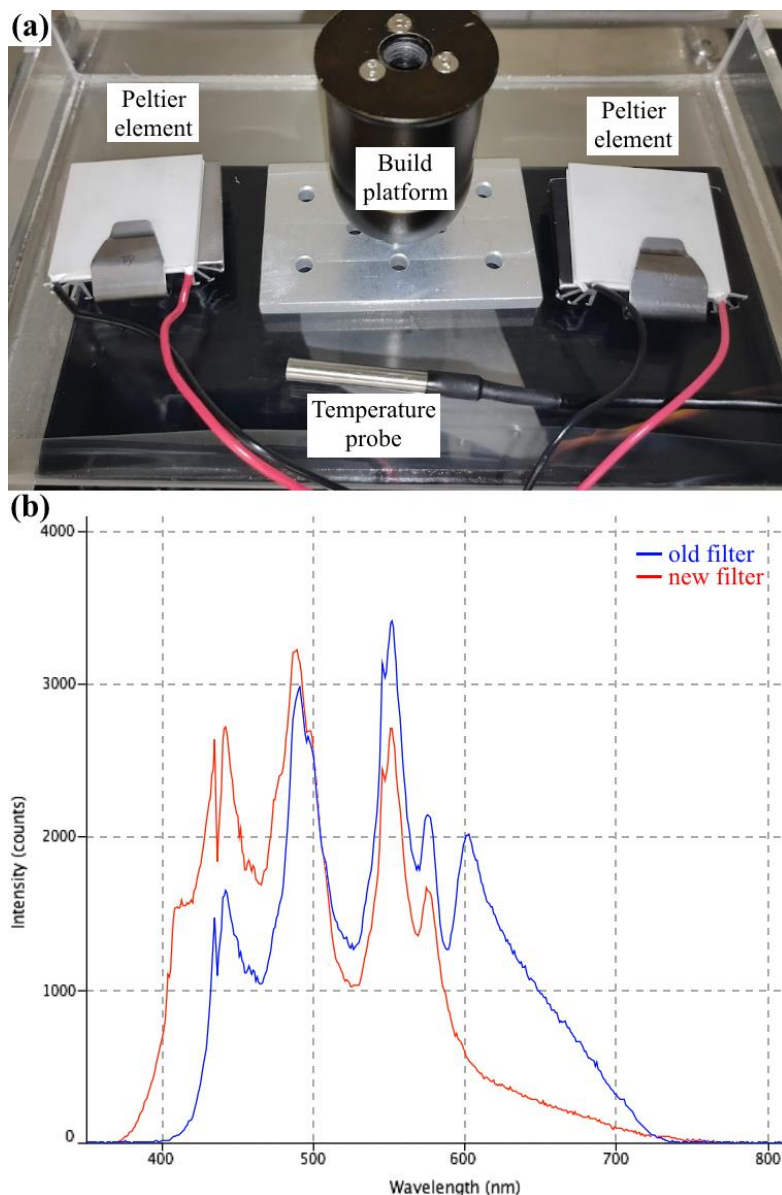


Figure 4.1 Titan printer modifications (a) heating system elements and build platform, and (b) transmission properties of the old and new projector filters.

4.2.2 Resin Formulation and Initial Evaluation

Several potentially suitable base materials were acquired from various sources to iteratively synthesise and evaluate new resin blends towards the creation of 3D printable elastomers (Table 4.1). Most of the oligomeric resins were not intended for 3D printing applications, but rather intended for

applications such as protective surface coatings and to be cured by traditional methods.

Table 4.1 Sourced chemical types from various manufacturers.

Type	Manufacturer	Product Name
Oligomers	Dymax	BR-345
	Allnex	EBECRYL 8411
		EBECRYL 8413
	Resin Designs	Vivid Cure 70201
		Vivid Cure 70501
Monomers	Epoxies	UV Cure 60-7111
	Sigma-Aldrich	Isobornyl Acrylate (IBOA)
		1,6-Hexanediol Diacrylate (HDDA)
		2-Hydroxyethyl acrylate (HEA)
Photoinitiators	Sigma-Aldrich	Diphenyl(2,4,6-trimethylbenzoyl) phosphine oxide (TPO)
Pigments	MakerJuice Labs	EZ-Pigment Black
	Monocure3D	Magenta Pigment

The oligomers were selected based on their reported elongation at break, requiring a minimum of 200% to be considered (Table 4.2). Resin viscosity was also a consideration, but some manufacturers reported the viscosity at elevated temperatures rather than room temperature, preventing direct comparisons. As these resin blends were proprietary, the manufacturers did not publish the complete chemical compositions, often specifying only the generic classes of chemicals included and broad concentration ranges. Some of the products already had photoinitiators included, intended to be used off-the-shelf for certain applications and cured using specific tools.

Table 4.2 Reported properties of various commercial resin compounds.

Product Name	ε_{max} (%)	E (MPa)	η (mPa.s)	Diluent Included?	Photoinitiator Included?
	N/A	N/A			
BR-345	pure. 400 with 50% IBOA	pure. 4.6 with 50% IBOA	42 000 at 25 °C	No	No
Ebecryl 8411	320	8.8	3 400 – 9 500 at 65 °C	IBOA, 20%	No
Ebecryl 8413	550	9.0	21 000 – 44 000 at 60 °C	IBOA, 33%	No
VividCure 70201	300	N/A	13 000 – 24 000 at 25 °C	2-[[[(butyl- amino) carbonyl] oxy]ethyl acrylate, 25 – 50%	1-hydroxy- cyclohexyl phenyl ketone
VividCure 70501	200	N/A	2 000 – 3 500 at 25 °C	Isodecyl acrylate, 10 – 25%	1-hydroxy- cyclohexyl phenyl ketone
UV-Cure 60-7111	230	N/A	3 500 at 25 °C	Multiple, 30 – 70%	1-hydroxy- cyclohexyl phenyl ketone

ε_{max} : elongation at break, E : Young's modulus, η : dynamic viscosity

Several dozen combinations and ratios of the obtained chemicals were synthesised and evaluated for their potential for elastomeric material fabrication. Across the many tests, trends could be deduced regarding the effects of each constituent chemical and concentration on factors such as resin

viscosity, elastomer material properties, and warping of the cured polymer. Dozens of trials investigating the numerous combinations and concentrations of the oligomers, monomers, photoinitiators, and pigments were performed. As the results are not easily displayed in table format they will be discussed throughout the following section.

The first phase of resin evaluation involved the synthesis of 20 mL of resin per formulation. All resin blends, regardless of prior photoinitiator content, had 4 wt% of TPO added to ensure polymerisation in the DLP printer. The 1-hydroxy-cyclohexyl phenyl ketone photoinitiator included in the VividCure and UV-Cure products is only reactive to wavelengths below 300 nm [128]. Each resin blend, unpigmented at this stage, was applied to the surface of the printer vat before lowering the platform. The sample was then irradiated for 20 seconds with a large rectangular pattern. This single layer was then detached from the surface of the platform and post-processed. The polymer films were observed and handled to determine whether to continue experimentation with the formula in a larger batch, iterate upon the formulation then print another film sample, or discontinue with the current formula or a constituent chemical. The main selection criterion was the flexibility of the film sample, that is, how it behaved when deformed by hand. The successful samples were soft and deformed with ease, while the film formulations which fractured, tore, or were too tough were not passed to the next phase.

Next the resin viscosity was evaluated. Even if a cured polymer was soft and flexible, it would not pass to the next phase if the resin was too viscous to be used in DLP printing. Formulas were deemed too difficult to print if their viscosity was significantly above 1 000 mPa.s at elevated temperatures. These were re-evaluated with a higher proportion of diluent monomer, until they cleared the threshold, or their mechanical properties diminished too much. After several iterations of formulations, some chemicals were removed from consideration. The Allnex Ebecryl 8413 oligomeric resin was rejected due to its extremely viscous nature. When combined with IBOA in a 2:1 ratio, its viscosity exceeded 25 000 mPa.s at room temperature and 5 000 mPa.s at 60 °C. When

further diluted with IBOA in a 1:1 ratio to reduce the viscosity, the resulting polymer was stiff and brittle, characteristic of isobornyl acrylate homopolymers with glass transition temperatures near 90 °C [164].

The VividCure oligomeric resins and the UV Cure 60-7111 resin formulations showed good flexibility and responsiveness but tore too easily. This is likely due to them being formulated specifically for substrate coatings rather than standalone structures. While the HDDA monomer showed greater viscosity reductions than the other diluent monomers, it had a detrimental effect on material elasticity and toughness. Polymer formulations cured with HDDA were flexible at low strains but fractured under moderate deformations. The Dymax BR-345 and Allnex EBECRYL 8411 formulations both produced polymers with good flexibility, elasticity, and tear resistance. The inclusion of diluent monomers IBOA and HEA showed good viscosity reductions at moderate concentrations and produced reasonably high strain polymers.

Pigment type and concentration were assessed to gauge the minimum concentration required for dimensional accuracy. To measure the degree of through-curing and side-curing during printing, small test pieces consisting of multiple geometric features were created (Figure 4.2). An arch was used to observe the amount of through-cure in the Z-direction which occurred during printing, as well as giving an indication of maximum bridge spans and overhang angles. Column features showed the amount of side-curing in the XY-plane and served as a depiction of the minimum printable diameter. A wedge-shaped section provided an indication of the minimum distance between features. The cone could be used to gauge how much of the side-curing is proportional to the area of the projected light.

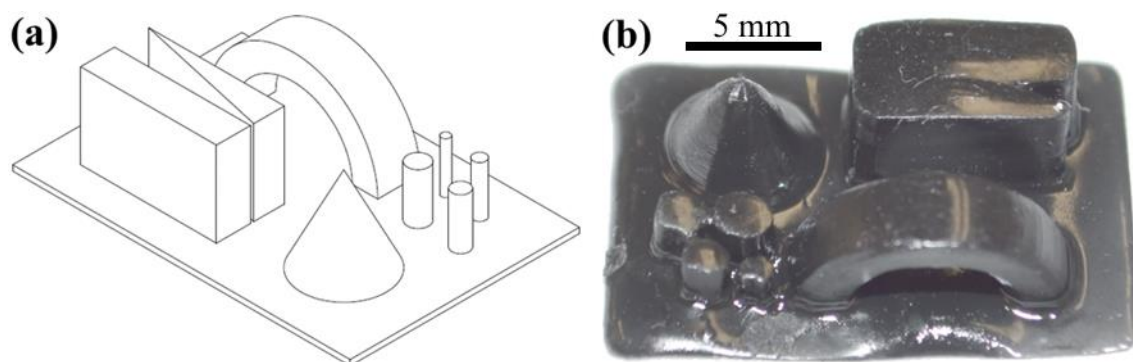


Figure 4.2 Geometric test piece (a) model and (b) printed part at 0.25 wt% carbon black pigment.

Further formula iterations on the remaining resin compounds were created to determine the layer exposure time for each level of pigment concentration which would provide the best degree of conversion without over-curing the material. Where the features had not fully formed, the exposure time was increased. If unacceptable over-cure occurred, the pigmentation was increased or exposure duration was lowered. It was determined that the carbon black pigment provided the best geometric accuracy, with a pigment concentration of 0.5 wt% best used at exposures of three to four seconds of exposure per layer in functional parts. Concentrations of 0.75 wt% and 1.0 wt% were found to have similar geometric accuracies but required longer exposure times. Lower concentrations of carbon black pigment did not sufficiently prevent the unwanted dispersion of light. The magenta pigment did not possess a high enough absorptivity coefficient for the purposes of this work, with the arches of test pieces through-curing completely in formulations containing 1 wt%, even at short exposure times.

4.2.3 Initial Mechanical Evaluation

Elastomers are a special class of polymers which can exhibit large strains when loaded and recover swiftly with when the load is removed [135]. Elastomers typically have a characteristic flattened 'S'-shaped curve on a stress-strain diagram and no well-defined yield point [104, 165]. By contrast, tough

and hard plastics are stiffer with a well-defined yield point, beyond which they plastically deform. This property was used to assess the nature of each polymer.

Tensile stresses and strains were recorded on the most promising formulations to determine the elongation at break, elastic modulus, and ultimate tensile strength. Due to the high elongation strains and Poisson's Effect, the samples would often partially or wholly slip from the jaws of the mechanical testing machine. These occurrences are indicated in the sample legends in the below figures.

Cyclic tests were performed to assess the dynamic characteristics of each material. The effects of TPO concentration on tensile performance was also evaluated. Based on the viscosity testing, it was decided to use the BR-345 oligomer in a 1:1 ratio with the diluent monomers. Similarly, the EBECRYL 8411 oligomer was best used in a 2.7:1 ratio with its diluent monomer.

The EBECRYL 8411 and IBOA (2.7:1, TPO 4%, CB 1%) formulation (Figure 4.3 (a)) was shown to have an ultimate tensile strength (σ_{UTS}) of 4.46 MPa and elongation at break of 210%. The BR-345 and IBOA (1:1, TPO 4%, CB 1%) blend (Figure 4.3 (b)) showed a more compliant response (σ_{UTS} = 1.65 MPa) at a similar elongation at break. For this reason and the significantly higher viscosity, the EBECRYL 8411 line was discontinued in favour of the softer BR-345 oligomer. Lower TPO concentrations (Figure 4.3 (c) and (d)) showed to increase the elongation at break, with 2% providing the best elongation for the selected exposure time and pigmentation. As evidenced by the well-defined yield points on these graphs, the BR-345 and IBOA blend polymers functioned more like tough polymers than elastomers.

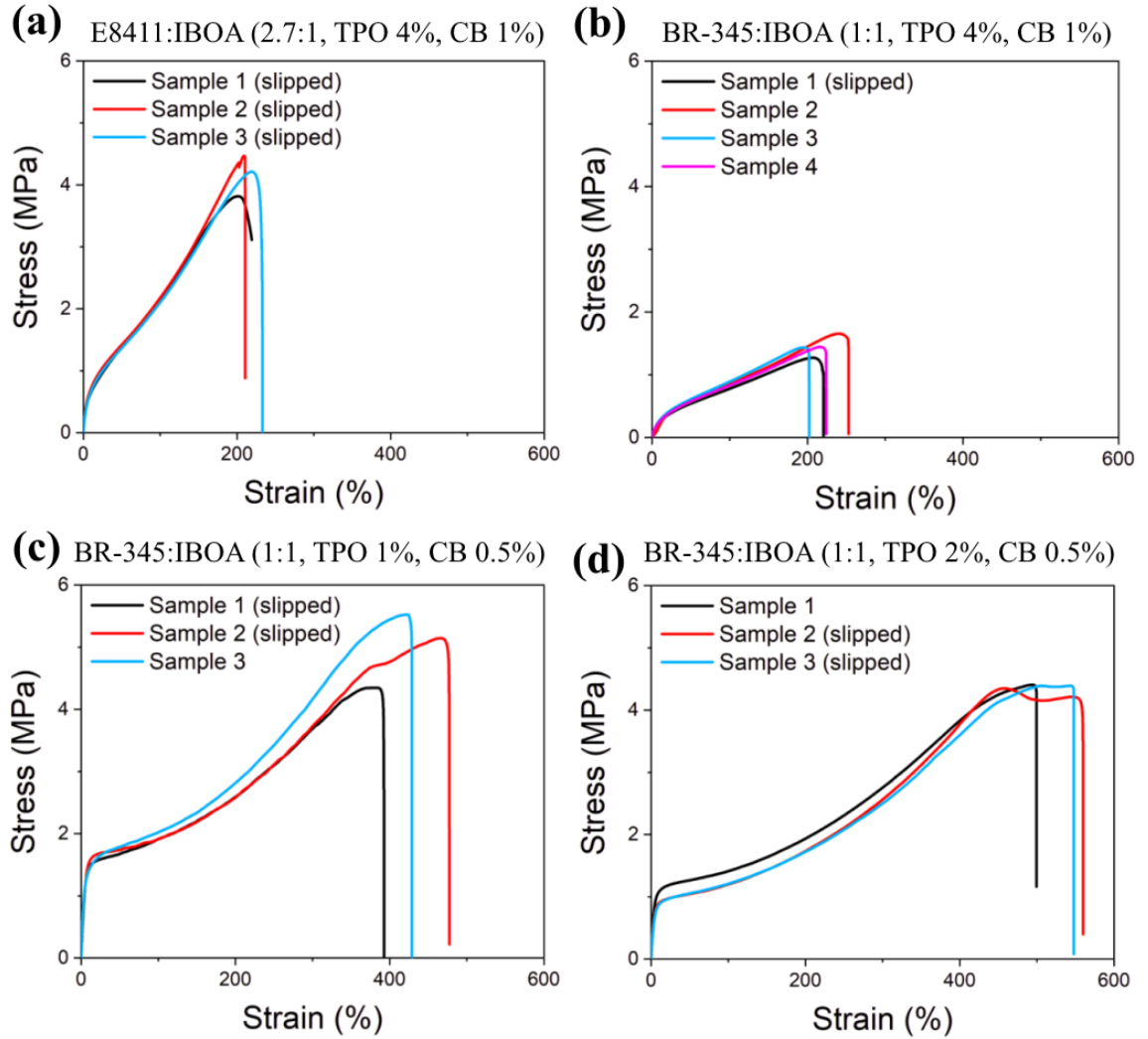


Figure 4.3 Stress-strain curves for (a) EBECRYL 8411 and IBOA (2.7:1, TPO 4%, CB 1%), (b) BR-345 and IBOA (1:1, TPO 4%, CB 1%), (c) BR-345 and IBOA (1:1, TPO 1%, CB 0.5%), and (d) BR-345 and IBOA (1:1, TPO 2%, CB 0.5%).

The combination of BR-345 and HEA resulted in a softer and more elastomeric material, but at a cost of some elongation at break (Figure 4.4 (a)). The lack of a definitive yield point and a very small hysteresis loop (Figure 4.4 (b)) indicates that the BR-345 and HEA formulation produces a very responsive elastomer. Contrasting this to Figure 4.4 (c), the combination of BR-345 and IBOA create a highly viscoelastic material. This can be observed through the large area of the hysteresis loop, indicative of a large mechanical energy loss through the cycle.

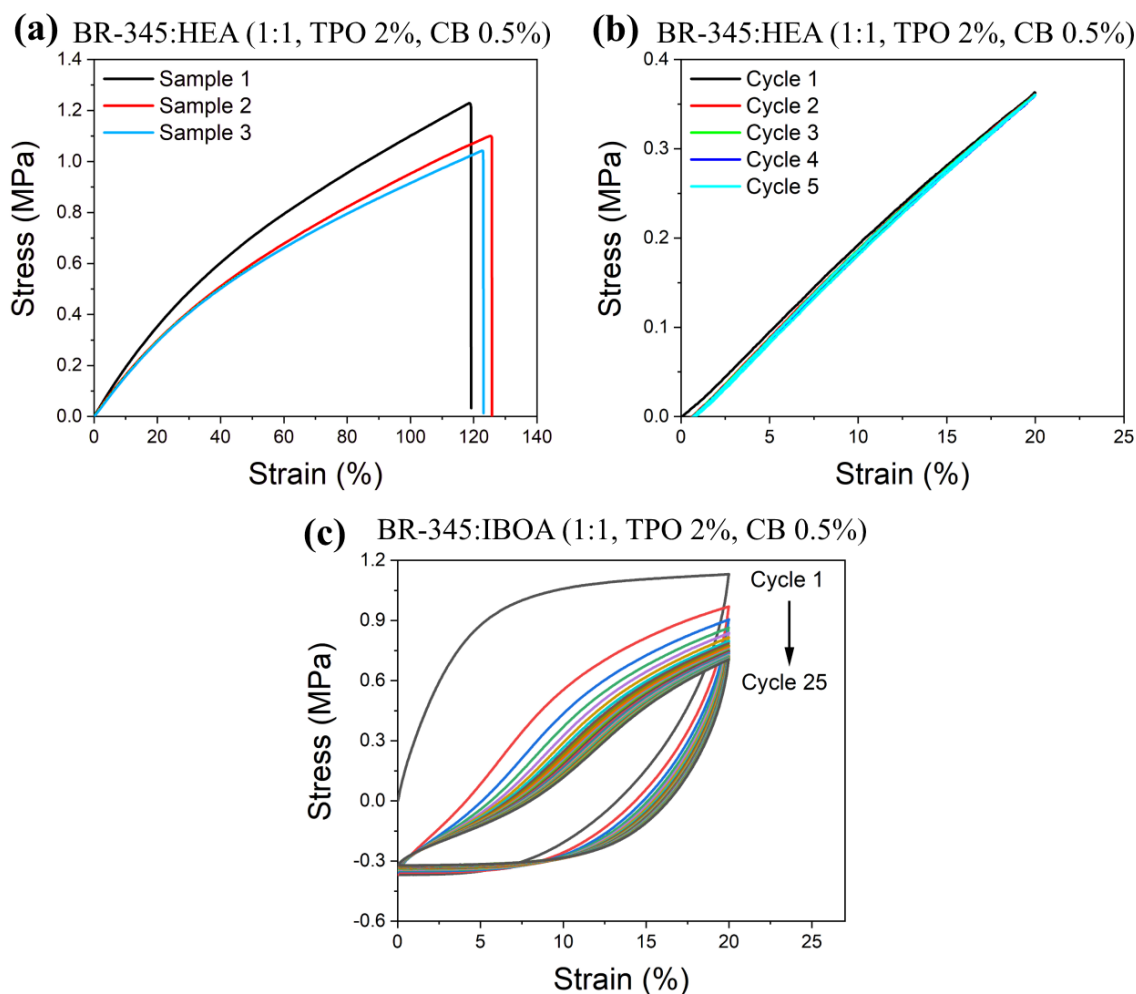


Figure 4.4 (a) BR-345 and HEA (1:1, TPO 2%, CB 0.5%) stress-strain curves, (b) BR-345 and HEA (1:1, TPO 2%, CB 0.5%) hysteresis curves, and (c) BR-345 and IBOA (1:1, TPO 2%, CB 0.5%) hysteresis curves.

Several trends were observed within the various material responses and are summarised here. Firstly, the polymers formed using IBOA had greater elongations at break than those formed using HEA. Second, polymers created with HEA showed significantly lower hysteresis in cyclic tests than IBOA-based formulations. Third, high concentrations of HEA created significant curling and surface roughness in the cured materials. Fourth, higher concentrations of TPO photoinitiator resulted in lower elongations at break. It was decided that the inclusion of both IBOA and HEA would produce a polymer with a good elastic strain and low hysterical losses.

For the final resin formulation, elongation at break was deemed a more important mechanical property than hysteresis loss, thus a ratio of IBOA to HEA of 2:1 was selected for the monomer diluent. Maintaining the 1:1 ratio of oligomers to monomers, this meant the ratio of BR-345 to IBOA to HEA was 5:3:2. With inclusion of the photoinitiator TPO at 2 wt%, this ratio equates to the portions of the final mass being BR-345 at 49 wt%, IBOA at 29.4 wt%, and HEA at 19.6 wt%. This formulation was designated ElastAMBER, after the AMBER research group at the University of Wollongong, and its elastomer nature.

4.3 Results and Discussion

4.3.1 Evaluation of the ElastAMBER Resin

The molecular weight (M_w) of the ElastAMBER (after blending) was compared with the molecular weight of the different components used in the preparation of the resin (Figure 4.5 (a)). After mixing the different chemical components at 60 °C under an inert atmosphere, it was observed that the resin presented three distinctive peaks at molecular weights of 39 235 g.mol⁻¹ (polydispersity index (PDI) of 1.1), 13 581 g.mol⁻¹ (PDI = 1.2), and 280 g.mol⁻¹. The difunctional polyether urethane acrylate (BR-345), which accounted for 49 wt% of the resin, presented the same peaks at the higher molecular weights 38 876 g.mol⁻¹ (PDI = 1.1) and 13 407 g.mol⁻¹ (PDI = 1.2), while the peak at the lowest molecular weight represents the M_w of the remaining components with a molecular weight between 116.2 g.mol⁻¹ (2-hydroxyethyl acrylate) up to 348.37 g.mol⁻¹ (diphenyl(2,4,6-trimethylbenzoyl)phosphine oxide) (Table 4.3). This result suggests that the blending of the different components of resin at higher temperatures leads to a homogeneous dispersion that made the ElastAMBER printable resin.

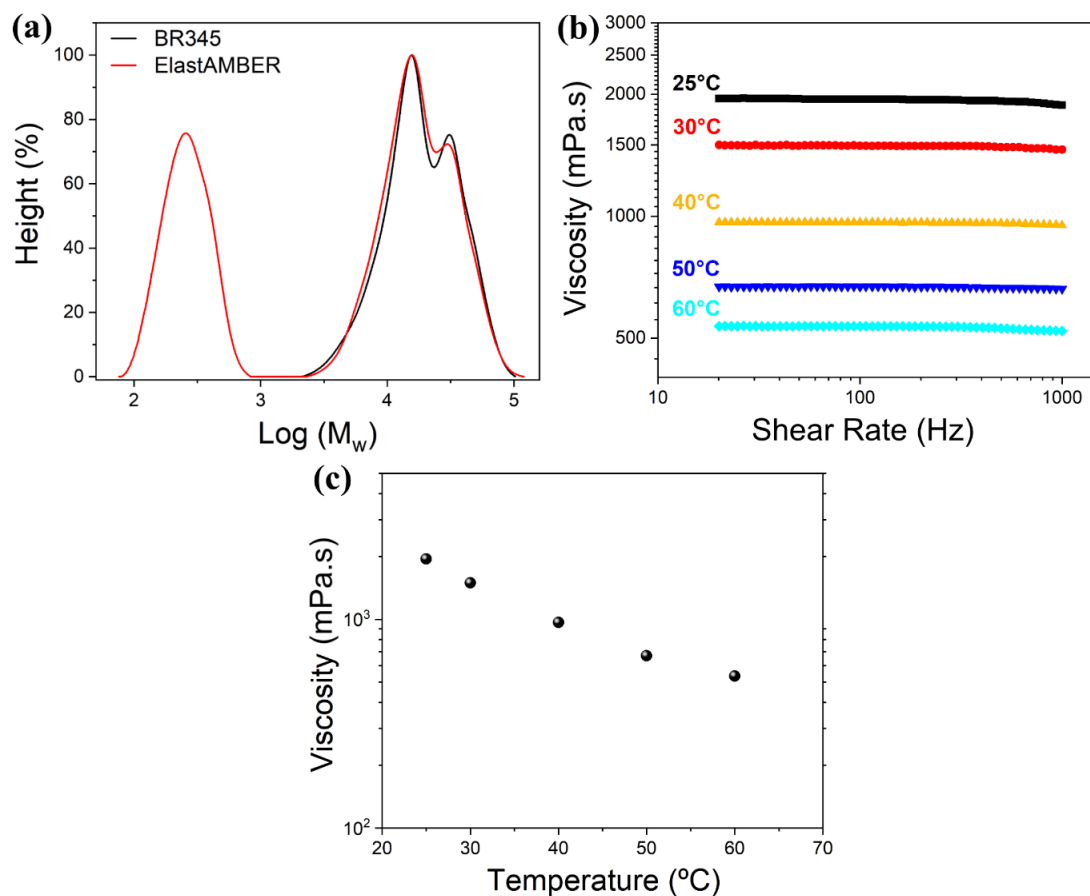


Figure 4.5 ElastAMBER resin properties: (a) GPC comparison between BR-345 oligomer and ElastAMBER resin, (b) resin viscosity with respect to shear rate, and (c) resin viscosity with respect to temperature.

Table 4.3 Molecular weights of the resin components from GPC.

Component	M_w (g.mol ⁻¹)	PDI
BR-345 Peak 1	38 876	1.1
BR-345 Peak 2	13 407	1.2
diphenyl(2,4,6-trimethylbenzoyl)phosphine oxide	348.37	-
2-hydroxyethyl acrylate	116.12	-
isobornyl acrylate	208.30	-
ElastAMBER Peak 1	39 235	1.1
ElastAMBER Peak 2	13 581	1.2
ElastAMBER Peak 3	280	1.1-

M_w : molecular weight, PDI: polydispersity index

The rheological properties play a crucial role in the formulation of a photopolymerising resin as it affects not just the speed and ease of printing, but more importantly the mechanical properties of the cured polymer [122]. The developed ElastAMBER resin viscosity showed a stable plateau all over the shear rate range tested (Figure 4.5 (b)), suggesting that the 3D printable resin have the characteristics of a Newtonian fluid. The ElastAMBER had a viscosity of almost 2 000 mPa.s at room temperature, which dropped below 1 000 mPa.s when heated to 40 °C (Figure 4.5 (c)). The viscosity was almost halved again to approximately 500 mPa.s once it reached 60 °C.

The dependence of the ElastAMBER viscosity (η) with the temperature (T) was modelled by an Arrhenius-type equation as follows:

$$\eta = Ae^{E_a/RT} \quad (4.1)$$

where, A is a pre-exponential factor and is related with the flexibility of the oligomer chains, R is the ideal gas constant (8.31 J.K⁻¹.mol⁻¹), and E_a is the apparent activation energy of the viscous flow. The E_a can be seen as a local transition of a molecule or a group of molecules from one state (before flowing to another), having to overcome an energy barrier. The ElastAMBER presented a value of 30.82 kJ.mol⁻¹, which is in the same range of the one reported for molten polyethylene (E_a =30 kJ.mol⁻¹) [166]. Further, a resin viscosity below 1 000 mPa.s is recommended for DLP printing [125]. The ElastAMBER can be printed with ease at near room temperatures (40 °C), a significant improvement over similar previous works, required temperatures of (70 to 75) °C to cross this printability threshold [81, 82].

4.3.2 Physical and Thermal Properties of 3D Printed ElastAMBER

Scanning electron microscopy was used to obtain clear images of the print lines (Figure 4.6). The first image, a cross-section of a mechanical specimen, clearly shows the printed layer lines (diagonal) and there are no microporosities or tears, indicating a continuous airtight polymer matrix. The samples are shown being stretched, bent, and twisted with ease in Figure 4.7.

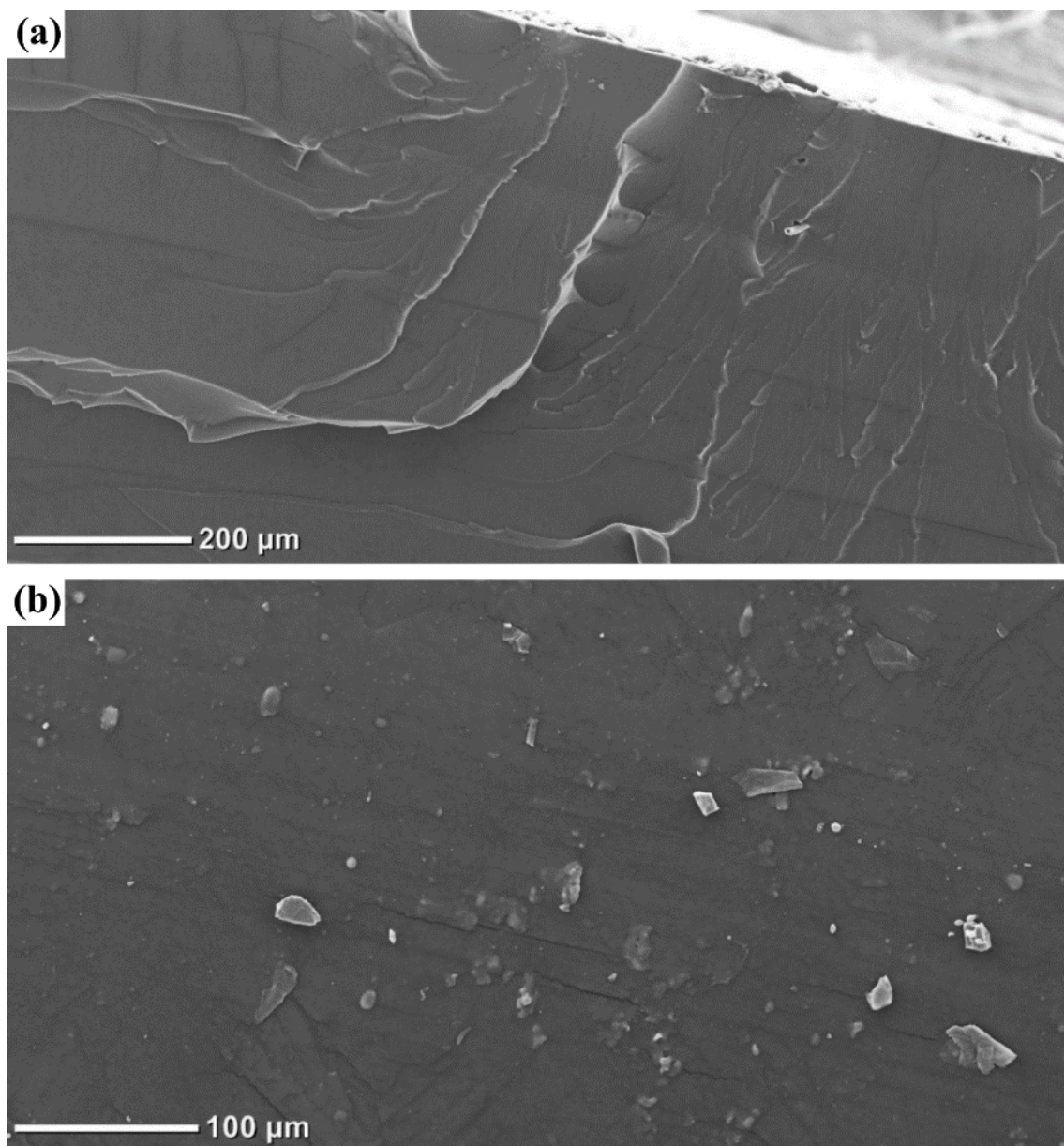


Figure 4.6 Scanning electron microscope images of (a) printed mechanical specimen cross-section and (b) elastomer surface.

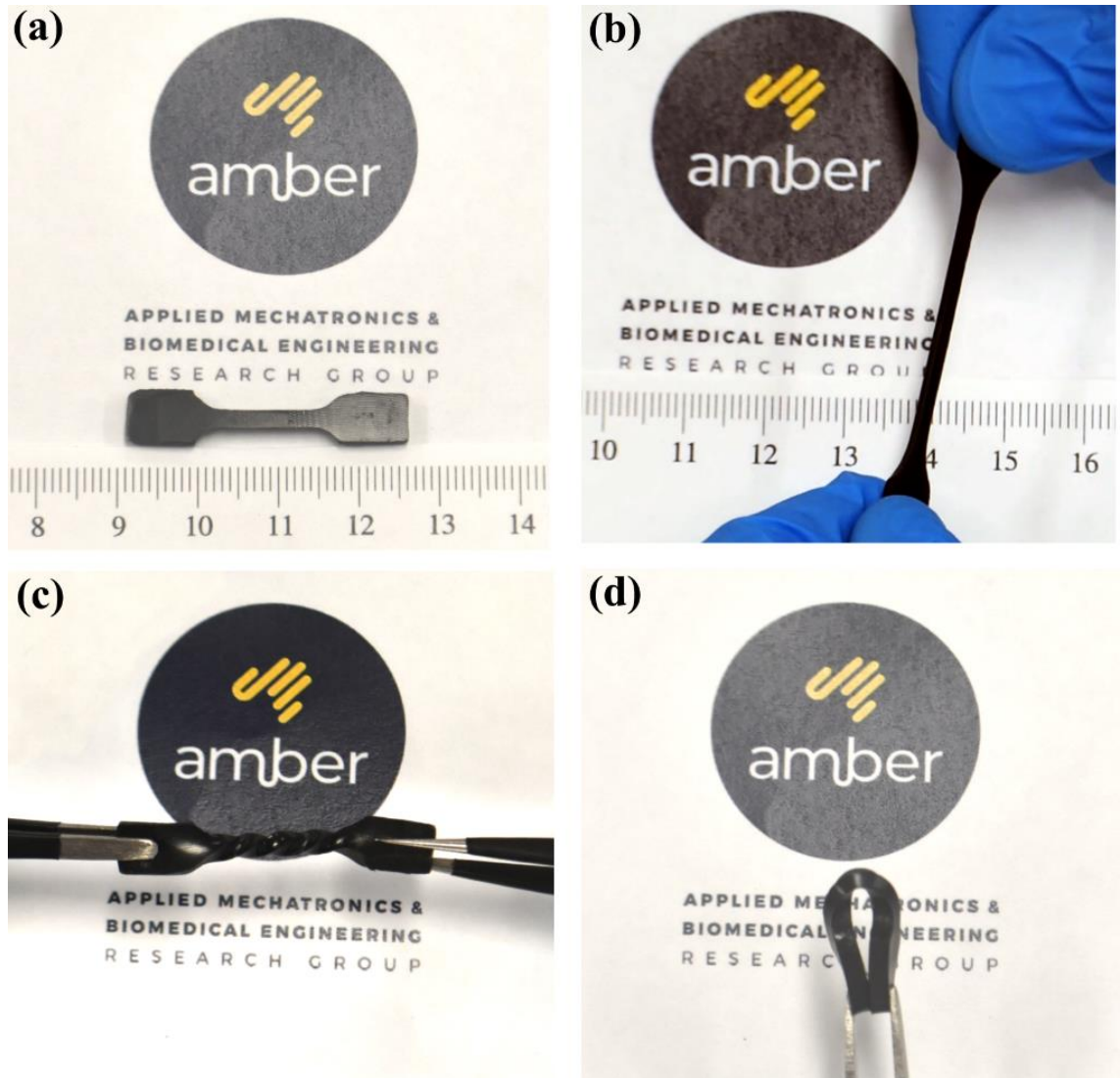


Figure 4.7 ElastAMBER specimen (a) measurement, (b) stretched 250%, (c) twisted 2.5 times, and (d) bent 180°.

Mechanical testing was performed on the dog-bone shaped 3D printed specimens to evaluate the mechanical performance of cured ElastAMBER. The polymer showed a Neo-Hookean rubber elasticity behaviour, characteristic of elastomeric materials, with an average extension ratio of 4.02 ± 0.06 , an ultimate tensile strength of (1.23 ± 0.09) MPa, and a Young's modulus of (579 ± 50) kPa, referenced at 100% elongation (Figure 4.8 (a)). Compared to other materials used in soft actuators, ElastAMBER shows remarkably high elastic strains, minimal permanent plastic deformation, and a low stiffness but can support its own weight. Other flexible DLP resins Spot-E and Formlabs Flexible fail at

extension ratios of 1.65 [108] and 1.85 [107], respectively, the common moulding silicone elastomer Sylgard-184 fails at 2.00 [77], while the FDM filament NinjaFlex yields at extension ratios of 1.65 [98]. ElastAMBER is also significantly more compliant than all these other materials, with the closest material Filaflex exhibiting a stiffness of 2.5 MPa, or four times more rigid [80].

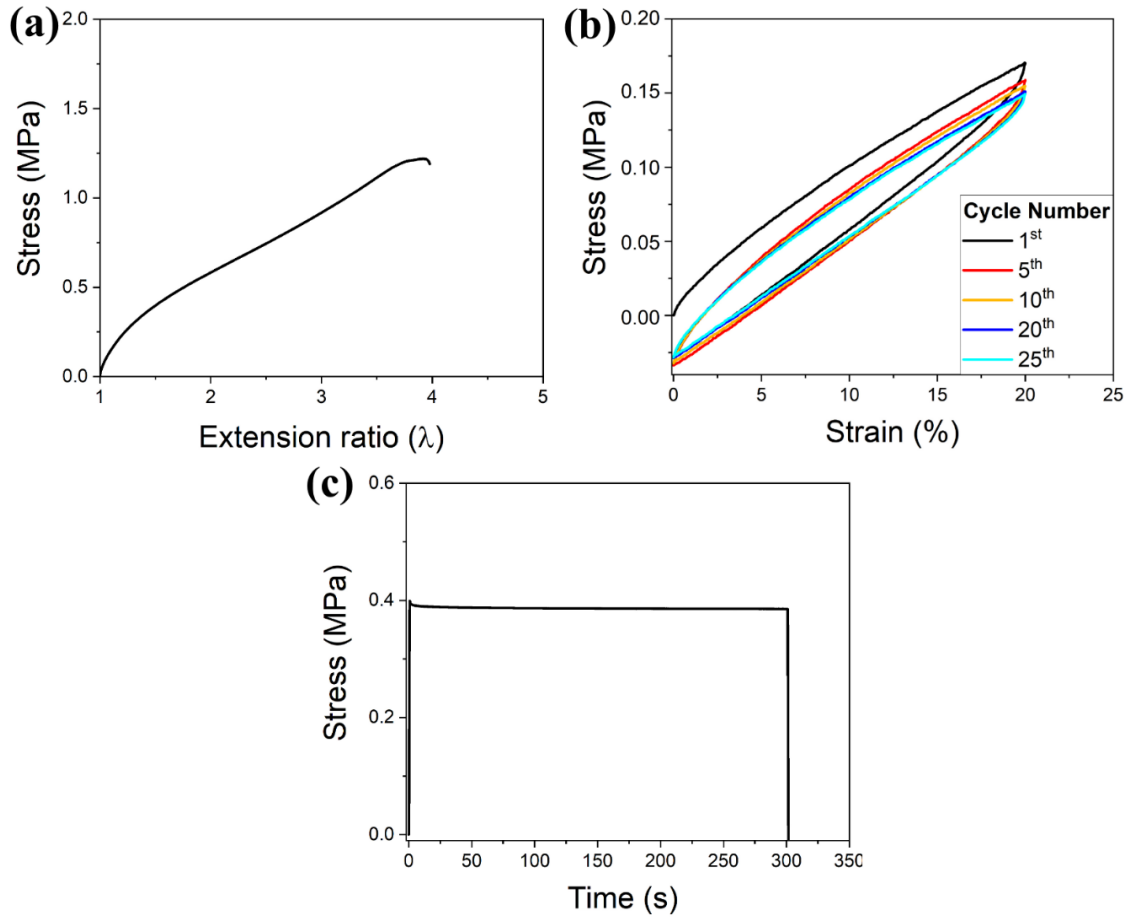


Figure 4.8 Mechanical responses (a) stress versus extension ratio, (b) hysteresis cycles, and (c) stress relaxation.

Ideally, an elastomer would react instantly to an applied stress, but most synthetic elastomers display viscoelastic behaviour which leads to the presence of a permanent deformation within cyclic mechanical applications [113, 135, 162]. The determination of reliable deformation characteristics and durability are necessary for selecting actuators used for soft robotic devices [32, 81]. Cyclic strain experiments were performed using ElastAMBER samples to obtain the

mechanical hysteresis curves and to quantify the amount of mechanical energy that is lost to heat between the loading and unloading stages. Successive cycles are shown to have a slight drift in the direction of decreasing stress, suggesting the presence of a permanent deformation during the cyclic experiment (Figure 4.8 (b)). The average drop in peak stress between each cycle was calculated to be 0.64 kPa, indicating a stable and reliable repetitive stress response.

Another property of elastomers is a stress-relaxation process after an instantaneous strain due to the viscoelastic nature of the elastomer [113, 162]. Stress-relaxation is the phenomenon where materials with a constant strain undergo a degree of decay in the stress response, with more viscous substances exhibiting a greater stress reduction across wider time periods [113, 167]. While this phenomenon does contribute to the hysteresis effect, it is on a fundamentally different time scale and is analysed separately [113, 168]. As seen in Figure 4.8 (c), ElastAMBER displays a negligible viscoelastic tendency, as the stress response over the five-minute duration is remarkably stable. The total stress relaxation is approximately 3.5%, which is completed within the first few seconds, demonstrating the highly elastic nature of the ElastAMBER elastomer.

Dynamic mechanical analysis (DMA) was performed to determine the effect of temperature upon the viscoelastic properties of polymers [104, 127]. As shown in Figure 4.9 (a), with the increase of temperature, a dramatic decrease in the storage modulus (E') occurred, associated with cooperative motion of the glass transition temperature (T_g). With further temperature increase, a stable rubbery plateau is observed, characteristic of cross-linked materials [169]. A relaxation process with a maximum in the loss factor ($\tan \delta = E''/E'$) can be observed in the maxima at approximately -54 °C. This was assigned to the cooperative segmental motion of amorphous regions of the polymer chains, characteristic of the T_g process [169].

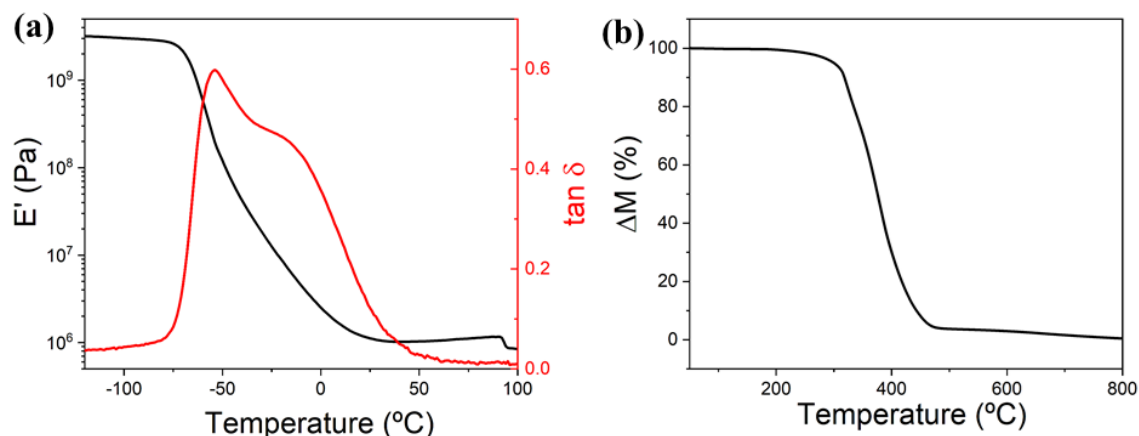


Figure 4.9 Thermal properties of ElastAMBER: (a) storage modulus (E') and the loss factor ($\tan \delta$) versus temperature for ElastAMBER and (b) elastomer mass loss versus temperature.

The thermal stability of the ElastAMBER was evaluated by thermal gravimetric analysis (TGA). Figure 4.9 (b) shows that the elastomer has no noticeable mass loss for temperatures below 300 °C. When the temperature increases, a strong mass loss is observed due to the release of the volatile compounds of the elastomer, and by increasing the temperature, no residue was detected at temperatures above 600 °C. These results shows that the ElastAMBER presents a wide temperature range of applications, from -54 °C (T_g) up to more than 100 °C, without loss of performance.

4.3.3 Evaluation of the Cross-Linking Density of ElastAMBER

An ElastAMBER printed part was immersed in tetrahydrofuran (THF) and the amount of solvent uptake was measured over time. A clear volume expansion was observed of more than double (Figure 4.10 (a)) after immersing the sample in THF (Figure 4.10 (b)). The swelling degree (Equation 3.2), represents the amount of liquid that the sample could absorb over time, shows that the 3D printed part could absorb more than four-fold its own weight (Figure 4.10 (c)). This behaviour suggests that the UV light energy used during the DLP printing process was effective in starting the polymerisation process of the ElastAMBER resin, creating cross-linking sites between the polymer chains.

After printing, the density of the ElastAMBER was found to be $(1.037 \pm 12.4) \text{ kg.m}^{-3}$, as determined using the pycnometer method. This is very near the density of water and lighter than other materials used in soft actuators, such as Spot-E [108] (1.100 kg.m^{-3}), NinjaFlex [98] (1.190 kg.m^{-3}), Filaflex [80] (1.070 kg.m^{-3}), and other polyurethane-based polymers [113] (1.050 kg.m^{-3} to 1.250 kg.m^{-3}).

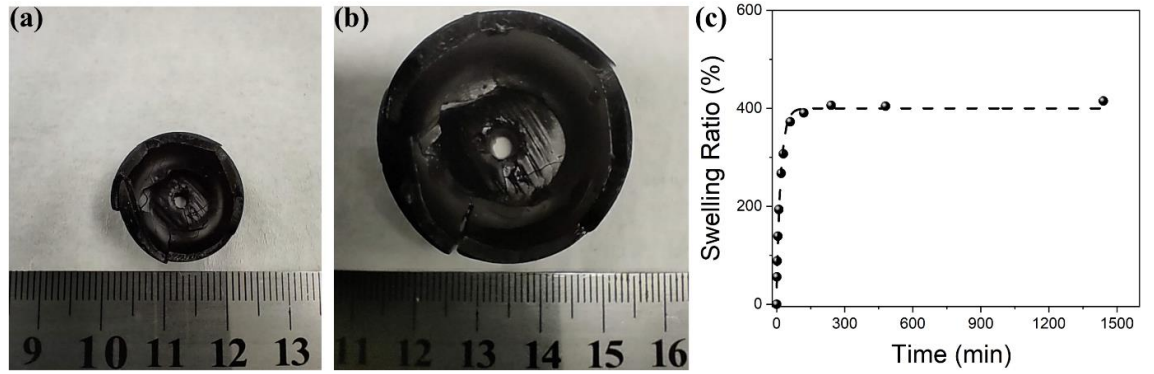


Figure 4.10 Swelling experiment: (a) dry polymer sample, (b) polymer sample completely swollen with THF, and (c) polymer swelling ratio with respect to time.

The swelling degree is a valuable method to evaluate the cross-linking density of an elastomer and evaluate the effective curing of the ElastAMBER. The density of the chemical bonds in a network influences the polymer's mechanical properties such as toughness, strength, hysteresis, and permanent set [169]. The cross-linking density (n) of the polymer network can be calculated using the Flory-Rehner theory:

$$n = \frac{1}{2} \frac{\ln(1 - v_2) + v_2 + \chi v_2^2}{v_1 \left(\frac{v_2}{2} - v_2^{\frac{1}{3}} \right)} \quad (4.2)$$

and

$$v_2 = \left(1 + \left(\frac{m_{eq} - m_d}{m_d} \right) \left(\frac{\rho_2}{\rho_1} \right) \right)^{-1} \quad (4.3)$$

where v_2 is the volume fraction of polymer at swelling equilibrium, χ is the Flory-Huggins parameter for polymer-solvent interaction, v_1 is the molar

volume ($\text{m}^3\cdot\text{mol}^{-1}$) of the solvent (THF), and ρ_1 and ρ_2 are the densities ($\text{kg}\cdot\text{m}^{-3}$) of the solvent and polymer respectively [163, 170]. For elastomeric materials, the cross-linking density is also related with the polymer modulus of elasticity, according to:

$$E = 3RTn \quad (4.4)$$

where E is Young's modulus of elasticity (Pa), R is the universal gas constant ($\text{J}\cdot\text{mol}^{-1}\cdot\text{K}^{-1}$), and T is the temperature (K). Combining Equation 4.2 and 4.4 allows the determination of the Flory-Huggins parameter (χ):

$$\frac{E}{3RT} = \frac{1}{2} \frac{\ln(1 - v_2) + v_2 + \chi v_2^2}{v_1 \left(\frac{v_2}{2} - v_2^{\frac{1}{3}} \right)} \quad (4.5)$$

The cross-linking densities present in this elastomer were calculated to be $78.7 \text{ mol}\cdot\text{m}^{-3}$ using the chemical swelling method, and $79.6 \text{ mol}\cdot\text{m}^{-3}$ using the mechanical method, and are similar to the ones reported for the PDMS elastomer [171]. Moreover, the average molecular weight between cross-links ($M_c = \rho/n$) that is related with the fraction of polymer chain bounded at both ends by active network chain segments is $13.2 \text{ kg}\cdot\text{mol}^{-1}$. It has been reported that PDMS presents a M_c of $10 \text{ kg}\cdot\text{mol}^{-1}$ [172], while natural rubber presents a value of $70.1 \text{ kg}\cdot\text{mol}^{-1}$ [172]. The Flory-Huggins parameter is a constant for a specific of a polymer-solvent pair and is not influenced by the cross-linking density of the elastomeric chains [169]. In this work, a value of 0.36 was calculated for χ , which reveals that the THF can be classified as a “good solvent” for the ElastAMBER [173].

A comparison between the physical properties of the ElastAMBER elastomer and other elastomeric materials used in soft robotics is summarised in Table 4.4. The developed 3D printable oligomer present remarkable elastomeric properties than those previously reported, including Young's modulus, extension ratio, and ultimate tensile strength, which makes them highly desirable for the next generation of soft robotics and human-machine interfaces.

Table 4.4 Comparison between ElastAMBER and other elastomeric materials.

Material	E (MPa)	σ_{max} (MPa)	λ_{max}	ρ (kg.m ⁻³)
This work	0.579	1.23	4.02	1 037
Sylgard-184 [77]	3.9	3.9	2.00	982
NinjaFlex [98]	12	26	7.60	1 190
Filaflex 60A [80]	2.5	26	10.5	1 070
Spot-E [108]	12	11	1.65	1 100
Formlabs Elastic 50A [114]	0.94	3.23	2.60	N/A
SUV elastomer [82]	7.6	7.5	12.0	N/A

E : Young's modulus, σ_{max} : ultimate tensile strength, λ_{max} : extension ratio at break, ρ : density

5 LINEAR SOFT MULTI-MODAL ACTUATORS

5.1 Introduction

The new soft elastomeric resin ElastAMBER was used in the DLP printing of the linear soft multi-mode actuators (LSOMMAs), which could provide significant contractile and extensile forces under negative and positive pressures, respectively. The main feature of the LSOMMA is to produce bidirectional actuation *in the same design* (Figure 5.1), widening their application prospects. This is a significant advantage over most other soft actuators, as the dual operating mode allows for both push and pull actions to be performed. Additionally, for operations requiring the rapid switching of actuators between states, the application of the opposite pressure type provides faster responses than passive material restoration. Significantly, the magnitude of differential pressure required to deform the actuator is greatly reduced. This allows for smaller and cheaper pneumatic pumps to be used, thereby smaller autonomous devices can be created for small-scale applications. The LSOMMA actuators are referred to by their number of chambers and face diameter. For example, the LSOMMAs with one chamber and face diameters of 20 mm are called “1C 20 mm”. The primary dimensions and mass of each LSOMMA type assessed in this thesis are shown in Table 5.1. The LSOMMA was manufactured using DLP 3D printing, as opposed to moulding, as printing allowed for the actuator to be monolithic and seamless. The elimination of joining multiple moulded parts using adhesives allows for better material performance and fewer points of weakness.

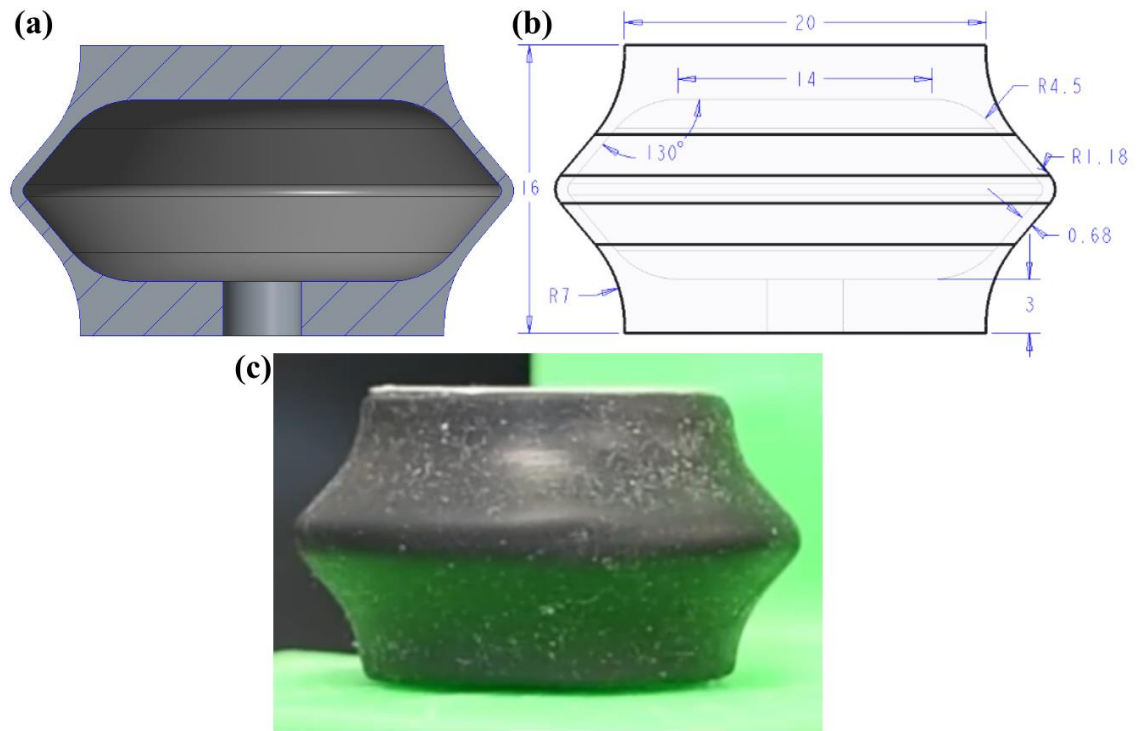


Figure 5.1 A one chamber 20 mm face diameter LSOMMA: (a) cross-sectional side view, (b) side view with dimensions labelled, and (c) photo.

Table 5.1 Dimensions and mass of LSOMMA units.

Actuator	L_0 (mm)	D_f (mm)	t_w (mm)	m (g)
1C 20 mm	16	20	0.68	2.74
1C 14 mm	11.2	14	0.48	0.92
3C 14 mm	29.4	14	0.48	2.04

L_0 : undeformed length, D_f : face diameter, t_w : wall thickness, m : unit mass

5.2 Actuator Performance

Experimental tests were performed to gauge the pressure limits of the LSOMMAs. The vacuum pressure required for complete contraction of the actuators was discovered to be approximately -25 kPa. Vacuum pressures up to -70 kPa (the limit of the motor-pump) were tolerated without issue. When testing for the maximum operable positive pressure, some actuators tolerated pressures up to 100 kPa without damage, although at pressures above 80 kPa

the inflation became irregular and the actuators began ballooning. While the LSOMMAs can perform under higher pressures, this study focused on a maximum of 75 kPa differential pressure for general expansion tests. The initial, fully expanded, and fully contracted positions of a three chamber 14 mm base diameter LSOMMA can be viewed in Figure 5.2.

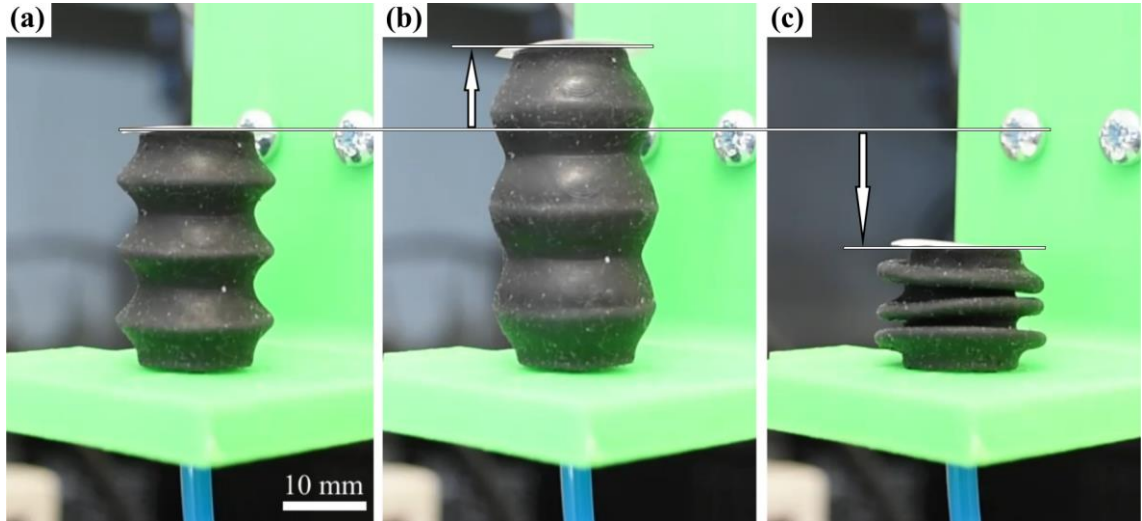


Figure 5.2 A 3C 14 mm LSOMMA: (a) unpressurised (b) with 75 kPa applied, and (c) with -25 kPa applied.

Scalability

Three actuator configurations were chosen to be studied. The first, a single chamber LSOMMA with 20 mm base diameter, was selected so that direct comparisons of performance can be made between this study and the vacuum linear actuators reported by Tawk *et al.* [79]. In order to assess scalability, the first actuator was scaled down by 70% to create the second actuator. This allowed a comparison between size and performance and provided insights into the effect of wall thickness. The third actuator was created with three separate pneumatic chambers and was scaled down similarly to the second actuator type. The additional chambers allow for a greater actuation deformation whilst maintaining its minimal cross-sectional area. These actuators are referred to as 1C 20 mm, 1C 14 mm, and 3C 14 mm, respectively. Actuator performance was measured using a step input of

pressure as well as a ramp input to provide insight into the transient and hysteresis effects of the viscoelastic material on the operating metrics. The step input performance and critical geometric properties of the LSOMMAs are summarised in Table 5.2.

Table 5.2 Performance parameters of the LSOMMAs under step inputs.

Actuator	ΔP (kPa)	δ (mm)	ε (%)	F (N)	T_r (ms)	ω_b (rad.s ⁻¹)	L_t (cycles)
1C 20 mm	75	5.09	31.8	19.4	252	18.1	8 132
	-25	-7.59	-47.4	-5.46	145	11.9	>50 000
1C 14 mm	75	3.60	32.1	9.10	91	38.1	11 911
	-25	-5.19	-46.3	-3.06	57	26.8	-
3C 14 mm	75	10.3	37.1	12.3	200	17.7	10 353
	-25	-14.6	-49.7	-3.14	127	11.0	-

ΔP : operating gauge pressure, δ : linear displacement, ε : actuation strain, F : blocked force, T_r : rise time, ω_b : estimated 3dB bandwidth, L_t : cycles before failure

Step Response

The linear displacements of the actuators under a variety of step pressure inputs were recorded over time (Figure 5.3). Upon vacuum pressurisation, the LSOMMAs rapidly contracted in length, and restored to their initial positions when the vacuum was released back to atmospheric pressure. Similarly, positive pressurisation resulted in a swift elongation in the axial direction. The rise times were shorter than the fall times due to the passive nature of the latter. The viscoelastic strain relaxation of the ElastAMBER material caused the final sections of the dynamic motions in both directions to be prolonged, which is especially evident in the 10% to 0% sections of the return stroke. Compared to the smaller units, the 1C 20 mm units were more significantly affected by the interior walls sticking together on vacuum tests, with a greater wall contact area to be separated on the return stroke, prolonging the fall times. Additionally, the actuators with more chambers showed a slightly higher strain response, likely a

result of having a greater proportion of unit length in the active region. Some displacement overshoot can be observed at lower positive pressures. This is attributed to the regulator settings causing pressure overshoot to affect faster response times.

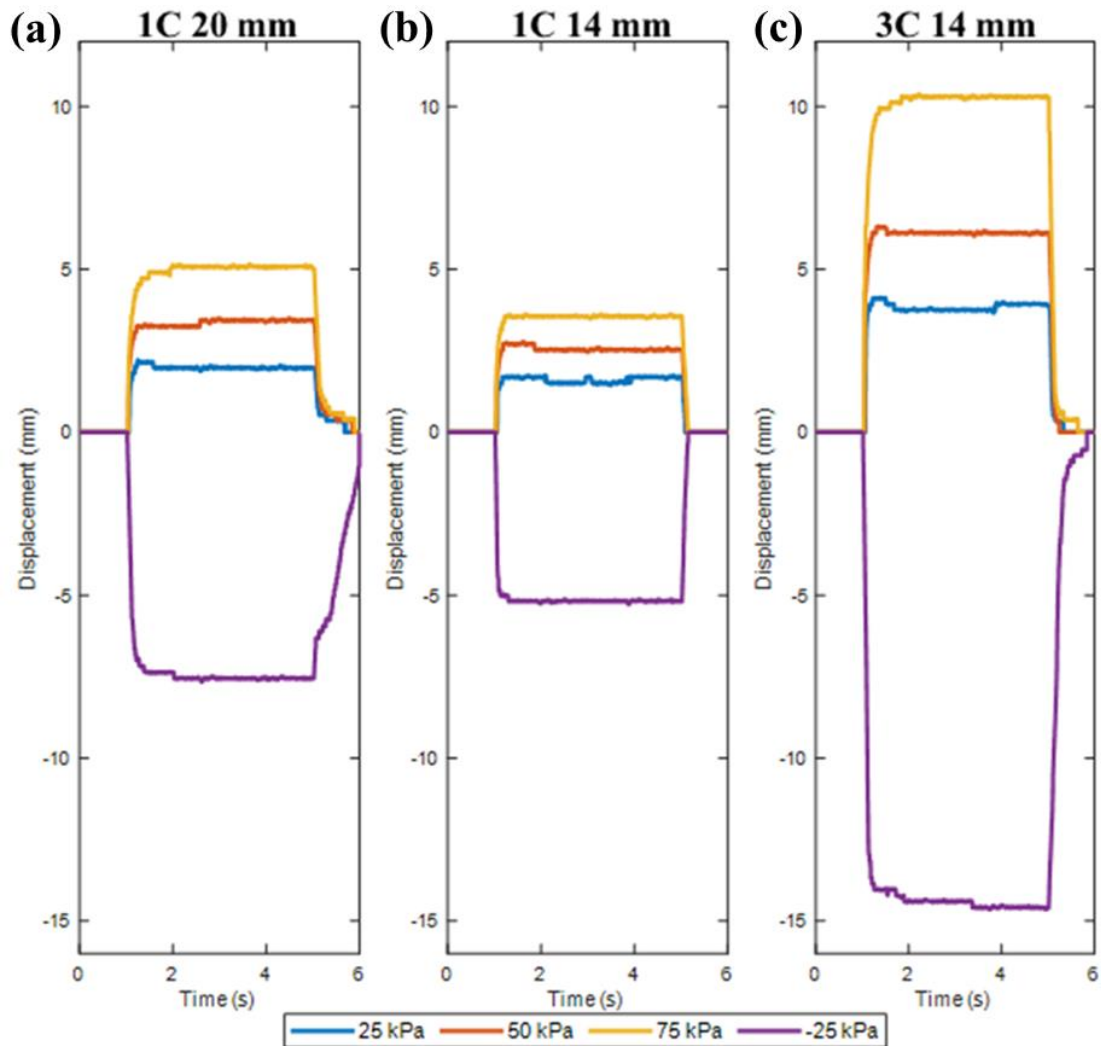


Figure 5.3 Displacement responses to step inputs (a) 1C 20 mm step responses, (b) 1C 14 mm step responses, and (c) 3C 14 mm step responses.

The complete range of motion for the 3C 14 mm LSOMMA from fully contracted to fully extended is 24.9 mm. If multi-mode operations are not required, the LSOMMA could easily be configured to start at one end of motion by pre-loading it, which would provide enhanced stroke functionality. The actuator, if initially held at -25 kPa, having a height of 14.8 mm, produces an

elongation of 168% when pumped to 75 kPa. Similarly, the magnitude of contraction can be improved by beginning the motion from an extended state. This adds to the versatility of the LSOMMA by expanding its stroke range while maintaining the ability to both push and pull.

Hysteresis

Hysteresis is the loss of mechanical energy in a system through heat, measured by applying a dynamic closed cycle to the material. The hysteresis curves were obtained by applying a pressure ramp of 1 kPa.s^{-1} to the actuator from zero to maximum, and then back to zero, plotting displacement with respect to internal pressure (Figure 5.4). The area between the loading and unloading curves is an indicator of how much loss there is in the system. The curves also show where the critical pressure regions lie for the actuator, that is, the pressure range across which most of the deformation occurs. The displacement response of the LSOMMAs, like most other soft pneumatic devices, are non-linear. However, the displacement responses under positive pressures show higher linearity than the contractions under the vacuum, as seen in the hysteresis plots. Originally, the actuator was designed only to buckle under a certain vacuum pressure range to produce the linear displacement, which appears as a non-uniform relation between pressure and displacement. The buckling phenomenon does not occur under positive pressure, thus the relation is more uniform.

The displacement hysteresis between the output strokes and the return strokes for positive pressures is essentially zero, with the difference arising from the sensitivity step of the displacement sensor. The larger hysteresis magnitudes in the vacuum tests are due to the interior annular surfaces of the contracted actuator remaining stuck together while pressure is being released. In particular, the 'S' shaped discontinuity in the return stroke (Figure 5.4 (c)) occurred when the last stuck section peeled off, and the actuator jumped upright. This peeling phenomenon can be reduced by a minimum operating

vacuum pressure of greater than or equal to -20 kPa, UV post-curing the inside of the actuator, and adjusting the wall geometry.

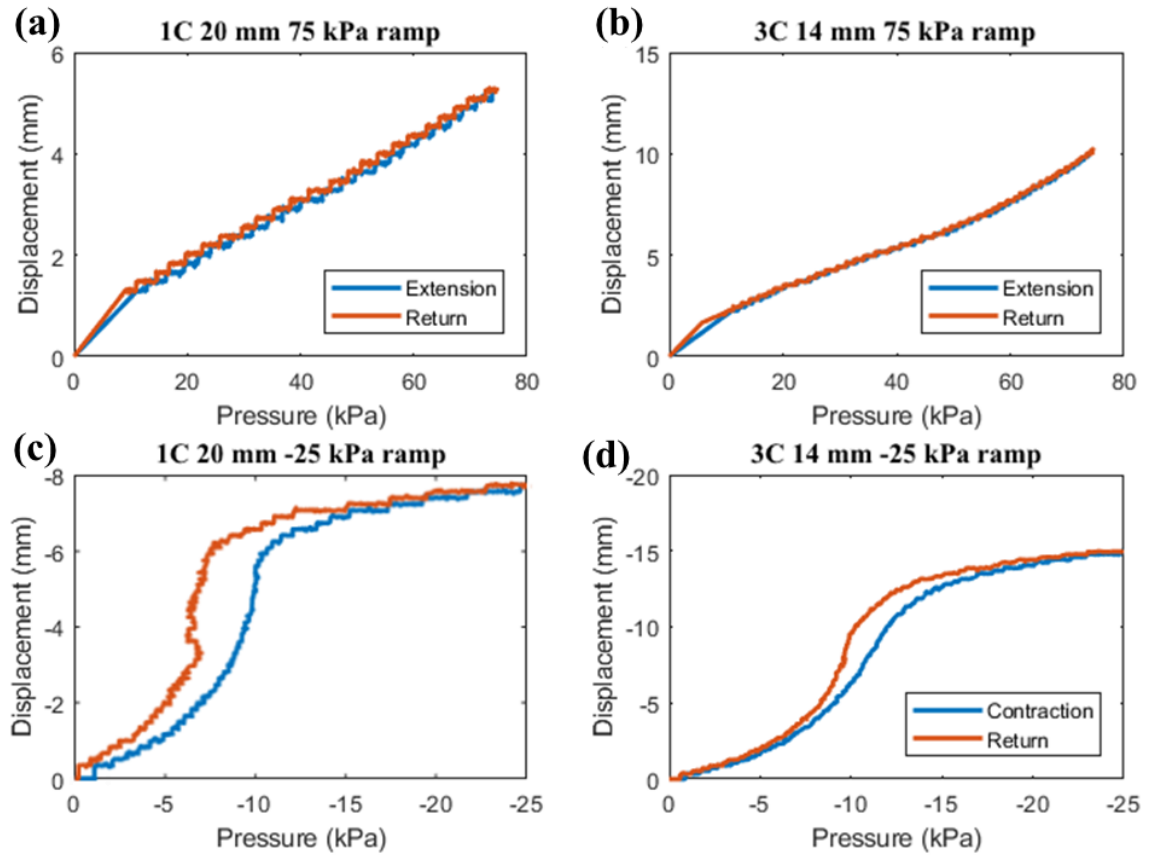


Figure 5.4 Hysteresis curves of ramped pressure cycles in LSOMMAs (a) 1C 20 mm 75 kPa, (b) 3C 14 mm 75 kPa, (c) 1C 20 mm -25 kPa, and (d) 3C 14 mm -25 kPa.

Bandwidth and Rise Times

The bandwidth of an actuator is directly related to the maximum actuation frequency at a given load. The -3 dB bandwidth was calculated for the actuators using the step response data for both positive and negative pressures. The bandwidths obtained are known to be hardware dependent, as the regulators limit the pressure rate to produce a less dynamic response curve. The bandwidth was also seen to be dependent on the internal volume of the actuator, as larger spaces require more transfer of air for pressure change, thus take a longer time. The step responses for each experiment were used to

estimate transfer functions in MATLAB, from which the Bode plots (Figure 5.5) and bandwidths were calculated (Table 5.2). As was to be expected, the actuators with smaller volumes had faster rise times than the larger actuators. For the same actuator, contractions had faster rise times than expansions.

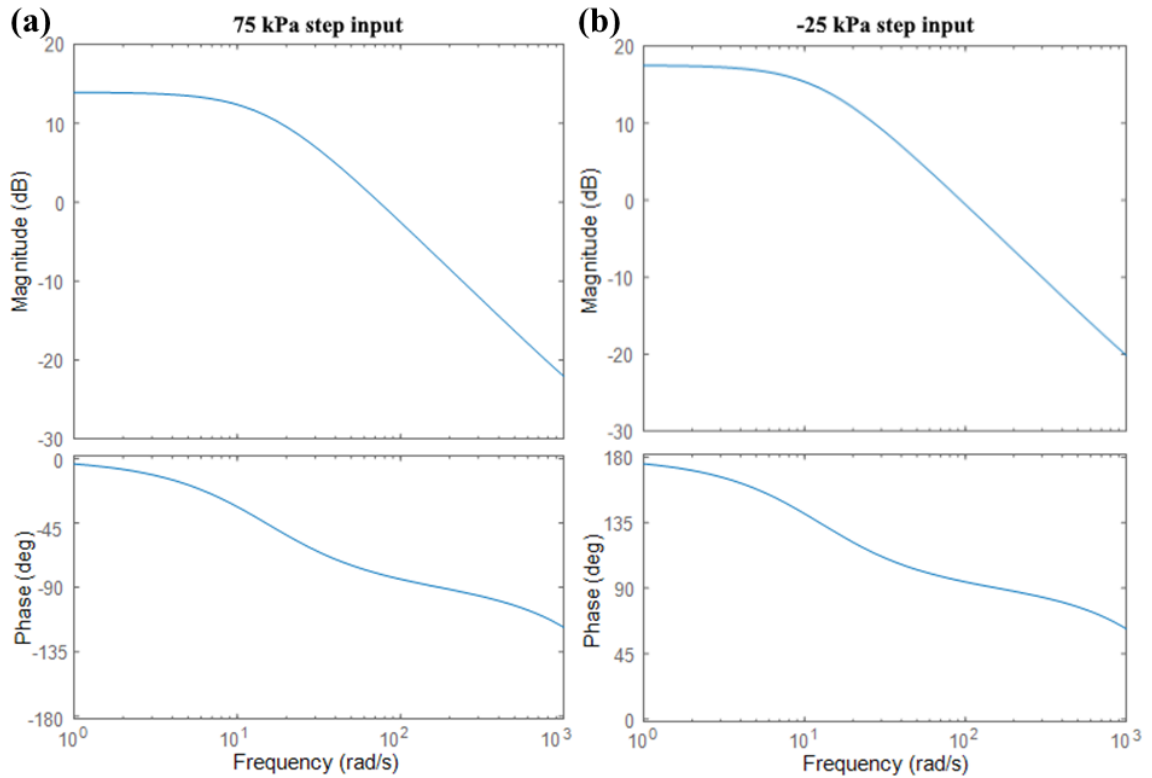


Figure 5.5 Bode plots for a 1C 20 mm LSOMMA (a) at 75 kPa and (b) at -25 kPa.

Pressure Stability

By maintaining the pressure input and measuring the change in the displacement of the actuator over time, one may ascertain if an actuator suffers from any substantial creep. As regulators would systematically adjust for pressure decays in a closed system, a 10 mL pneumatic syringe was used in place of the regulators to provide system pressure, allowing for accurate measuring of the potential pressure decay. The 1C 20 mm actuators had ± 25 kPa pressurisation which was maintained for a duration of 30 minutes, showing minimal pressure decay and a displacement fluctuation attributable to one step of the laser displacement sensor analogue output (Figure 5.6 (a) and (b)). In the highest recorded case, the pressure drop was 0.8 kPa (or 3.2% of the

step input pressure) and is most likely a result of air escaping through the pneumatic fittings.

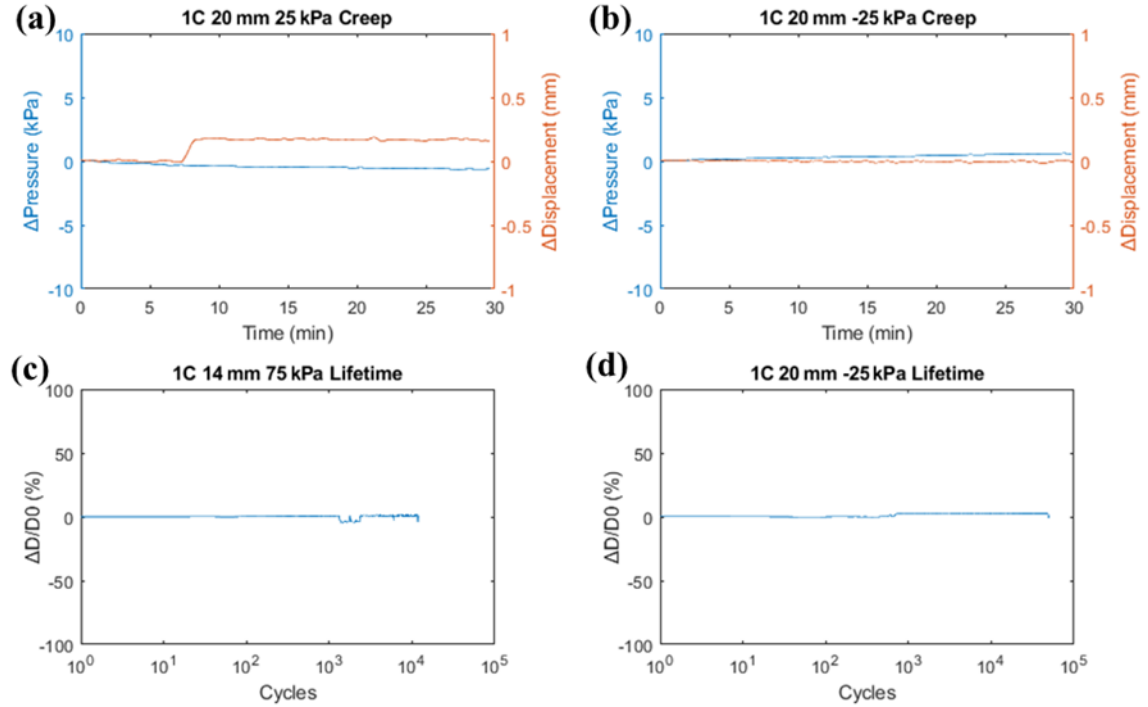


Figure 5.6 Actuator creep and lifetime (a) 1C 20 mm held at 25 kPa showing pressure and displacement creep, (b) 1C 20 mm held at -25 kPa showing creep, (c) 1C 14 mm showing stroke lifetime at cycles of 75 kPa, and (d) 1C 20 mm showing stroke lifetime at cycles of -25 kPa.

Lifetime

An estimate of the cycle durability of the soft material LSOMMA was determined by recording the number of inflation or deflation cycles completed before actuator failure. As positive pressure creates more stress and is more likely to result in tearing or rupturing during expansion, it was used to determine the actuator lifetime, over the much gentler vacuum contractions [37]. The test was conducted at a pressure of 75 kPa, a frequency of 1 Hz, and a duty cycle of 50%. The 1C 20 mm LSOMMA showed a lifetime of over 8 000 cycles, while the thinner walled actuators both lasted over 10 000 cycles before failure (Figure 5.6 (c)). The most common location of failure was just above the outer supports, where the unsupported overhang is at a maximum

during printing. This defect, which took the shape of a shallow notch across a small arc, is due to the imperfect fusion of the thin-walled layers at high overhang angles (Figure 5.7). The other area where ruptures were likely to occur was along the widest circumference of the LSOMMA, where the cross-section's radius of curvature is highest. A 1C 20 mm LSOMMA was also evaluated for its lifetime under cyclic vacuum pressures of -20 kPa, surviving over 50 000 cycles without rupturing or significant change in stroke (Figure 5.6 (d)).

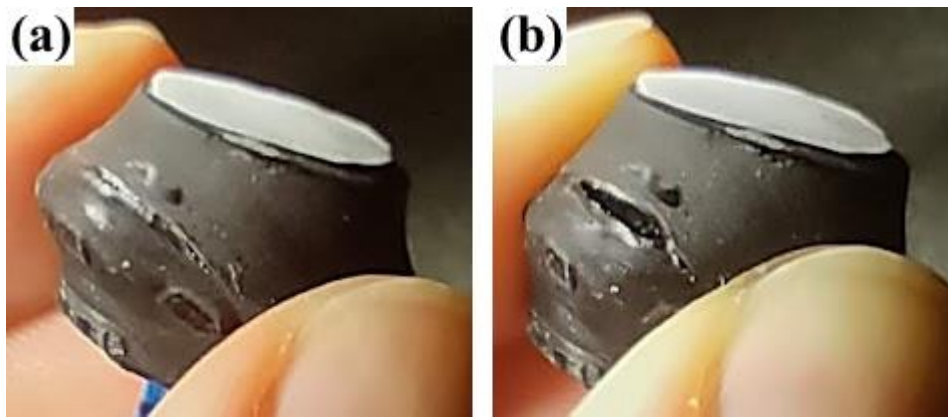


Figure 5.7 1C 14 mm LSOMMA after failure: (a) imperfection in the wall and (b) failure at imperfection shown by squeezing the actuator.

Absolute Limit

A destructive test was performed to determine the limit of positive pressure the actuator can sustain without failure and to observe the mode of failure. With the LSOMMA clamped and vertical displacement being recorded, a pressure ramp of 1 kPa.s^{-1} was applied until the actuator burst (Figure 5.8). The 1C 20 mm LSOMMA exhibited roughly linear expansion with respect to pressure up to 85 kPa mark, yielding a displacement of 6.5 mm. As pressure increased further the actuator ballooned rapidly and exponentially, until failing at 101 kPa and 27.7 mm. The mode of failure was a clean horizontal tear in the wall where the LSOMMA is the widest in diameter, across a $\sim 60^\circ$ arc. As the tear did not occur between two printed layers, this supports the theory that the DLP printing process created a complete three-dimensional polymer matrix.

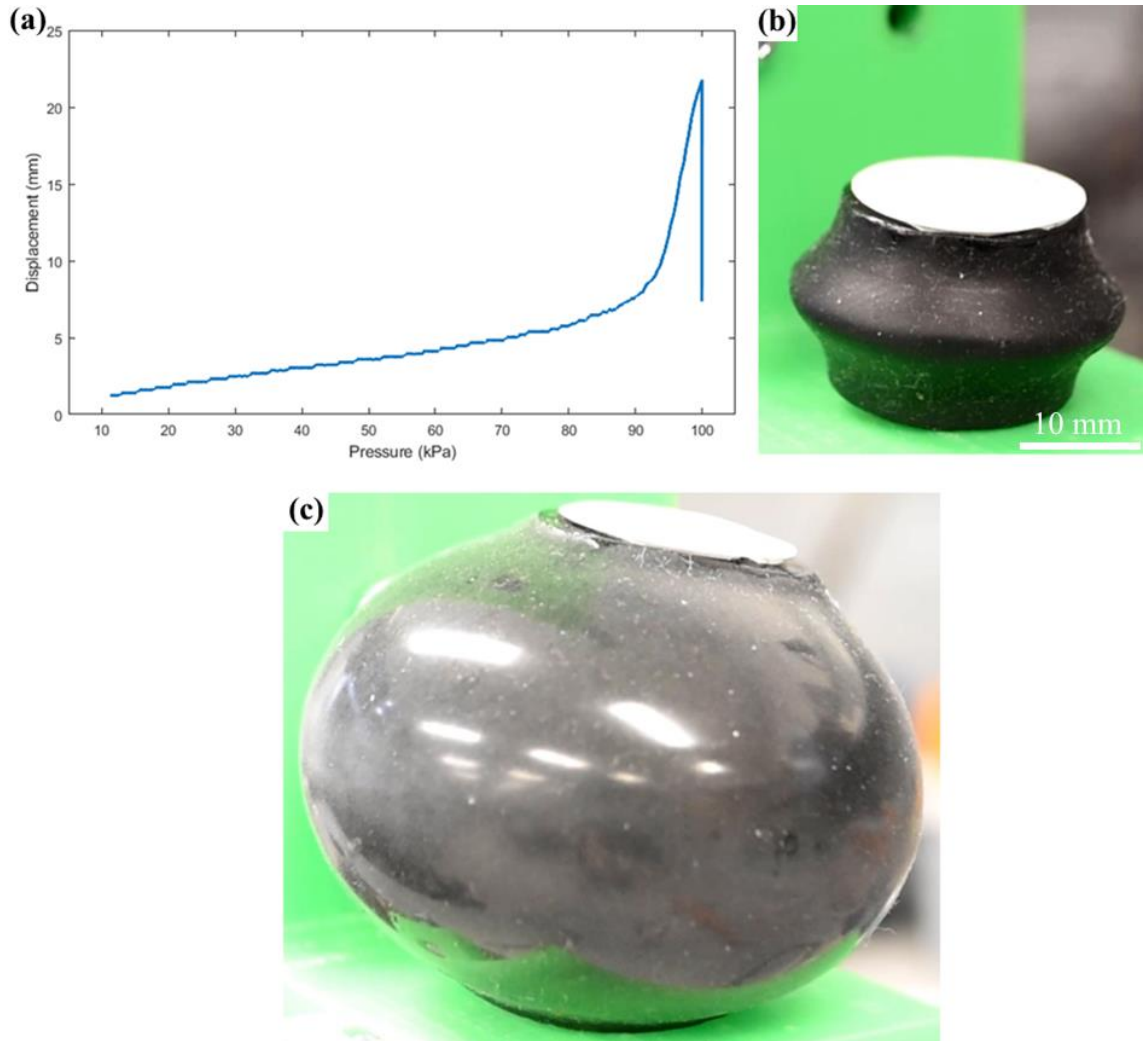


Figure 5.8 Destructive test on a 1C 20 mm LSOMMA (a) pressure-displacement graph, (b) unpressurised LSOMMA, and (c) LSOMMA at 101 kPa.

Blocked Force

The actuators were pressurised under step inputs while the blocked force outputs were recorded. It was observed that the force was roughly proportional to the area of the actuator. These findings are supported by the assertion made by Tawak *et al.* [79] that blocked force is independent of actuator length. Despite not testing the LSOMMAs at such extreme pressures of 95.7% vacuum, one may assume the blocked forces created at those pressures would be lower than those of the LSOVAs. This is because stiffer materials do not stretch as much and can transfer greater forces [92]. As noted previously, the stretchable material used in the presented actuators would absorb some of the energy supplied to the

system to be used as deformation, which creates internal stresses opposing those of applied blocked forces.

5.3 Electromechanical Behaviour of ElastAMBER Actuators

The capacitive electromechanical behaviour of the LSOMMA was analysed to assess the relationship between displacement and capacitance of a unit (Figure 5.9 (a)). Experiments were performed for the following pressure input sequences: step inputs, ramp inputs with a gradient of $\pm 1 \text{ kPa.s}^{-1}$, and pressure held at 20 kPa for one hour. The extension of the actuator under the applied pressures caused a decrease in the capacitance reading, while the actuator's contraction significantly increased the measurement. A strong correlation was found between the pressure and the capacitance readings, implying one latter is dependent upon the former. There is no observable lag between the air pressure signal and the capacitance response, indicating the response is instantaneous (Figure 5.9 (b)). The capacitance creep, as can be seen in Figure 5.9 (c), is less than 1% across the entire hour duration. The plateauing of the capacitance in Figure 5.9 (e) is due to the interior surfaces of the actuator coming into contact, with the closing of the internal voids increasing the contact area. As the capacitance is distinctly dependent upon the air pressure within the actuator, it would be possible to use the LSOMMA as a dual actuator-sensor device. When properly calibrated, this would allow a control scheme to be built in which the actuator can also be used as an intrinsic sensor, reducing the size and complexity of the system.

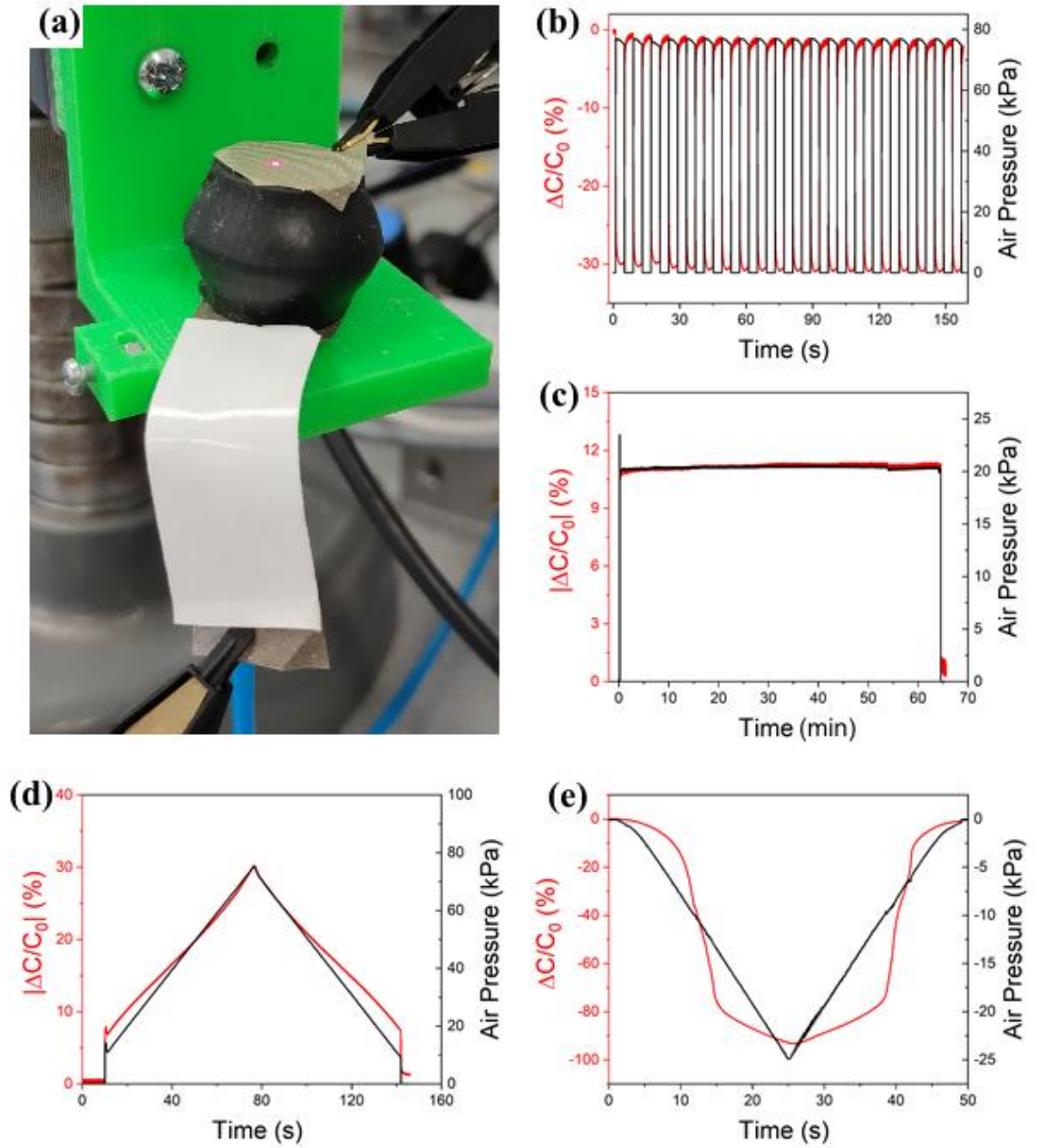


Figure 5.9 Relationship between the change in capacitance and the air gauge pressure. (a) 1C 20 mm LSOMMA with capacitive probes connected, (b) positive pressure step inputs, (c) positive pressure step held for an hour, (d) positive pressure ramp input, and (e) vacuum pressure ramp input.

5.4 Finite Element Analysis

Finite Element Analysis (FEA) was performed to verify and predict the material and actuator behaviours under various conditions. An Ogden 1st Order

model (Table 5.3) was selected to represent the elastomer's nature and calculated using the previously evaluated tensile data in Section 4.3.2.

Table 5.3 Elastomer hyperelastic material model constants.

Hyperelastic Material Model	Material Constant	Value (units)
Ogden 1 st Order	μ_1	0.49333 (MPa)
	A_1	1.6388 (unitless)
	D_1	0 (MPa ⁻¹)

FEA computer simulations were performed using ANSYS Mechanical Workbench (v18.2, ANSYS Inc.) software on LSOMMA models. The results of the FEA simulations closely resemble the results of the experiments (Table 5.4). The small degree of variation is largely be attributed to the imperfect geometries of the printed models, but also to the meshing and material approximations. As such, it is reasonable to use FEA simulations to accurately predict and optimise the dynamic performance of the LSOMMA designs. The results support the observations made during this study that the highest strains occur at the widest parts of the chambers, where the radius of curvature is highest along the thin walls (Figure 5.10). It can also be seen that a positive pressure of 75 kPa produces almost three times as much maximum elemental stress and strain within the walls as the vacuum -25 kPa pressure does. These results also confirm the widest part of the wall to be the location of maximum stress under positive pressures, where actuator failure often took place.

Table 5.4 Comparison of LSOMMA performance with FEA predictions.

Actuator	ΔP (kPa)	δ_{EXP} (mm)	δ_{FEA} (mm)	$\Delta\delta$ (%)	F_{EXP} (N)	F_{FEA} (N)	ΔF (%)
1C 20 mm	75	5.09	5.04	0.99	19.4	20.8	6.97
	-25	-7.59	-7.35	3.21	-5.46	-6.39	15.7
1C 14 mm	75	3.60	3.39	6.01	9.10	10.1	10.4
	-25	-5.19	-5.30	2.09	-3.06	-3.04	0.66
3C 14 mm	75	10.3	10.5	1.92	12.3	11.2	9.36
	-25	-14.6	-15.7	7.26	-3.14	-3.10	1.28

ΔP : operating gauge pressure, δ_{EXP} : experimental linear displacement, δ_{FEA} : FEA linear displacement, $\Delta\delta$: displacement percent difference, F_{EXP} : experimental force, F_{FEA} : FEA force, ΔF : force percent difference

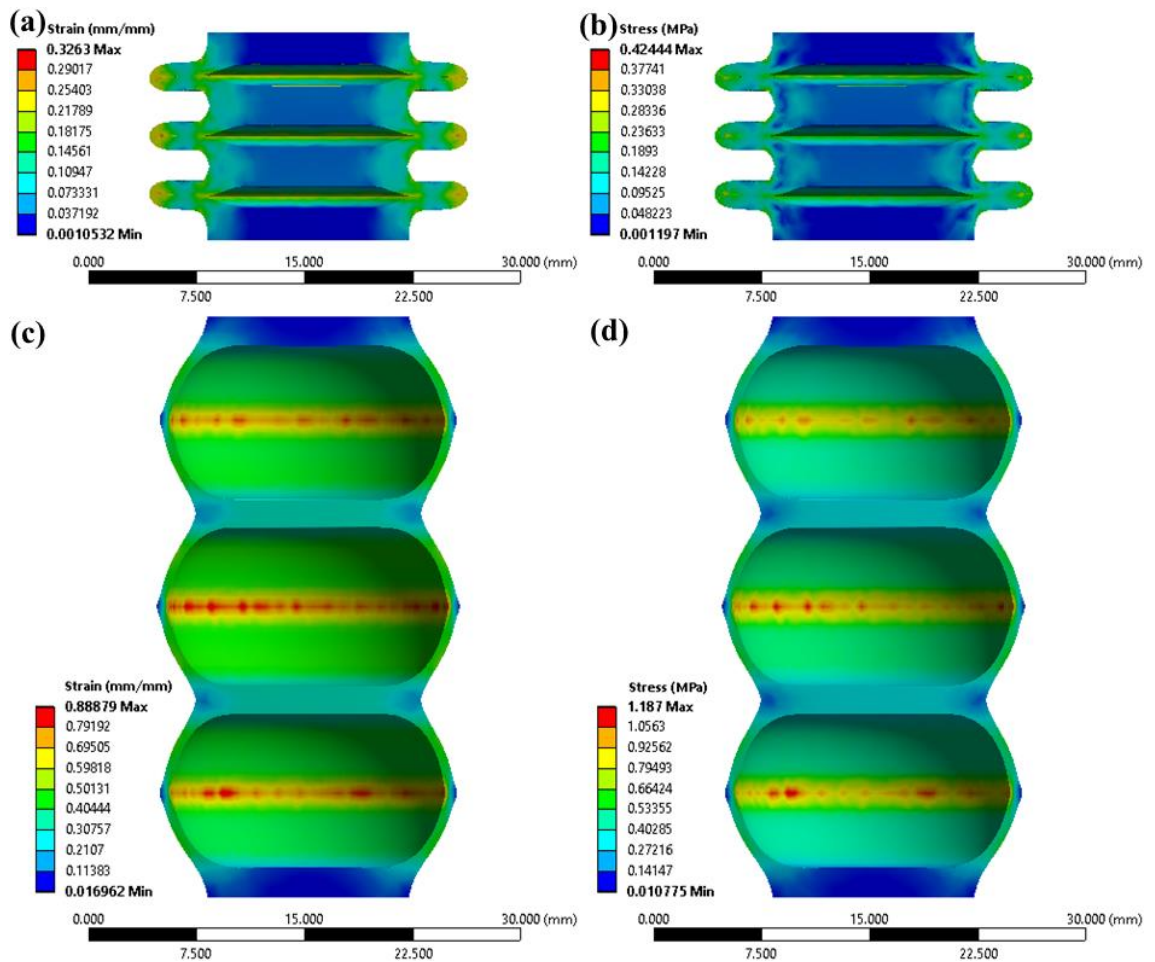


Figure 5.10 Finite element analysis results for a 3C 14 mm LSOMMA: (a) element strain at -25 kPa, (b) elemental stress at -25 kPa, (c) elemental strain at 75 kPa, and (d) elemental stress at 75 kPa.

5.5 Locomotion Robots

Pipe Crawler Robot

Robots which can traverse small pipes can be used for maintenance and inspections. A pipe crawling robot was constructed which could travel both horizontal and vertical pipes of roughly 30 mm diameter (Figure 5.11). The crawling robot was created using a central 3C 14 mm LSOMMA and two 1C 20 mm LSOMMAs attached at either end. The middle LSOMMA provided the bulk of the motion, whereas the front and rear LSOMMAs expanded outwards to grip the pipe wall while under vacuum pressure. These two actuators had their outer surfaces wrapped in PTFE tape to reduce the sliding friction against the pipe. The robot, with a total length of 61.5 mm, travels at horizontal and vertical velocities of 78.8 mm.min^{-1} and 73.2 mm.min^{-1} (Figure 5.12 (left)), respectively, using only a vacuum pressure source. When applying a sequence of both vacuum and gauge pressures to the central actuator, the horizontal and vertical speeds increased to $124.5 \text{ mm.min}^{-1}$ (Figure 5.11) and $145.9 \text{ mm.min}^{-1}$ (Figure 5.12 (right)), respectively, clearly demonstrating the benefits of utilising actuators capable of multi-mode operations. In terms of speed with respect to the robot's body length (BL), these equate to 2.02 BL.min^{-1} and 2.37 BL.min^{-1} , respectively. The pipe crawler can be made to reverse its direction simply by altering the inflation sequence. Its pipe crawling abilities were further demonstrated by having it journey through a 32 mm diameter pipe with a 90° bend from horizontal to vertical orientation (Figure A.1).

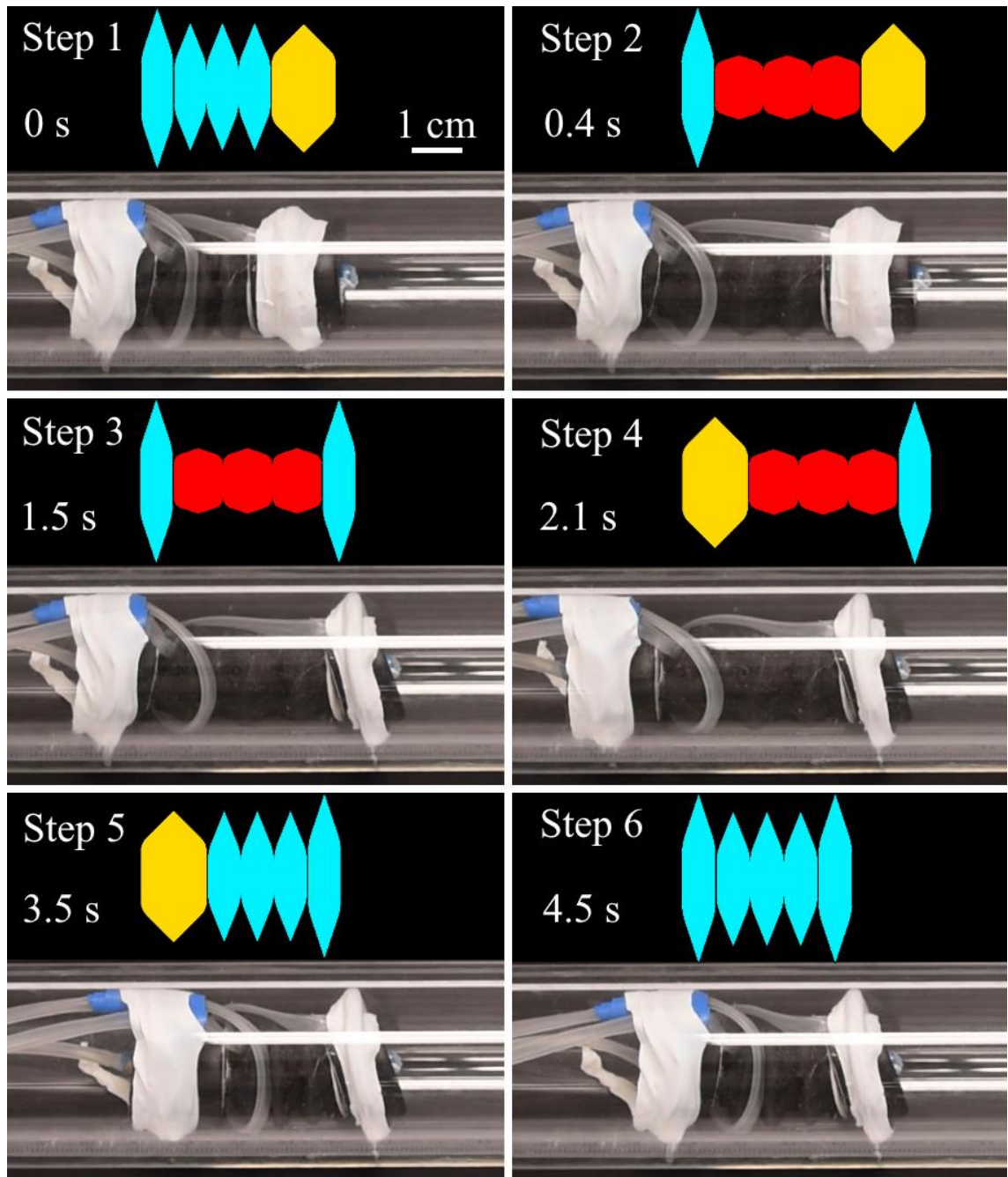


Figure 5.11 Pipe crawling robot with snapshots of individual steps. In the diagrams, aqua blue indicates a negative pressure (-20 kPa) actuated chamber, yellow an unactuated chamber, and red a positive pressure (50 kPa) actuated chamber.

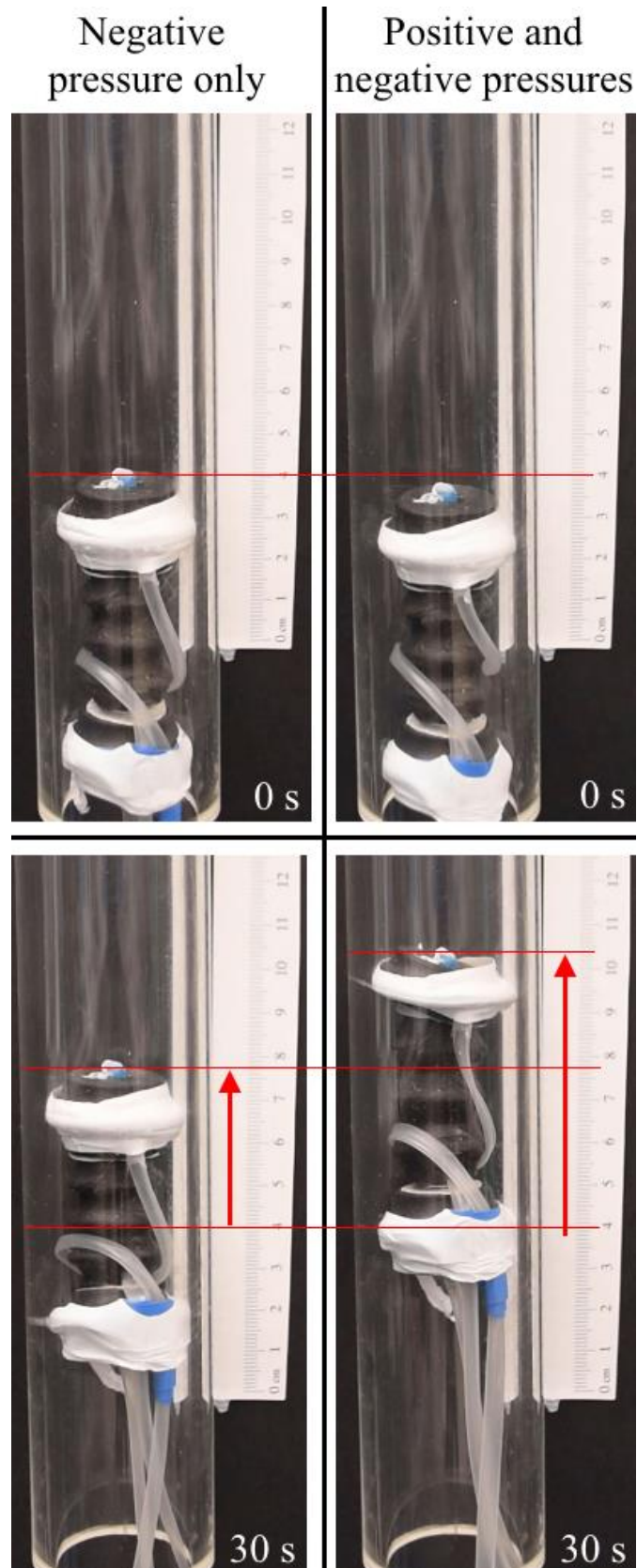


Figure 5.12 Pipe crawler moving vertically. Left: negative pressures (-20 kPa) only. Right: positive (50 kPa) and negative pressures. Upper: positions at 0 s. Lower: positions after 30 s.

Ground Locomotion Robots

The pipe crawling robot design was adapted into a general crawling robot to evaluate its locomotion abilities. Two 3C 14 mm LSOMMAs were placed in parallel, with structures attached between the ends for support. Feet were added to the front and rear ends of the LSOMMAs to improve traction with the surface. Small flaps of ElastAMBER rubber were attached to the plastic feet, allowing asymmetric slide-stick movements to alternate between the anchor points. The tethered locomotion robot weighed 14 g and had dimensions of 50 mm in length, 40 mm in width, and 25 mm in height. Utilising only a vacuum pressure source of -20 kPa, the robot travelled linearly at a velocity of $469 \text{ mm}\cdot\text{min}^{-1}$ ($9.38 \text{ BL}\cdot\text{min}^{-1}$) (Figure A.2 (a)) and turned at a rate of $172^\circ\cdot\text{min}^{-1}$ (Figure A.2 (b)). Upon applying positive pressures of 50 kPa in sequence with the vacuum pressures to the robot, these speeds increased to $652 \text{ mm}\cdot\text{min}^{-1}$ ($13.0 \text{ BL}\cdot\text{min}^{-1}$) walking (Figure 5.13 (a)), and $361^\circ\cdot\text{min}^{-1}$ turning (Figure 5.13 (b)) on the rubber mat surface. These substantial increases are due in part to the increased stroke length of contraction-extension movements compared to the contraction-rest cycle. Also contributing to the faster speeds are the strokes being actively driven in both directions, as opposed to the vacuum only version undergoing only active contractions with passive returns.

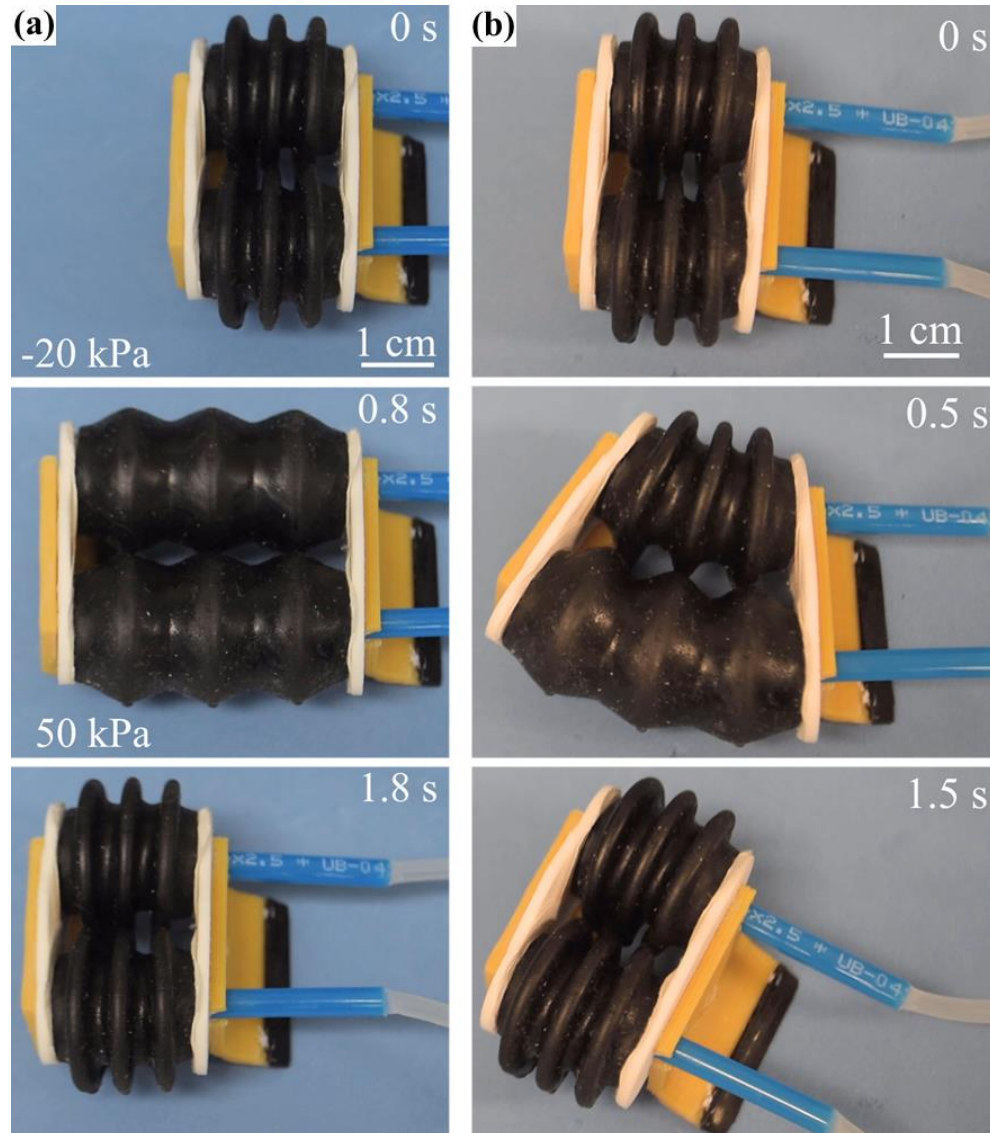


Figure 5.13 Soft pneumatic tethered locomotion robot, alternating between -20 kPa and 50 kPa (a) forward motion steps and (b) turning motion steps.

It is possible to create untethered robots that crawl autonomously using LSOMMA by using mini pneumatic solenoids and pumps. The control system was run by an Adafruit Trinket M0 microcontroller running a custom open-loop Arduino code. The digital outputs from the microcontroller were routed through solid state optical relays which toggled the pneumatic solenoid valves (Figure 5.14). The solenoid valves switched the pneumatic connections, shown in blue, connecting the actuators to either the pump or atmosphere. A 3.7 V lithium-ion polymer battery supplied the power for all components. The enclosure, which was 3D printed PLA made using a FDM printer, was made

oversized for the system to allow for easier assembly. Thus, there is room for more components to be added in the future, such as a pressure sensor for closed loop control, a wireless communication chipset, or a small camera. This was mounted to the rear of the locomotion robot and the rear foot was relocated to beneath the enclosure.

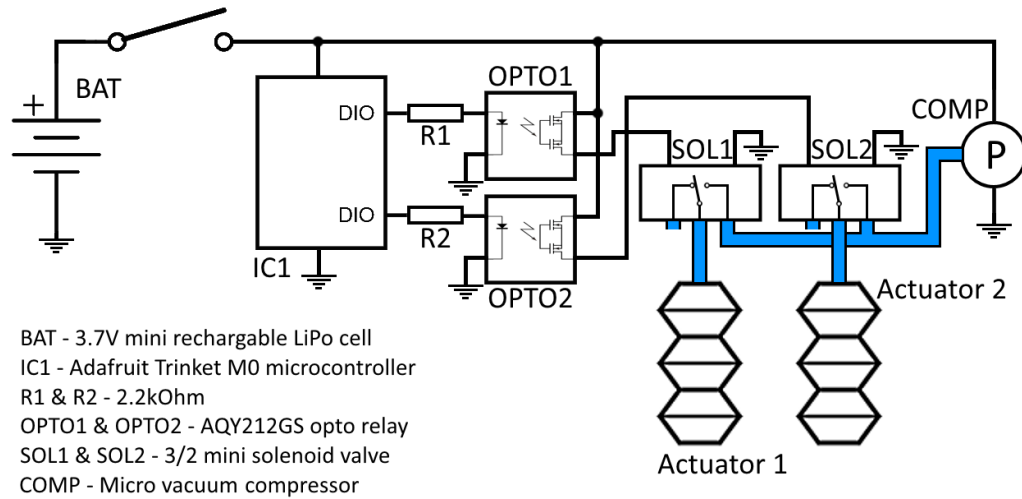


Figure 5.14 Untethered ground locomotion robot electrical and pneumatic schematic.

The performance of the untethered locomotion robot was distinctly lower than that of the tethered locomotion robot for two reasons. Firstly, the micro air pump was rated far lower in terms of vacuum pressure and flow rate compared to the tethered robot's pump. Second was the dramatic increase in mass because of the payload of mounted control components. The untethered locomotion robot weighed 95 g and had dimensions of 87 mm in length, 43 mm in width, and 36 mm in height. The untethered version operated under vacuum pressures only, as the inclusion of the components required to achieve positive pressure motion would severely increase the system's complexity, weight, and volume. When activated, the robot travelled linearly at a velocity of 423 mm.min⁻¹ (4.86 BL.min⁻¹) and could turn at a rate of 74.4 °.min⁻¹. It was able to traverse various surfaces such as a wooden desk, rubber foam mat, and office carpet (Figure 5.15).

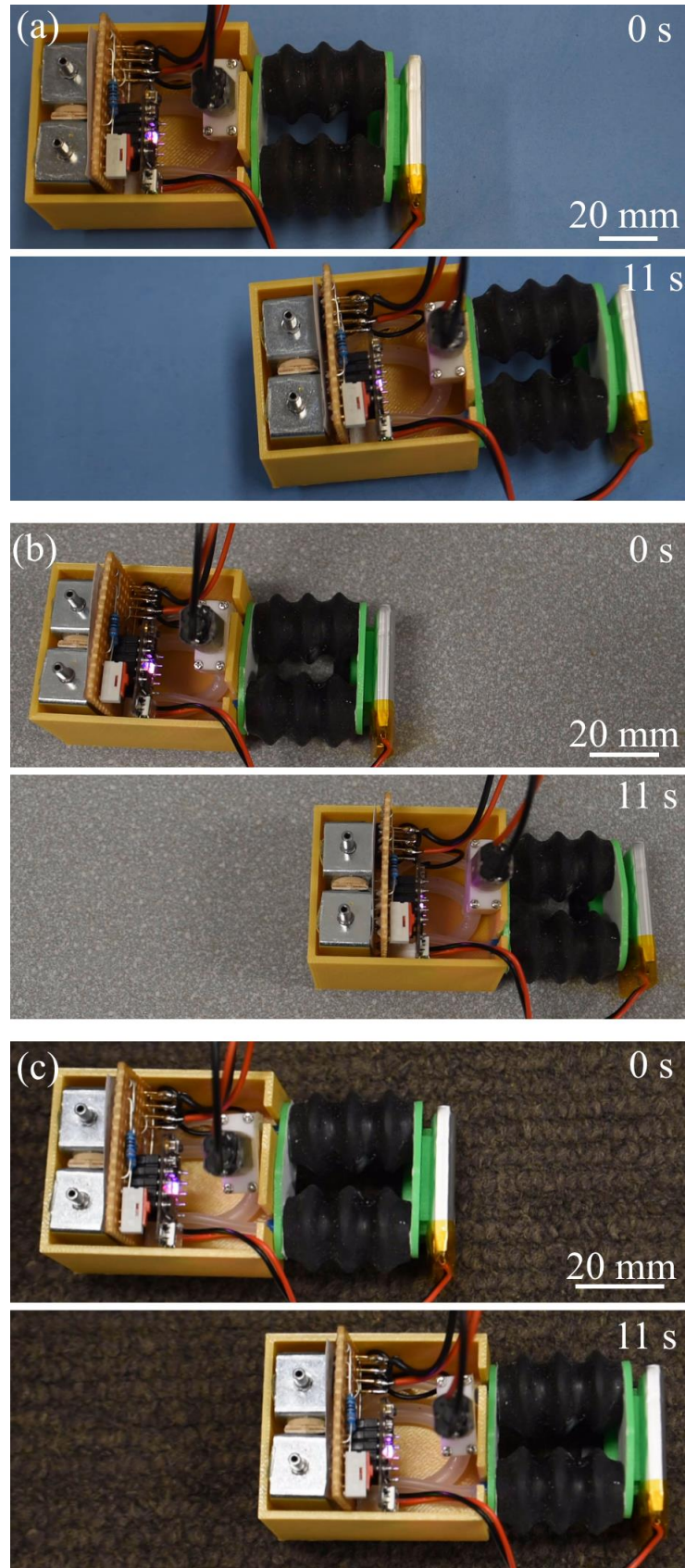


Figure 5.15 Untethered locomotion robot after six crawling cycles (11 seconds) on (a) a rubber mat, (b) wooden desk, and (c) office carpet.

5.6 Discussion

Fabrication

A challenge in creating the LSOMMA on a DLP printer arose from the interaction between the fabrication method and the actuator geometry. The soft linear bellows-like actuators are monolithic in structure and pneumatically actuated, and therefore utilise a singular pneumatic port. This fact, coupled with the clinging viscous nature of the resin and standard DLP printing procedures, introduced a complication. Typically, multiple vent holes are added to hollow rigid parts to allow for the uncured resin to drain from the interior and relieve the interior pressure imbalance. The limitation of a single hole necessitates specific print orientations and angles to achieve the draining and pressure relief. Further, it adds difficulty in the post-print cleaning of the part, especially for higher viscosity resins, as it cannot be continuously flushed with solvent like multi-port channels can [144]. More so, if the holes or voids are too small, the viscous resin may refuse to drain, rendering them useless and causing the print to fail. Fact that the suction forces which occur during the DLP printing process are proportional resin viscosity and layer surface area further necessitates the optimisation of viscosity and model orientation.

To simplify the evaluation and modelling, the actuators were approximated as first order systems. This assumed that the transient characteristics were not input-dependent and would scale according to the magnitude of the applied pressure. In actuality, the pressures supplied to the regulator inputs were fixed and would provide the same impulse upon the actuator regardless of the set point. The process variable was controlled by the regulator using high frequency switching of solenoid valves between the source pressure and the atmosphere. Experimentally, it was observed that the lower step inputs (lower pressure set points) had much quicker rise times and higher bandwidths than tests performed to higher input signals. This would not be true if the system were a true first order linear time-invariant system.

Actuator Performance

Compared to other soft linear vacuum actuators, LSOMMA devices show superior performance in many categories. The soft ElastAMBER material and LSOMMA geometry allows for greater contraction ratios than other devices, even when actuated with less than a quarter of the vacuum pressure [50, 92]. Additionally, the slowest LSOMMA actuator observed had a rise time three times faster than those reported by Yang *et al.* [50]. With its high cycle lifetimes of >10 000 cycles under positive pressures and >50 000 cycles under negative pressures, these actuators outlive many other similar devices. A different soft pneumatic actuator created using one of the few commercially available flexible DLP resins had an average failure lifetime of just nine cycles, up to a maximum of 50 cycles [55]. Similarly, a FDM printed PneuNet device reported an average lifetime of 606 cycles at 250 kPa [69]. In regards to the blocked forces, the pulling force of ~ 5.5 N generated by the 1C 20 mm LSOMMAs closely matched that of the shear-VAM, ~ 5.7 N, presented by Yang *et al.* [92], which was constructed from a material with a similar Young's modulus to ElastAMBER. This is in accordance with the relationship between force, pressure, and area, as the LSOMMA was roughly four times the area but operated at a quarter of the relative pressure [92].

A comparison between the performance of the LSOMMA actuators presented in this work with those of the predecessor LSOVA design [79] is summarised in Table 5.5. The previous work used a FDM 3D printer to fabricate low-cost linear soft actuators which operated under vacuum pressure. The material used was NinjaFlex, an off-the-shelf TPU filament with an elongation at yield of 65% and a tensile modulus of 12 MPa [98]. In this thesis the novel elastomeric resin ElastAMBER was used in modified mid-range DLP 3D printer to produce soft pneumatic actuators. The vacuum pressure required for contraction was reduced to roughly a quarter of the previous work, which reduced the system requirements and permitted new areas of application. Additionally, the elastomeric material made extension and pushing operations under gauge pressure possible. This enhancement has improved the potential

of the LSOMMA as an actuator by doubling the possible directions of motion and thus the operation modes.

Table 5.5 Comparison between the performance of LSOMMA and LSOVA.

Actuator	ΔP (kPa)	δ (mm)	F (N)	T_r (ms)	ω_b (rad.s ⁻¹)	L_t (cycles)
1C 20 mm LSOMMA	-25	-7.59	5.46	145	12.7	>50 000
	+75	5.09	19.4	252	15.4	8 132
1C 20 mm LSOVA	-97	-6.05	27.0	60	40.8	21 571

ΔP : operating gauge pressure, δ : linear displacement, F : blocked force, T_r : Rise Time, ω_b : estimated 3dB bandwidth, L_t : cycles before failure

These improvements, however, come with the consequence of some lowered performance metrics. The softer ElastAMBER material results in the LSOMMA absorbing more energy through structural deformation, resulting in lower blocking forces and slower response times, when compared to the stiffer polymer fabrication of the LSOVA. A substantial portion of the variance between the blocking forces of the two actuators is a result of the different pressures used in each experiment, as pneumatic force is proportional to applied pressure. The remainder is due to the ElastAMBER material absorbing some of the energy in the initial contraction stages. It is speculated the blocking force variance would reduce if the LSOMMA was operated at the same pressure. The lower temporal performances were most likely a consequence of the material's viscoelastic properties, with the strains being time delayed and non-instantaneous versus the applied stresses. The same is true for the lower bandwidths exhibited by the LSOMMA.

Considering these results, it is believed that the LSOMMA devices, having a similar geometry as the LSOVA design but using a soft elastomeric material, are an excellent addition to the literature on soft pneumatic actuators. The 1C 20 mm LSOMMA geometry used was identical to the LSOVA by Tawk *et al.* [79], allowing the direct comparison between the actuator types, while the

others were proportionally scaled. Thus, there is much room for the optimisation of the LSOMMA geometry to improve its performance metrics, especially under positive pressures which were not considered in the LSOVA design process. Rather than outright replacing LSOVAs, the presented multimode operable actuators can broaden the scope of their potential applications, offering more versatility, lower operating pressures, and simpler systems. Importantly, the lower operating pressures allowed for the use of smaller and lighter pumps, which expanded the possibilities for the creation of smaller devices and function in mobile operations.

The ElastAMBER material shows promise for creating intrinsically capacitive sensing actuators, displaying a strong correlation between actuator displacement and capacitance. The developed 3D printable ElastAMBER can find potential applications in sensors and actuators for many soft robotic and human-machine interface applications.

Soft Robotic Devices

The benefits of the softer, lighter material are evident through the direct comparison between similar sized LSOMMA and LSOVA pipe crawling robots. The ElastAMBER material allowed the LSOMMA robot to climb 25% faster under vacuum pressures alone. The speeds significantly improved with the addition of positive pressure actuation, achieving a 150% increase when operating using multiple modes [79]. The LSOMMA crawling robot also compares favourably to another recently published crawling robot, which requires eight individual actuators operating at vacuum pressures of -70 kPa to achieve movement [90]. This considerably larger robot (~235 mm long) could move along pipes with diameters of around 120 mm at horizontal and vertical speeds of 2.04 BL.min⁻¹ and 1.35 BL.min⁻¹, respectively.

The ground locomotion robot formed from just two LSOMMA units outperforms other walking robots, walking at speeds up to 652 mm.min⁻¹ (13.0 BL.min⁻¹) and turning at 361 °.min⁻¹. A soft walking robot capable of linear and rotational movements was presented by Jiao *et al.* [90]. The robot,

comprised of seven individual actuators operating under vacuum pressures of -70 kPa which were directed by five solenoid valves, had a length of 255 mm, and weighed 312 g. When moving along a rubber mat, it averaged a linear speed of $4.27 \text{ BL} \cdot \text{min}^{-1}$ and had a maximum turning speed of $25.7^\circ \cdot \text{s}^{-1}$ in a single direction, as its asymmetric design operated slower when rotating in the other direction. However, their robot was five greater in length, 22 times heavier, required five more actuators, and used a far greater vacuum pressure to operate when compared to the design presented here. This work also compares favourably to a slightly larger soft robot which achieved tethered locomotion using a bellows-like actuator and soft bistable valve [174]. This robot, powered by an air pressure supply of 17 kPa, could move linearly at a rate of $84 \text{ mm} \cdot \text{min}^{-1}$. Compared to other soft robots which also utilise two-anchor crawling mechanisms, this work's design performs far above the average ($9.0 \text{ BL} \cdot \text{min}^{-1}$) [23].

The untethered locomotion robot is contrasted to other similarly sized untethered soft pneumatic crawling robots and summarised in Table 5.6. This soft robot had the second fastest speed relative to body length, outperformed due to the first-place robot being built taller than it was long and was restricted to smooth level surfaces [37]. In terms of turning speed, it outperformed all other robots of a similar size, bested only by a robot with a mass over twenty times greater. Additionally, its operation uses the lowest vacuum pressure and the second lowest pressure magnitude overall, while having the second lowest mass.

Table 5.6 Comparison of untethered soft pneumatic crawling robots

Crawling Robots	ΔP (kPa)	m (g)	L (mm)	v (BL.min ⁻¹)	ω (°.min ⁻¹)
This work	-20	95	87	4.86	74.4
Duggan <i>et al.</i> [175]	16	200	210	0.08	8
Rafsanjani <i>et al.</i> [91]	16	65	275	1.43	-
Yang <i>et al.</i> [37]	-35	N/A	50	6.28	-
Waynelovich <i>et al.</i> [176]	90	2 000	N/A	0.056	103.9
Tolley <i>et al.</i> [177]	138	5 000	650	0.462	11.7

ΔP : operating gauge pressure, m : mass of the untethered robot, L : body length of the untethered robot in the direction of travel, v : linear velocity proportional to body length, ω : angular velocity

6 CONCLUSIONS AND RECOMMENDATIONS FOR FUTURE WORK

This thesis provided advancements to both materials technologies and actuator designs, allowing further developments in the field of soft pneumatic actuators. DLP 3D printing fabrication was improved through the synthesis of a new elastomeric material, ElastAMBER. This soft stretchable material was characterised in terms of resin viscosity, mechanical, and thermal behaviours. Then, a new linear soft pneumatic actuator, the LSOMMA, was created and analysed. This multi-mode actuator could produce sophisticated linear motions as both contractions and expansions. It showed demonstrable improvements over previously developed soft locomotion robotic devices.

6.1 Conclusions

This work presented a new photopolymerisable resin with a viscosity of 1 000 mPa.s at 40 °C that was capable of producing high fidelity elastomeric components on a DLP 3D printer. ElastAMBER's mechanical properties were evaluated thoroughly, exhibiting a significant extension ratio of 4.02, a Young's modulus of 0.579 MPa, and an ultimate tensile strength of 1.23 MPa. The cross-linking density of ElastAMBER was calculated through the Flory-Rehner and Neo-Hookean methods, producing values of 78.7 mol.m⁻³ and 79.6 mol.m⁻³, respectively, demonstrating the high elasticity and flexibility of the components made from ElastAMBER. The printing of this material was enhanced by modifications made to the DLP printer.

A soft actuator was printed and its change in capacitance was evaluated over the full actuation cycle. The device was used as a dual actuating-sensing device, showing a strong correlation between the pressure within the actuator and the change in capacitance across it. It is expected this elastomer will be of great use for the 3D printing of novel soft pneumatic actuators, especially in applications where intrinsic sensing capabilities are desirable, such as soft actuators, soft robotic devices, and human-machine interfaces.

The LSOMMA was presented as an advancement in soft pneumatic actuator technologies. The production of these actuators was made possible by the creation and use of the ElastAMBER material. Soft pneumatic actuators with the ability to actively produce strains in multiple directions were rarely found in literature, despite the obvious benefits of actively generating both pushing and pulling forces using a single actuator. LSOMMAs have been demonstrated to achieving meaningful strains at lower pressures than many other pneumatic devices [13, 37, 67, 90, 176, 177]. By using a DLP printer to manufacture the actuators, their walls formed fully three-dimensional elastomeric chains, creating completely airtight chambers that could survive tens of thousands of cycles without creep before failure.

Through the construction and analysis of two small mobile robots, the applicability of LSOMMAs in the field of soft robotics was shown, emphasising the benefits of multi-modal operations. A peristaltic pipe crawler was able to rapidly move horizontally, vertically, around bends, and adapt to changes in pipe diameter. Ground-based crawling robots were assembled to show how LSOMMAs can be used for unconstrained locomotion, including the ability to turn. Importantly, the low operating pressures of LSOMMAs permitted the use of smaller, lighter pumps and other control components, allowing for the creation of lightweight mobile devices. An untethered version of the ground locomotion robot was able to traverse multiple surface materials, including difficult ones like carpet. Notably, both the tethered and untethered versions performed significantly better in many categories compared to many of the other soft robots of similar natures within the literature.

6.2 Recommendations for Future Research

There is potential for further refining the ElastAMBER formula for optimal performance:

- The 5:3:2 ratio of BR-345 to IBOA to HEA was selected as a compromise between resin viscosity, material elongation at break, and hysteresis effects. For applications prioritising elongation at break, a larger ratio of

BR-345 or IBOA could be used. If it were desirable to further reduce the hysteresis losses, then a proportionally greater HEA concentration would be beneficial.

- Only two types of pigments were evaluated, though colourless photoabsorbers or fluorescing optical brighteners are options for creating a transparent ElastAMBER polymer for optical functions.
- The post-curing time was not investigated for its effects on material properties but is known to have positive effects, up to a certain point.
- ElastAMBER could potentially improve the performance of other soft pneumatic actuators, improving their maximum strains and lowering their operating pressures.
- Further studies could perform deeper investigations regarding control schemes utilising capacitance measurement as a means for actuator control.

There is considerable room for the optimisation of LSOMMAs geometry in terms of performance under both pressure types:

- This is especially true for positive pressures, as these were not considered in the design of the original LSOVA. As the LSOMMAs evaluated in this work used similar geometries to the LSOVA to allow direct comparisons, no consideration was given to designing for extension motions.
- The wall thickness of soft pneumatic actuators, an important factor in internal material stresses and flexibility, was not directly assessed in this work.
 - Related to this is the production and evaluation of smaller scale LSOMMAs on high resolution DLP 3D printers.
 - DLP technologies have a much higher theoretical resolution than FDM printers and can create microfluidic devices. Therefore, it would be beneficial to determine the smallest size at which a LSOMMA can be constructed and operated.

The soft locomotion robots could be improved in several ways:

- The implementation of more robust control systems and feedback loops.
 - The untethered ground walker operated under open-loop control and the parameters were not adjusted for better performance across the different terrains.
 - The pressure control was mostly automated by the regulators' internal systems, which used their own PID controllers to set the pressures. A level of user control was maintained by controlling the input to the regulators.
- An untethered version of the pipe crawler could be constructed and evaluated.
 - The integration of a mechanism to allow the flow of fluids past the pipe crawler, such as a mesh or struts, would aid its operation in live pipelines.
- Smaller and lighter components could be sourced and integrated into the untethered robots.
- The integration of a mini camera and a more robust control system would help guide the untethered robots autonomously in multiple environments for operations such as exploration, inspection and monitoring, and search and rescue.
 - Alternatively, a camera and a wireless communication module could allow for the remote observation and control of the untethered devices.
- The LSOMMA could be integrated into other soft robotic devices or used in place of other linear actuators.

REFERENCES

- [1] H. Janocha, *Actuators: Basics and Applications*: Springer, 2004.
- [2] S. M. Mirvakili and I. W. Hunter, "Artificial Muscles: Mechanisms, Applications, and Challenges," *Advanced Materials*, vol. 30, p. 1704407, 2018/02/01 2018.
- [3] A. Hošovský, J. Piteľ, K. Židek, M. Tóthová, J. Sárosi, and L. Cveticanin, "Dynamic characterization and simulation of two-link soft robot arm with pneumatic muscles," *Mechanism and Machine Theory*, vol. 103, pp. 98-116, 2016.
- [4] P. Šmeringai, M. Rimár, M. Fedák, and Š. Kuna, "Real Time pressure control in pneumatic actuators," in *Key Engineering Materials* vol. 669, ed: Trans Tech Publications Ltd, 2016, pp. 335-344.
- [5] L. Hines, K. Petersen, G. Z. Lum, and M. Sitti, "Soft Actuators for Small-Scale Robotics," *Advanced Materials*, 2016.
- [6] K. H. Cho, M. G. Song, H. Jung, S. Y. Yang, H. Rodrigue, H. Moon, *et al.*, "Biomimetic robotic joint mechanism driven by soft linear actuators," 2017, pp. 1850-1855.
- [7] G. Alici, "Softer is Harder: What Differentiates Soft Robotics from Hard Robotics?," *MRS Advances*, vol. 3, pp. 1557-1568, 2018/06/01 2018.
- [8] E. Sachyani Keneth, A. Kamyshny, M. Totaro, L. Beccai, and S. Magdassi, "3D Printing Materials for Soft Robotics," *Advanced Materials*, vol. 33, p. 2003387, 2021/05/01 2021.
- [9] J. Hughes, U. Culha, F. Giardina, F. Guenther, A. Rosendo, and F. Iida, "Soft Manipulators and Grippers: A Review," *Frontiers in Robotics and AI*, vol. 3, Nov 16 2016.
- [10] J. H. Low, H. A. Marcelo, and C. H. Yeow, "Customizable Soft Pneumatic Finger Actuators for Hand Orthotic and Prosthetic Applications," in *Proceedings of the Ieee/Ras-Embs International Conference on Rehabilitation Robotics*, New York, 2015, pp. 380-385.
- [11] A. De Greef, P. Lambert, and A. Delchambre, "Towards flexible medical instruments: Review of flexible fluidic actuators," *Precision Engineering*, vol. 33, pp. 311-321, 2009.
- [12] P. Polygerinos, N. Correll, S. A. Morin, B. Mosadegh, C. D. Onal, K. Petersen, *et al.*, "Soft Robotics: Review of Fluid-Driven Intrinsically Soft Devices; Manufacturing, Sensing, Control, and Applications in Human-Robot Interaction," *Advanced Engineering Materials*, vol. 19, 2017.
- [13] K. Han, N. H. Kim, and D. Shin, "A Novel Soft Pneumatic Artificial Muscle with High-Contraction Ratio," *Soft Robotics*, vol. 5, pp. 554-566, 2018.
- [14] D. Rus and M. T. Tolley, "Design, fabrication and control of soft robots," *Nature*, vol. 521, pp. 467-475, 2015/05/01 2015.
- [15] U. Çulha and F. Iida, "Enhancement of finger motion range with compliant anthropomorphic joint design," *Bioinspiration and Biomimetics*, vol. 11, 2016.

- [16] D. Han, C. Farino, C. Yang, T. Scott, D. Browe, W. Choi, *et al.*, "Soft Robotic Manipulation and Locomotion with a 3D Printed Electroactive Hydrogel," *ACS Applied Materials and Interfaces*, 2018.
- [17] S. Schmitt, D. F. B. Haeufle, R. Blickhan, and M. Günther, "Nature as an engineer: One simple concept of a bio-inspired functional artificial muscle," *Bioinspiration and Biomimetics*, vol. 7, 2012.
- [18] R. J. Lock, S. C. Burgess, and R. Vaidyanathan, "Multi-modal locomotion: From animal to application," *Bioinspiration and Biomimetics*, vol. 9, 2014.
- [19] Y. Bar-Cohen, "Biomimetics - Using nature to inspire human innovation," *Bioinspiration and Biomimetics*, vol. 1, pp. P1-P12, 2006.
- [20] J. K. Hopkins, B. W. Spranklin, and S. K. Gupta, "A survey of snake-inspired robot designs," *Bioinspiration and Biomimetics*, vol. 4, 2009.
- [21] M. Luo, Y. Pan, E. H. Skorina, W. Tao, F. Chen, S. Ozel, *et al.*, "Slithering towards autonomy: A self-contained soft robotic snake platform with integrated curvature sensing," *Bioinspiration and Biomimetics*, vol. 10, 2015.
- [22] S. Kim, C. Laschi, and B. Trimmer, "Soft robotics: A bioinspired evolution in robotics," *Trends in Biotechnology*, vol. 31, pp. 287-294, 2013.
- [23] M. Calisti, G. Picardi, and C. Laschi, "Fundamentals of soft robot locomotion," *Journal of the Royal Society Interface*, vol. 14, 2017.
- [24] R. Bogue, "Artificial muscles and soft gripping: A review of technologies and applications," *Industrial Robot*, vol. 39, pp. 535-540, 2012.
- [25] A. W. Feinberg, "Biological Soft Robotics," in *Annual Review of Biomedical Engineering* vol. 17, ed: Annual Reviews Inc., 2015, pp. 243-265.
- [26] S. Landkammer, R. Valek, and R. Hornfeck, "A novel bio-inspired fluidic actuator for robotic applications," in *25th International Conference on Adaptive Structures and Technologies, ICAST 2014*, 2014.
- [27] S. Landkammer, F. Winter, D. Schneider, and R. Hornfeck, "Biomimetic Spider Leg Joints: A Review from Biomechanical Research to Compliant Robotic Actuators," *Robotics*, vol. 5, p. 15, Sep 2016.
- [28] M. Calisti, M. Giorelli, G. Levy, B. Mazzolai, B. Hochner, C. Laschi, *et al.*, "An octopus-bioinspired solution to movement and manipulation for soft robots," *Bioinspiration and Biomimetics*, vol. 6, 2011.
- [29] C. Laschi, B. Mazzolai, V. Mattoli, M. Cianchetti, and P. Dario, "Design of a biomimetic robotic octopus arm," *Bioinspiration and Biomimetics*, vol. 4, 2009.
- [30] R. Balasubramanian and V. J. Santos, "The human hand as an inspiration for robot hand development," in *Springer Tracts in Advanced Robotics* vol. 95, ed: Springer Verlag, 2014.
- [31] P. F. Egan, J. Cagan, C. Schunn, and P. R. LeDuc, "Design of Complex Biologically Based Nanoscale Systems Using Multi-Agent Simulations and Structure-Behavior-Function Representations," *Journal of Mechanical Design*, vol. 135, pp. 061005-061005-12, 2013.
- [32] J. E. Huber, N. A. Fleck, and M. F. Ashby, "The selection of mechanical actuators based on performance indices," *Proceedings of the Royal Society*

- A: Mathematical, Physical and Engineering Sciences*, vol. 453, pp. 2185-2205, 1997.
- [33] J. Mohd Jani, M. Leary, A. Subic, and M. A. Gibson, "A review of shape memory alloy research, applications and opportunities," *Materials and Design*, vol. 56, pp. 1078-1113, 2014.
 - [34] J. I. Lipton, S. Angle, R. E. Banai, E. Peretz, and H. Lipson, "Electrically Actuated Hydraulic Solids," *Advanced Engineering Materials*, 2016.
 - [35] C. Semini, V. Barasuol, J. Goldsmith, M. Frigerio, M. Focchi, Y. Gao, *et al.*, "Design of the Hydraulically Actuated, Torque-Controlled Quadruped Robot HyQ2Max," *IEEE/ASME Transactions on Mechatronics*, vol. 22, pp. 635-646, 2017.
 - [36] M. De Volder, A. J. M. Moers, and D. Reynaerts, "Fabrication and control of miniature McKibben actuators," *Sensors and Actuators, A: Physical*, vol. 166, pp. 111-116, 2011.
 - [37] D. Yang, B. Mosadegh, A. Ainla, B. Lee, F. Khashai, Z. Suo, *et al.*, "Buckling of Elastomeric Beams Enables Actuation of Soft Machines," *Advanced Materials*, vol. 27, pp. 6323-6327, 2015.
 - [38] P. Heo, G. M. Gu, S. Lee, K. Rhee, and J. Kim, "Current hand exoskeleton technologies for rehabilitation and assistive engineering," *International Journal of Precision Engineering and Manufacturing*, vol. 13, pp. 807-824, 2012.
 - [39] A. Zolfagharian, A. Z. Kouzani, S. Y. Khoo, A. A. A. Moghadam, I. Gibson, and A. Kaynak, "Evolution of 3D printed soft actuators," *Sensors and Actuators, A: Physical*, vol. 250, pp. 258-272, 2016.
 - [40] K. Andrianesis and A. Tzes, "Development and Control of a Multifunctional Prosthetic Hand with Shape Memory Alloy Actuators," *Journal of Intelligent and Robotic Systems: Theory and Applications*, vol. 78, pp. 257-289, 2015.
 - [41] K. Kluszczyński and M. Kciuk, "SMA actuators: Theory, performance curves and design problems," *COMPEL - The International Journal for Computation and Mathematics in Electrical and Electronic Engineering*, vol. 32, pp. 1417-1427, 2013.
 - [42] F. Gao, H. Deng, and Y. Zhang, "Hybrid actuator combining shape memory alloy with DC motor for prosthetic fingers," *Sensors and Actuators, A: Physical*, vol. 223, pp. 40-48, 2015.
 - [43] F. Simone, A. York, and S. Seelecke, "Design and fabrication of a three-finger prosthetic hand using SMA muscle wires," in *Bioinspiration, Biomimetics, and Bioreplication 2015*, 2015.
 - [44] F. Carpi, R. Kornbluh, P. Sommer-Larsen, and G. Alici, "Electroactive polymer actuators as artificial muscles: Are they ready for bioinspired applications?," *Bioinspiration and Biomimetics*, vol. 6, 2011.
 - [45] Y. Bar-Cohen, "Electroactive Polymer (EAP) actuators for future humanlike robots," in *Electroactive Polymer Actuators and Devices (EAPAD) 2009*, San Diego, CA, 2009.

- [46] D. Trivedi, C. D. Rahn, W. M. Kier, and I. D. Walker, "Soft robotics: Biological inspiration, state of the art, and future research," *Applied Bionics and Biomechanics*, vol. 5, pp. 99-117, 2008.
- [47] R. Mutlu, G. Alici, M. In het Panhuis, and G. M. Spinks, "3D Printed Flexure Hinges for Soft Monolithic Prosthetic Fingers," *Soft Robotics*, vol. 3, pp. 120-133, 2016.
- [48] PI-Ceramic. (2017, 20/06/2017). *Properties of Piezo Actuators*. Available: <https://www.piceramic.com/en/piezo-technology/properties-piezo-actuators/>
- [49] M. C. Carrozza, G. Cappiello, S. Micera, B. B. Edin, L. Beccai, and C. Cipriani, "Design of a cybernetic hand for perception and action," *Biological Cybernetics*, vol. 95, pp. 629-644, 2006.
- [50] D. Yang, M. S. Verma, J.-H. So, B. Mosadegh, C. Keplinger, B. Lee, *et al.*, "Buckling Pneumatic Linear Actuators Inspired by Muscle," *Advanced Materials Technologies*, vol. 1, pp. n/a-n/a, 2016.
- [51] M. A. Robertson and J. Paik, "Low-inertia vacuum-powered soft pneumatic actuator coil characterization and design methodology," 2018, pp. 431-436.
- [52] F. Daerden and D. Lefeber, "Pneumatic artificial muscles: Actuators for robotics and automation," *European Journal of Mechanical and Environmental Engineering*, vol. 47, pp. 11-21, 2002.
- [53] M. Kutz, *Standard handbook of biomedical engineering and design / Myer Kutz, editor in chief*: New York : McGraw-Hill, c2003., 2003.
- [54] W. Hu, R. Mutlu, W. Li, and G. Alici, "A structural optimisation method for a soft pneumatic actuator," *Robotics*, vol. 7, 2018.
- [55] B. N. Peele, T. J. Wallin, H. Zhao, and R. F. Shepherd, "3D printing antagonistic systems of artificial muscle using projection stereolithography," *Bioinspiration and Biomimetics*, vol. 10, 2015.
- [56] E. W. Hawkes, D. L. Christensen, and A. M. Okamura, "Design and implementation of a 300% strain soft artificial muscle," 2016, pp. 4022-4029.
- [57] M. Wehner, M. T. Tolley, Y. Mengüç, Y. L. Park, A. Mozeika, Y. Ding, *et al.*, "Pneumatic Energy Sources for Autonomous and Wearable Soft Robotics," *Soft Robotics*, vol. 1, pp. 263-274, 2014.
- [58] D. X. Ba, T. Q. Dinh, and K. K. Ahn, "An Integrated Intelligent Nonlinear Control Method for a Pneumatic Artificial Muscle," *IEEE/ASME Transactions on Mechatronics*, vol. 21, pp. 1835-1845, 2016.
- [59] G. Andrikopoulos, G. Nikolakopoulos, and S. Manesis, "A Survey on applications of Pneumatic Artificial Muscles," in *2011 19th Mediterranean Conference on Control and Automation, MED 2011, Corfu, 2011*, pp. 1439-1446.
- [60] J. Mižáková, J. Pitel, and M. Tóthová, "Pneumatic artificial muscle as actuator in mechatronic system," in *Applied Mechanics and Materials* vol. 460, ed: Trans Tech Publications Ltd, 2014, pp. 81-90.
- [61] Festo Corporation. (2016, 2016-09-28). *Fluidic Muscle DMSP/MAS*. Available:

https://www.festo.com/cat/en_us/data/doc_enus/PDF/US/DMSP-MAS_ENUS.PDF

- [62] D. Buchler, H. Ott, and J. Peters, "A lightweight robotic arm with pneumatic muscles for robot learning," in *2016 IEEE International Conference on Robotics and Automation, ICRA 2016*, 2016, pp. 4086-4092.
- [63] A. A. M. Faudzi, M. R. M. Razif, I. N. A. M. Nordin, K. Suzumori, S. Wakimoto, and D. Hirooka, "Development of bending soft actuator with different braided angles," in *2012 IEEE/ASME International Conference on Advanced Intelligent Mechatronics, AIM 2012*, Kaohsiung, 2012, pp. 1093-1098.
- [64] B. K. S. Woods, S. M. Boyer, E. G. Hocking, N. M. Wereley, and C. S. Kothera, "Contractile pneumatic artificial muscle configured to generate extension," *Journal of Dynamic Systems, Measurement and Control, Transactions of the ASME*, vol. 136, 2014.
- [65] T. Sato, N. Saito, T. Ogasawara, and T. Sato, "Development of rubberless artificial muscle and fundamental characteristics," in *37th Annual Conference of the IEEE Industrial Electronics Society, IECON 2011*, Melbourne, VIC, 2011, pp. 2124-2129.
- [66] J. Yan, B. Xu, X. Zhang, and J. Zhao, "Design and test of a new spiral driven pure torsional soft actuator," vol. 10462 LNAI, H. Liu, Y. Huang, H. Wu, and Z. Yin, Eds., ed: Springer Verlag, 2017, pp. 127-139.
- [67] R. Deimel and O. Brock, "A compliant hand based on a novel pneumatic actuator," in *2013 IEEE International Conference on Robotics and Automation, ICRA 2013*, Karlsruhe, 2013, pp. 2047-2053.
- [68] B. Mosadegh, P. Polygerinos, C. Keplinger, S. Wennstedt, R. F. Shepherd, U. Gupta, *et al.*, "Pneumatic networks for soft robotics that actuate rapidly," *Advanced Functional Materials*, vol. 24, pp. 2163-2170, 2014.
- [69] H. K. Yap, H. Y. Ng, and C. H. Yeow, "High-Force Soft Printable Pneumatics for Soft Robotic Applications," *Soft Robotics*, vol. 3, pp. 144-158, 2016.
- [70] P. Polygerinos, S. Lyne, Z. Wang, L. F. Nicolini, B. Mosadegh, G. M. Whitesides, *et al.*, "Towards a soft pneumatic glove for hand rehabilitation," in *2013 26th IEEE/RSJ International Conference on Intelligent Robots and Systems: New Horizon, IROS 2013*, Tokyo, 2013, pp. 1512-1517.
- [71] F. Ilievski, A. D. Mazzeo, R. F. Shepherd, X. Chen, and G. M. Whitesides, "Soft robotics for chemists," *Angewandte Chemie - International Edition*, vol. 50, pp. 1890-1895, 2011.
- [72] R. Deimel and O. Brock, "A novel type of compliant and underactuated robotic hand for dexterous grasping," *International Journal of Robotics Research*, vol. 35, pp. 161-185, 2016.
- [73] S. Wakimoto, K. Ogura, K. Suzumori, and Y. Nishioka, "Miniature soft hand with curling rubber pneumatic actuators," in *2009 IEEE International Conference on Robotics and Automation, ICRA '09*, Kobe, 2009, pp. 556-561.
- [74] J. Morrow, H. S. Shin, C. Phillips-Grafflin, S. H. Jang, J. Torrey, R. Larkins, *et al.*, "Improving Soft Pneumatic Actuator fingers through

- integration of soft sensors, position and force control, and rigid fingernails," in *2016 IEEE International Conference on Robotics and Automation, ICRA 2016*, 2016, pp. 5024-5031.
- [75] D. Mata Amritanandamayi, G. Udupa, and P. Sreedharan, "A novel underactuated multi-fingered soft robotic hand for prosthetic application," *Robotics and Autonomous Systems*, vol. 100, pp. 267-277, 2018.
 - [76] R. F. Shepherd, F. Ilievski, W. Choi, S. A. Morin, A. A. Stokes, A. D. Mazzeo, *et al.*, "Multigait soft robot," *Proceedings of the National Academy of Sciences of the United States of America*, vol. 108, pp. 20400-20403, 2011.
 - [77] S. Park, K. Mondal, R. M. Treadway, V. Kumar, S. Ma, J. D. Holbery, *et al.*, "Silicones for Stretchable and Durable Soft Devices: Beyond Sylgard-184," *ACS Applied Materials and Interfaces*, vol. 10, pp. 11261-11268, 2018.
 - [78] M. Wehner, R. L. Truby, D. J. Fitzgerald, B. Mosadegh, G. M. Whitesides, J. A. Lewis, *et al.*, "An integrated design and fabrication strategy for entirely soft, autonomous robots," *Nature*, vol. 536, pp. 451-455, 2016.
 - [79] C. Tawak, G. Spinks, M. in het Panhuis, and G. Alici, "3D Printable Linear Soft Vacuum Actuators (LSOVA): their modeling, performance quantification and application in soft robotic systems," *IEEE/ASME Transactions on Mechatronics*, pp. 1-1, 2019.
 - [80] Recreus, "Filaflex 60A 'Pro' Technical Data Sheet," 2018.
 - [81] H. Hingorani, Y. F. Zhang, B. Zhang, A. Serjouei, and Q. Ge, "Modified commercial UV curable elastomers for passive 4D printing," *International Journal of Smart and Nano Materials*, vol. 10, pp. 225-236, 2019.
 - [82] D. K. Patel, A. H. Sakhaei, M. Layani, B. Zhang, Q. Ge, and S. Magdassi, "Highly Stretchable and UV Curable Elastomers for Digital Light Processing Based 3D Printing," *Advanced Materials*, 2017.
 - [83] C. J. Thrasher, J. J. Schwartz, and A. J. Boydston, "Modular Elastomer Photoresins for Digital Light Processing Additive Manufacturing," *ACS Applied Materials and Interfaces*, vol. 9, pp. 39708-39716, 2017.
 - [84] Y. F. Zhang, C. J. X. Ng, Z. Chen, W. Zhang, S. Panjwani, K. Kowsari, *et al.*, "Miniature Pneumatic Actuators for Soft Robots by High-Resolution Multimaterial 3D Printing," *Advanced Materials Technologies*, vol. 4, 2019.
 - [85] K. Suzumori, A. Koga, and R. Haneda, "Microfabrication of integrated FMAs using stereo lithography," pp. 136-141, 1994.
 - [86] S. Sanan, P. S. Lynn, and S. T. Griffith, "Pneumatic torsional actuators for inflatable robots," *Journal of Mechanisms and Robotics*, vol. 6, 2014.
 - [87] D. Baiden, A. Wilkening, and O. Ivlev, "Safety and handling concept for assistive robotic devices with pneumatic rotary soft-actuators," in *2011 IEEE/ASME International Conference on Advanced Intelligent Mechatronics, AIM 2011*, Budapest, 2011, pp. 754-759.
 - [88] H. Amase, Y. Nishioka, and T. Yasuda, "Mechanism and basic characteristics of a helical inflatable gripper," in *12th IEEE International Conference on Mechatronics and Automation, ICMA 2015*, 2015, pp. 2559-2564.
 - [89] Y. Nishioka, M. Uesu, H. Tsuboi, and S. Kawamura, "Proposal of an extremely lightweight soft actuator using plastic films with a pleated

- structure," in *2012 19th International Conference on Mechatronics and Machine Vision in Practice, M2VIP 2012*, Auckland, 2012, pp. 474-479.
- [90] Z. Jiao, C. Ji, J. Zou, H. Yang, and M. Pan, "Vacuum-Powered Soft Pneumatic Twisting Actuators to Empower New Capabilities for Soft Robots," *Advanced Materials Technologies*, vol. 4, 2019.
 - [91] A. Rafsanjani, Y. Zhang, B. Liu, S. M. Rubinstein, and K. Bertoldi, "Kirigami skins make a simple soft actuator crawl," *Science Robotics*, vol. 3, p. eaar7555, 2018.
 - [92] D. Yang, M. S. Verma, E. Lossner, D. Stothers, and G. M. Whitesides, "Negative-Pressure Soft Linear Actuator with a Mechanical Advantage," *Advanced Materials Technologies*, vol. 2, 2017.
 - [93] A. J. Veale, S. Q. Xie, and I. A. Anderson, "Characterizing the Peano fluidic muscle and the effects of its geometry properties on its behavior," *Smart Materials and Structures*, vol. 25, 2016.
 - [94] A. J. Veale, I. A. Anderson, and S. Q. Xie, "The smart Peano fluidic muscle: A low profile flexible orthosis actuator that feels pain," in *Sensors and Smart Structures Technologies for Civil, Mechanical, and Aerospace Systems 2015*, 2015.
 - [95] M. Heidingsfeld, R. Horio, B. Baesch, C. Riethmüller, G. T. Gresser, and O. Sawodny, "Introduction, mathematical modelling and motion control of the novel pneumatic textile actuator," *International Journal of Fluid Power*, pp. 1-10, 2016.
 - [96] Y. Sun, C. M. Lim, H. H. Tan, and H. Ren, "Soft oral interventional rehabilitation robot based on low-profile soft pneumatic actuator," in *2015 IEEE International Conference on Robotics and Automation, ICRA 2015*, 2015, pp. 2907-2912.
 - [97] C. Blanes, M. Mellado, and P. Beltran, "Novel Additive Manufacturing Pneumatic Actuators and Mechanisms for Food Handling Grippers," *Actuators*, vol. 3, pp. 205-225, 2014.
 - [98] NinjaTek, "NinjaFlex TDS," ed, 2016.
 - [99] R. L. Truby and J. A. Lewis, "Printing soft matter in three dimensions," *Nature*, vol. 540, pp. 371-378, 2016.
 - [100] J. W. Stansbury and M. J. Idacavage, "3D printing with polymers: Challenges among expanding options and opportunities," *Dental Materials*, vol. 32, pp. 54-64, 2016.
 - [101] H. N. Chia and B. M. Wu, "Recent advances in 3D printing of biomaterials," *Journal of Biological Engineering*, vol. 9, 2015.
 - [102] F. Alifui-Segbaya, S. Varma, G. J. Lieschke, and R. George, "Biocompatibility of Photopolymers in 3D Printing," *3D Printing and Additive Manufacturing*, vol. 4, pp. 185-191, 2017.
 - [103] H. Gong, B. P. Bickham, A. T. Woolley, and G. P. Nordin, "Custom 3D printer and resin for 18 μm \times 20 μm microfluidic flow channels," *Lab on a Chip*, vol. 17, pp. 2899-2909, 2017.
 - [104] S. C. Ligon-Auer, M. Schwentenwein, C. Gorsche, J. Stampfl, and R. Liska, "Toughening of photo-curable polymer networks: a review," *Polymer Chemistry*, vol. 7, pp. 257-286, 2016.

- [105] J. Stampfl, M. Schuster, S. Baudis, H. Lichtenegger, R. Liska, C. Turecek, *et al.*, "Biodegradable stereolithography resins with defined mechanical properties," in *3rd International Conference on Advanced Research in Virtual and Rapid Prototyping: Virtual and Rapid Manufacturing Advanced Research Virtual and Rapid Prototyping*, Leiria, 2007, pp. 283-287.
- [106] K. Kowsari, B. Zhang, S. Panjwani, Z. Chen, H. Hingorani, S. Akbari, *et al.*, "Photopolymer formulation to minimize feature size, surface roughness, and stair-stepping in digital light processing-based three-dimensional printing," *Additive Manufacturing*, vol. 24, pp. 627-638, 2018.
- [107] Formlabs, "Flexible FLFLGR02 Material Properties," ed: Formlabs Inc., 2016.
- [108] Spot-A Materials, "Spot-E Technical Data Sheet," ed: Spot-A Materials, 2017.
- [109] S. Baudis, B. Steyrer, T. Pulka, H. Wilhelm, G. Weigel, H. Bergmeister, *et al.*, "Photopolymerizable Elastomers for Vascular Tissue Regeneration," *Macromolecular Symposia*, vol. 296, pp. 121-126, 2010.
- [110] J. Zhang and P. Xiao, "3D printing of photopolymers," *Polymer Chemistry*, vol. 9, pp. 1530-1540, 2018.
- [111] J. Aerykssen and J. Piceno, "New Developments in Acrylate Oligomers for 3D Printing," presented at the RadTech UV + EB 2018, Chicago, Illinois, 2018.
- [112] Spot-A Materials, "Spot-E Materials Safety Data Sheet," ed: Spot-A Materials, 2012.
- [113] R. A. Shanks and I. Kong, "General Purpose Elastomers: Structure, Chemistry, Physics and Performance," in *Advances in Elastomers I: Blends and Interpenetrating Networks*, P. M. Visakh, S. Thomas, A. K. Chandra, and A. P. Mathew, Eds., ed Berlin, Heidelberg: Springer Berlin Heidelberg, 2013, pp. 11-45.
- [114] Formlabs, "Elastic 50A Materials Data Sheet," ed: Formlabs Inc., 2019.
- [115] Formlabs, "Flexible Safety Data Sheet," ed: Formlabs Inc, 2016.
- [116] S. Schüller-Ravoo, J. Feijen, and D. W. Grijpma, "Preparation of flexible and elastic poly(trimethylene carbonate) structures by stereolithography," *Macromolecular Bioscience*, vol. 11, pp. 1662-1671, 2011.
- [117] B. Huang, Z. Du, T. Yong, and W. Han, "Preparation of a novel hybrid type photosensitive resin for stereolithography in 3D printing and testing on the accuracy of the fabricated parts," *Journal Wuhan University of Technology, Materials Science Edition*, vol. 32, pp. 726-732, 2017.
- [118] Allnex, "EBECRYL 8411 Technical Data Sheet," ed: Allnex Group, 2017.
- [119] D. Lamone and J. Gotro. (2016, 17/05/2017). *UV Curing*. Available: <https://polymerinnovationblog.com/uv-curing-part-one-let-light/>
- [120] Allnex, "EBECRYL 8413 Technical Data Sheet," ed: Allnex Group, 2017.
- [121] A. L. Skov and L. Yu, "Optimization Techniques for Improving the Performance of Silicone-Based Dielectric Elastomers," *Advanced Engineering Materials*, 2017.

- [122] V. S. D. Voet, T. Strating, G. H. M. Schnelting, P. Dijkstra, M. Tietema, J. Xu, *et al.*, "Biobased Acrylate Photocurable Resin Formulation for Stereolithography 3D Printing," *ACS Omega*, vol. 3, pp. 1403-1408, 2018.
- [123] S. Baudis, F. Nehl, S. C. Ligon, A. Nigisch, H. Bergmeister, D. Bernhard, *et al.*, "Elastomeric degradable biomaterials by photopolymerization-based CAD-CAM for vascular tissue engineering," *Biomedical Materials*, vol. 6, 2011.
- [124] C. Hinczewski, S. Corbel, and T. Chartier, "Ceramic suspensions suitable for stereolithography," *Journal of the European Ceramic Society*, vol. 18, pp. 583-590, 1998.
- [125] R. Viereckl, M. Gould, V. Petry, R. Dodd, X. Marguerettaz, and S. Des Roches, "Formulating for 3D printing (SLA)," presented at the RadTech UV + EB 2018, Chicago, Illinois, 2018.
- [126] A. Torres-Knoop, I. Kryven, V. Schamboeck, and P. D. Iedema, "Modeling the free-radical polymerization of hexanediol diacrylate (HDDA): A molecular dynamics and graph theory approach," *Soft Matter*, vol. 14, pp. 3404-3414, 2018.
- [127] M. De Brito, "Investigation of interpenetrating polymer networks and recent UV curable chemistries," Université de Haute Alsace - Mulhouse, 2011.
- [128] W. A. Green, *Industrial Photoinitiators: A Technical Guide*: CRC Press, 2010.
- [129] C. Decker, "Kinetic study and new applications of UV radiation curing," *Macromolecular Rapid Communications*, vol. 23, pp. 1067-1093, 2002.
- [130] D. Oliveira, M. Rocha, I. Corrêa, A. Correr, J. Ferracane, and M. Sinhoret, *The effect of combining photoinitiator systems on the color and curing profile of resin-based composites*, 2016.
- [131] C. D. Diakournakos, Q. Xu, F. N. Jones, J. Baghdachi, and L. Wu, "Synthesis of acrylic resins for high-solids coatings by solution and separation polymerization," *Journal of Coatings Technology*, vol. 72, pp. 61-70, 2000.
- [132] M. Idacavage, "Introduction to the Basics of UV/EB Chemistry and Formulations," ed: RadTech, 2015.
- [133] C. Decker, "UV-radiation curing chemistry," *Pigment & Resin Technology*, vol. 30, pp. 278-286, 2001.
- [134] K. Hanhi, M. Poikelispää, and H. M. Tirilä. (2007, 2019-02-04). *Elastomeric materials*. Available: https://www.tut.fi/ms/muo/vert/6_elastomeric_materials/index.htm
- [135] C. Hepburn, *Polyurethane Elastomers*, 2nd ed. New York, NY, USA: Elsevier Applied Science 1992.
- [136] University of York Centre for Industry Education Collaboration. (2016, 2018-08-10). *Polyurethanes*. Available: <http://www.essentialchemicalindustry.org/polymers/polyurethane.html>
- [137] L. Zhang and J. Huang, "Effects of hard-segment compositions on properties of polyurethane-nitrolignin films," *Journal of Applied Polymer Science*, vol. 81, pp. 3251-3259, 2001.

- [138] Z. Khoubi-Arani, S. R. Ghaffarian, and G. M. M. Sadeghi, "Synthesis of flexible elastomeric polyurethane films with high elasticity and evaluation of their structural permanency," *Journal of Macromolecular Science, Part A: Pure and Applied Chemistry*, vol. 51, pp. 180-188, 2014.
- [139] B. K. Kim, K. H. Lee, and H. D. Kim, "Preparation and properties of UV-curable polyurethane acrylates," *Journal of Applied Polymer Science*, vol. 60, pp. 799-805, 1996.
- [140] T. Y. Lee, T. M. Roper, E. S. Jönsson, C. A. Guymon, and C. E. Hoyle, "Influence of hydrogen bonding on photopolymerization rate of hydroxyalkyl acrylates," *Macromolecules*, vol. 37, pp. 3659-3665, 2004.
- [141] L. Qin, Y. He, B. Liu, Y. Jian, C. Li, and J. Nie, "Preparation and properties of polyurethane acrylates modified by saturated alcohols," *Progress in Organic Coatings*, vol. 76, pp. 1594-1599, 2013.
- [142] B. Rundlett, "Photoinitiator Selection," ed: DSM Functional Materials, 2012.
- [143] H. Seo, S. G. Heo, H. Lee, and H. Yoon, "Preparation of PEG materials for constructing complex structures by stereolithographic 3D printing," *RSC Advances*, vol. 7, pp. 28684-28688, 2017.
- [144] H. Gong, M. Beauchamp, S. Perry, A. T. Woolley, and G. P. Nordin, "Optical approach to resin formulation for 3D printed microfluidics," *RSC Advances*, vol. 5, pp. 106621-106632, 2015.
- [145] C. S. Sodré, P. P. A. C. Albuquerque, C. P. Isolan, R. R. Moraes, and L. F. Schneider, "Relative photon absorption determination and the influence of photoinitiator system and water content on C=C conversion, water sorption/solubility of experimental self-etch adhesives," *International Journal of Adhesion and Adhesives*, vol. 63, pp. 152-157, 2015/12/01/ 2015.
- [146] Allnex, "TPO Technical Data Sheet," ed: Allnex, 2014.
- [147] V. E. Salgado, M. M. Borba, L. M. Cavalcante, R. R. De Moraes, and L. F. Schneider, "Effect of photoinitiator combinations on hardness, depth of cure, and color of model resin composites," *Journal of Esthetic and Restorative Dentistry*, vol. 27, pp. S41-S48, 2015.
- [148] J. G. Leprince, M. Hadis, A. C. Shortall, J. L. Ferracane, J. Devaux, G. Leloup, *et al.*, "Photoinitiator type and applicability of exposure reciprocity law in filled and unfilled photoactive resins," *Dental Materials*, vol. 27, pp. 157-164, 2011.
- [149] C. C. Chiu, "Liquid bis-acylphosphine oxide (BAPO) photoinitiators," presented at the Radtech UV & EB Technology Expo & Conference, Baltimore, 2010.
- [150] R. Jahn and T. Jung, "Relationship between pigment properties and UV-curing efficiency," *Progress in Organic Coatings*, vol. 43, pp. 50-55, 2001.
- [151] Spot-A Materials. (2013, 2017-09-10). *Is it better to use dyes or pigments?* Available: <http://spotamaterials.com/question/better-to-use-dyes-or-pigments/>
- [152] Spot-A Materials. (2013, 2017-09-10). *Which dyes or pigment colors are best for your resins?* Available: <http://spotamaterials.com/question/which-dyes-or-pigment-colors-are-best-for-your-resins/>

- [153] Y. Duan, Y. Huo, and L. Duan, "Preparation of acrylic resins modified with epoxy resins and their behaviors as binders of waterborne printing ink on plastic film," *Colloids and Surfaces A: Physicochemical and Engineering Aspects*, vol. 535, pp. 225-231, 2017.
- [154] J. Wang, A. Goyanes, S. Gaisford, and A. W. Basit, "Stereolithographic (SLA) 3D printing of oral modified-release dosage forms," *International Journal of Pharmaceutics*, vol. 503, pp. 207-212, 2016.
- [155] T. Morikawa, T. Kobayasi, M. Kataoka, and A. Mori, "Photo-curable urethane-acrylate resin composition for permanent resist," 1986.
- [156] J. Wu, Z. Zhao, C. M. Hamel, X. Mu, X. Kuang, Z. Guo, *et al.*, "Evolution of material properties during free radical photopolymerization," *Journal of the Mechanics and Physics of Solids*, vol. 112, pp. 25-49, 2018.
- [157] B. Steyrer, B. Busetti, G. Harakály, R. Liska, and J. Stampfl, "Hot Lithography vs. room temperature DLP 3D-printing of a dimethacrylate," *Additive Manufacturing*, vol. 21, pp. 209-214, 2018.
- [158] M. C. Rusu, C. Block, G. Van Assche, and B. Van Mele, "Influence of temperature and UV intensity on photo-polymerization reaction studied by photo-DSC," *Journal of Thermal Analysis and Calorimetry*, vol. 110, pp. 287-294, 2012.
- [159] J. W. Park, G. S. Shim, J. G. Lee, S. W. Jang, H. J. Kim, and J. N. Choi, "Evaluation of UV curing properties of mixture systems with differently sized monomers," *Materials*, vol. 11, 2018.
- [160] L. Pichavant and X. Coqueret, "Optimization of a UV-curable acrylate-based protective coating by experimental design," *Progress in Organic Coatings*, vol. 63, pp. 55-62, 2008.
- [161] X. Kuang, K. Chen, C. K. Dunn, J. Wu, V. C. F. Li, and H. J. Qi, "3D Printing of Highly Stretchable, Shape-Memory, and Self-Healing Elastomer toward Novel 4D Printing," *ACS Applied Materials & Interfaces*, vol. 10, pp. 7381-7388, 2018/02/28 2018.
- [162] R. Lakes, *Viscoelastic Materials*. New York, UNITED STATES: Cambridge University Press, 2009.
- [163] Y. Yan, V. Sencadas, T. Jin, X. Huang, W. Lie, D. Wei, *et al.*, "Effect of multi-walled carbon nanotubes on the cross-linking density of the poly(glycerol sebacate) elastomeric nanocomposites," *Journal of Colloid and Interface Science*, vol. 521, pp. 24-32, 2018.
- [164] P. Gloeckner, *Radiation Curing*: Vincentz, 2009.
- [165] polymerdatabase.com. (2015, 2019-07-19). *Stress-Strain Behavior of Polymers*. Available: <https://polymerdatabase.com/polymer%20physics/Stress-Strain%20Behavior.html>
- [166] R. S. Spencer and R. E. Dillon, "The viscous flow of molten polystyrene. II," *Journal of Colloid Science*, vol. 4, pp. 241-255, 1949.
- [167] J. Austin, A. Schepelmann, and H. Geyer, "Control and evaluation of series elastic actuators with nonlinear rubber springs," in *IEEE/RSJ International Conference on Intelligent Robots and Systems, IROS 2015*, 2015, pp. 6563-6568.

- [168] M. Negahban, *The Mechanical and Thermodynamical Theory of Plasticity*. Bosa Roca, UNITED STATES: Taylor & Francis Group, 2012.
- [169] L. H. Sperling, *Introduction to Physical Polymer Science*, 4th ed.: Wiley Online Books, 2006.
- [170] Q. Z. Chen, A. Bismarck, U. Hansen, S. Junaid, M. Q. Tran, S. E. Harding, *et al.*, "Characterisation of a soft elastomer poly(glycerol sebacate) designed to match the mechanical properties of myocardial tissue," *Biomaterials*, vol. 29, pp. 47-57, 2008.
- [171] R. Vera-Graziano, F. Hernandez-Sanchez, and J. V. Cauich-Rodriguez, "Study of crosslinking density in polydimethylsiloxane networks by DSC," *Journal of Applied Polymer Science*, vol. 55, pp. 1317-1327, 1995.
- [172] F. Zhao, W. Bi, and S. Zhao, "Influence of Crosslink Density on Mechanical Properties of Natural Rubber Vulcanizates," *Journal of Macromolecular Science, Part B*, vol. 50, pp. 1460-1469, 2011/07/01 2011.
- [173] C. A. Finch, "Polymer handbook: Third edition Edited by J. Brandrup and E. H. Immergut, Wiley-Interscience, Chichester, 1989. pp. ix + parts I to VIII, price £115 00/\$;175 00. ISBN 0-471-81244-7," *British Polymer Journal*, vol. 23, pp. 277-277, 1990/01/01 1990.
- [174] P. Rothmund, A. Ainla, L. Belding, D. J. Preston, S. Kurihara, Z. Suo, *et al.*, "A soft, bistable valve for autonomous control of soft actuators," *Science Robotics*, vol. 3, p. eaar7986, 2018.
- [175] T. Duggan, L. Horowitz, A. Ulug, E. Baker, and K. Petersen, "Inchworm-inspired locomotion in untethered soft robots," 2019, pp. 200-205.
- [176] J. Waynelovich, T. Frey, A. Baljon, and P. Salamon, "Versatile and dexterous soft robotic leg system for untethered operations," *Soft Robotics*, vol. 3, pp. 64-70, 2016.
- [177] M. T. Tolley, R. F. Shepherd, B. Mosadegh, K. C. Galloway, M. Wehner, M. Karpelson, *et al.*, "A Resilient, Untethered Soft Robot," *Soft Robotics*, vol. 1, pp. 213-223, 2014.

APPENDIX A

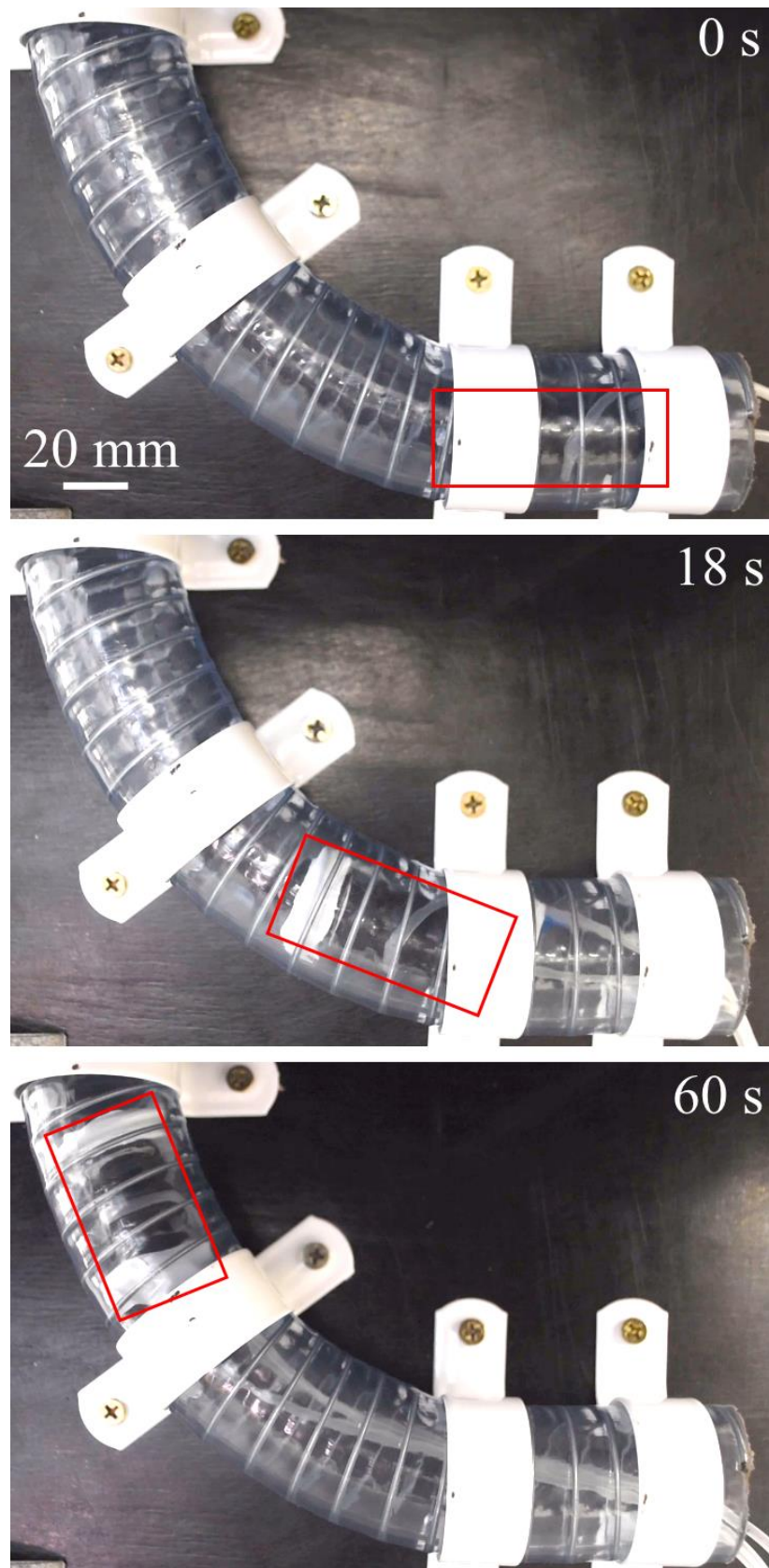


Figure A.1 Pipe crawler robot moving through a 90° bent pipe.

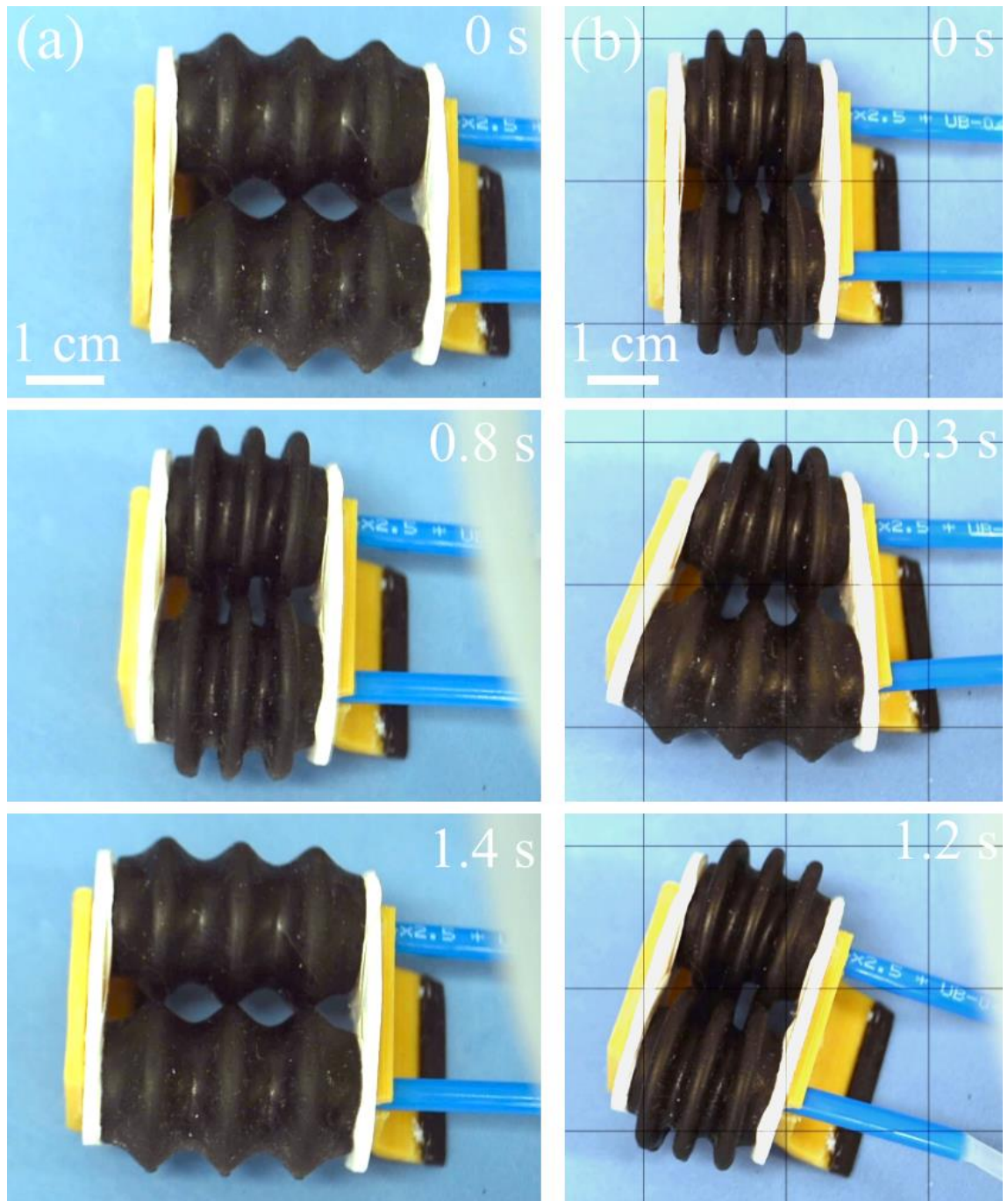


Figure A.2 Tethered locomotion robot crawling under -20 kPa: (a) forwards motion steps and (b) turning motion steps.